Improving Deep Exploration with Cost-Effective Geophysical Methods.

Alexander Furlan, B.Sc.

Earth Science

Submitted in partial fulfillment of the requirements for the degree of:

Master of Science

Faculty of Mathematics and Science, Brock University

St. Catharines, Ontario

Abstract

Key Words: Geophysics, Electromagnetics, Open-source, 3D-Modelling, Inversion

Subsurface exploration is rapidly changing and ‘easy to target’ deposits are depleting across the world. This reality has pushed exploration in two directions: re-evaluating known deposits and exploring greater depths. The goal of this thesis was to address these trends in a cost-effective manner. First, by combining geophysical, borehole, and open-source spatial data, a 3D model was synthesized for a volcanogenic massive sulphide (VMS) deposit located in Nash Creek, NB. Evaluating this model showed a need for structural controls to better understand the genesis of the deposit. A lesser-known geophysical system, Extremely Low Frequency EM (ELF-EM), measures ~2km deep and can produce conductivity models. While perfect for Nash Creek, ELF lacked modern software support which limited the modelling that could be done. Using an open-source inversion package, a python script is presented with this thesis that runs inversions of tipper (ELF) data to produce 3D conductivity models. This new workflow was tested at the Key Anacon VMS deposit near Bathurst, NB. A 3D wireframe model derived from geophysical surveying and borehole logs was available to compare with the ELF-EM derived model at Key Anacon. While individual mineralized horizons could not be discerned, a ‘conductive envelope’ follows a very similar strike and dip to the wireframe model. Promising results from Key Anacon led to the re-interpretation of past ELF-EM surveys. The final section of this thesis revisits a survey in Burwash Landing, Yukon to compare conductivity modelling results. The Burwash Landing survey aimed to identify potential geothermal wells drilling sites along the Denali fault. The new 3D model showed a coherent fault trace along strike, as well as eliminated several anomalies the researchers in the original paper could not explain. This improved ELF-EM inversion workflow has greatly improved 3D modelling of deep conductivity contrasts. In future, the techniques outlined here can be applied to various exploration scenarios while following the current trends in exploration.

Preface

The recent pandemic was not an ideal time to be a student but finally, with great pleasure, this thesis can be submitted. That said, some clarification is needed on the relation between Ch. 2 & Ch. 3 & 4. The original plan was to collect tipper data over Nash Creek to: A) test the new SimPEG workflow, B) gain knowledge of the BPAB fault at depth, and C) improve the Nash Creek 3D model using the newly acquired data. This addition would have greatly improved the cohesiveness of the thesis chapters, tying everything into ELF-EM. Unfortunately, COVID-19 eliminated the chance to complete field work and access to GeoModeller at this time was lost. Regardless, Ch. 2 was included as it presents a good example of multi-source 3D modelling. The disconnect between this chapter and the rest of the thesis is unfortunate, but such global-scale events cannot be predicted (unlike our observed data). The framework to achieve what was originally planned is clearly seen throughout but chapter 2 will remain a book with a few pages left to turn.

Contents

Figures

Tables

1.0 - Introduction

The number of easy-to-target or near-surface mineral deposits are rapidly depleting (Ranjith et al., 2017; McCutcheon & Walker, 2019; Xie, Konientzky, & Zhou, 2019). As the exploration industry adapts, so do geophysicists by shifting their focus to methods that identify physical properties at greater depths. Of the ~28,000 mineral exploration articles published from 1997-2021, 3,200 of them specified *deep* mineral exploration. When this 25-year period is broken into 5-year intervals, the percent total shows an exponential increase (Table 1). While the shear number of exploration papers is increasing, *deep* mineral exploration papers are being published at a higher rate. One of the geophysical techniques responsible for this increase is known as Magnetotellurics (MT). While the theory behind MT has existed since the 1950's (Tikhonov, 1950; Rikitake, 1950; Cagniard, 1953), modern-era computing and instrumentation has allowed MT to flourish as a tool for mineral exploration at depth (Heinson et al., 2018). For geophysical techniques that take advantage of MT, the process of inversion is imperative. At its core, inversions construct and refine a physical property model based on observational data the user provides. Property contrasts in these models can be related to rock type or structure by combining the model with existing geological knowledge at the survey site. (Lelievre, Oldenburg, & Williams, 2008). Until recently, geophysical inversions required exceptional knowledge in programming, geology, and geophysics or substantial capital to purchase a software license. The goal of this thesis was to develop cost effective 3D modelling techniques using geophysical data, which in part, measures a new critical depth range for mineral exploration. Improvements in geophysical modelling software has enabled construction of full 3D models derived from surface mapping, borehole data, and geophysical surveying. These models provide a more 'complete' picture of the subsurface by synthesizing data from multiple sources, reducing unknown variables. This methodology was applied in chapter 2 to a volcanogenic massive sulphide (VMS) deposit in Nash Creek, New Brunswick. This deposit has undergone previous exploration, but a full 3D model had yet to be constructed. When this model is constructed, it becomes clear that a better understanding of the structures at depth would provide the most significant improvement to the model. MT or seismic methods are forerunners, but these are expensive or very time consuming. A lesser-known MT method, Extremely Low Frequency Electromagnetics (ELF-EM), requires minimal manpower and time compared to traditional MT.

Table 1 – Number of journal articles that mention 'deep mineral exploration' compared to 'mineral exploration' as seen on Brock University Omni Libraries. Only English-written, peer-reviewed journal articles were included in these counts. The first column divides a 25-year period into 5-year increments. The second column shows 'deep mineral exploration' articles compared to 'mineral exploration' expressed as a count and percentage. The final column compares each period to the total across all 25 years. From 2007 on, the number of 'deep mineral exploration' journal articles show an exponential increase between each period.

Increments	'Deep mineral exploration' / 'Mineral exploration'		Percentage of 'Deep mineral exploration' Total (Total = 3,200)
	Count	Percent	
1997-2001	171 / 2,487	7%	5%
2002-2006	260 / 2,919	9%	8%
2007-2011	408 / 4,086	10%	11%
2012-2016	744 / 6,950	11%	23%
2017-2021	1,617 / 11,671	14%	51%

ELF data (also known as tipper data) identifies conductivity contrasts up to an approximate depth of 2 km (Hildes, 2014). Unfortunately, there are only a few tools that can invert ELF data and produce a conductivity model, but these are either tough to access or outdated / lack support. Chapter 3 outlines a new tipper inversion code that uses open-source python packages to create a full 3D conductivity model. This code was tested using data from the Key Anacon Volcanogenic Massive Sulphide (VMS) deposit near Bathurst, New Brunswick. The resulting conductivity model was compared to 3D wireframe models derived from geophysical and geological data collected by Osisko Metals Inc. or the previous owners. The model created in chapter 3 effectively identified a conductivity contrast related to the sulphide horizons present at Key Anacon. With this confirmation of effectiveness, it opens the door for previous ELF surveys to be re-interpreted using the new 3D modelling methodology. In chapter 4, ELF data collected by Aurora Geoscience Ltd. for the Yukon Geological Survey is re-evaluated using the new inversion code. A study of potential geothermal energy sources was completed over the Denali fault near Burwash Landing, Yukon (Witter, 2020). This study included ELF-EM data processed using the previous 2D ELF inversion code. Chapter 4 discusses re-interpretation of these results using the methods outlined in chapter 3. The resulting conductivity model was geologically plausible and showed a conductive anomaly that follows the Denali & Bock's Creek fault. This thesis concludes by discussing future improvements to the inversion code that would improve its useability and analysis of ELF data. The combination of open-source software & low operational costs make the ELF an attractive option for greenfield and brownfield exploration, as well as provide researchers a low barrier of entry to further the work outlined in this report.

2.0 - 3D modelling of a VMS without depth constraints – Nash Creek, NB

2.1 – Introduction

Using 3D modelling for mineral exploration is not a new concept (Gibb & Thomas, 1980; Holyland & Ojala, 1997; Artimo et al., 2003). Several software packages exist that deal with geological data such as Maptek Vulcan or the Datamine suite of applications. These modelling packages typically use borehole information to act as geological constraints. Another option to constrain the model is to use geophysical data to highlight property contrasts related to subsurface bodies or structure. Geophysical modelling packages like ModelVision (product of Datamine) can help construct lithological models that take geophysical surveys, geological maps, and borehole logs into consideration. These data supplement each other to minimize assumptions of the subsurface. 3D modelling is extensively used for mineral deposits but if the estimated resource lacks economic viability, less exploration effort will be put into it. One such deposit exists in Nash Creek, New Brunswick. This VMS deposit had been drilled & surveyed with geophysical techniques, but lacks a full 3D model that encompasses all data sources. Previous researchers, including Veglio (2017), have geophysically investigated the source of mineralization at Nash Creek but focus was on magnetic surveying & petrophysical data. This chapter aimed to improve understanding of the Nash Creek VMS deposit by creating a 3D model that considered the multitude of data sources. Callinex Mines Inc. provided borehole & geophysical data collected at the deposit which was further supplemented using public data provided from the Open Government Portal. The resulting 3D model required no additional data to be collected (minimizing cost) while showing that some constraint on local structural features at depth would provide the greatest improvement to the model and our understanding of Nash Creek.

2.2 – Geologic Setting

The Nash Creek exploration area lies within the Chaleur Bay Synclinorium in northeastern New Brunswick (Figure 1). Located on the Jacquet River Syncline (JRS) & transected by the Black Point - Arleau Brook (BPAB) Fault, this region is underlain by the Quinn Point (Early Silurian), Dickie Cove (Late Silurian), & Dalhousie (Early Devonian) Groups (Wilson, 2013). These units are part of the Matapedia Cover Sequence which formed on the eastern margin of Laurentia during the closure of the Tetagouche back-arc basin (Fyffe & Fricker, 1987). The Quinn Point Group is characterized by various siltstone, sandstone, limestone, and shale units. The presence of faunal

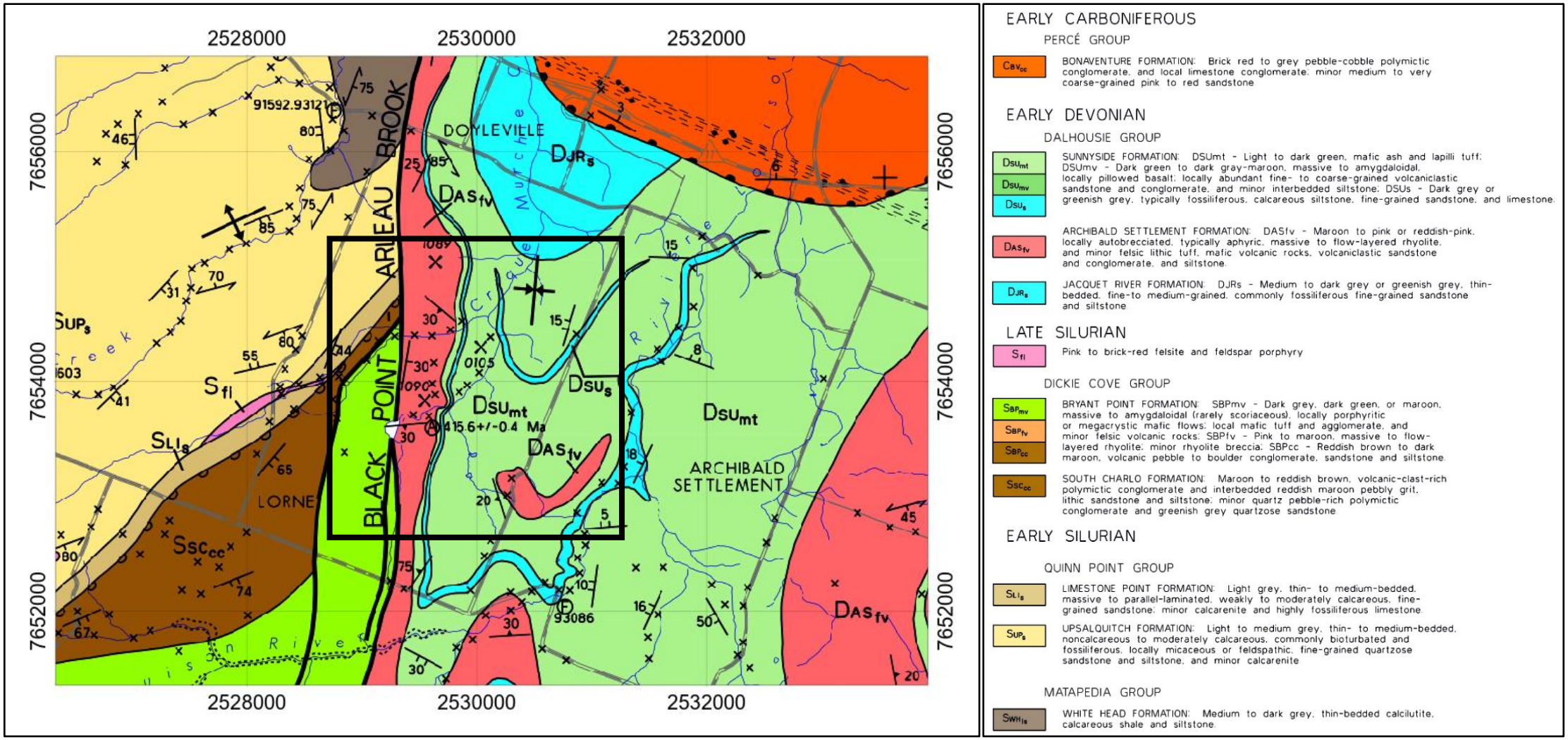

Figure 1 – (LEFT) 1:50,000 scale map of the Nash Creek geology. Focused survey area for modelling is outlined with black square. (RIGHT) Modified legend showing formations present in the survey area. Projected coordinates are New Brunswick Double Stereographic. Modified from Wilson (2013)

communities within the Limestone Point Formation indicates a shallow shelf depositional environment (Noble, 1976). The Dickie Cove Group disconformably overlies Quinn Point west of the BPAB fault. This group is a mix of sedimentary coarse-grained clastics, basaltic and rhyolitic flows, pyroclastics, and volcaniclastic conglomerates. Volcanic rocks in the Dickie Cove Group are constrained to the Bryant Point & Benjamin Formations. Marking the transition from Late Silurian to Early Devonian, the Dickie Cove Group is disconformably overlain by the Dalhousie Group. The Mitchell Settlement Formation forms the basal unit and is comprised of amygdaloidal mafic volcanics interbedded with sandstone. Fine-grained sedimentary rocks make up the Jacquet River Formation while Archibald Settlement is characterized by aphyric and flow-layered rhyolite. Within the survey area outlined above, felsic pyroclastics including heterolithic lapilli tuff, bedded ash tuff, epiclastic volcanics and coarse-grained tuffaceous sedimentary rocks are present. Lastly, the Sunnyside Formation is comprised of mafic pyroclastics (dominant), flows (minor), and pillows (rare). Structurally speaking, the Jacquet River Syncline is north trending, doubly plunging, and regionally folded (Walker, 2010). The Mitchell Settlement, Jacquet River, Archibald Settlement, and Sunnyside Formations are all present within the JRS (Wilson, 2013). A hydrothermal Zn-Pb-Ag deposit is located along the western limb, terminating at the north trending BPAB fault. This fault has been identified as an east dropping half graben structure, but no strike or dip measurements are known (Tetra Tech, 2018). The deposit is mainly hosted in the bimodal volcanism of the Archibald Settlement and Sunnyside Formations. The sulphides seen in borehole logs are strata-bound, laterally continuous, and occur as replacement-style mineralization or matrix fill in rock fractures, pyroclastics, and distinct breccia zones (Ugalde et al., 2019). The 3D model constructed in this paper focuses on the Hickey Zone, where most of the mineralization is seen in the Sunnyside Formation. Within the Hickey zone, several (three to four) distinct but discontinuous flat lying mineralized horizons have been identified. The mineralization in the Hickey zone is hosted in mafic-dominated rocks and seen ~1.6 km along strike of the BPAB fault, extending east from the fault trace, ~200 meters (Tetra Tech, 2018).

2.3 – Methodology

To develop a reasonable 3D model, a workflow for collecting, processing, interpreting, and modelling geological and geophysical data was needed. Data were collected from various sources including the Canadian Open Data platform, thesis work from students who worked in the region

Table 2 - Compilation of geological and geophysical information. The table is divided into two periods: Devonian and Silurian. Descriptions for each formation were created using public data provided by the New Brunswick Geological Survey. The fourth column is colour coded and gives a generalized rock type: Mafic – RED, Sedimentary – GREEN, Intermediate – BLUE, Felsic – YELLOW. The fifth column shows estimated thicknesses given from the NB government formation descriptions. The final two columns show potential density and magnetic susceptibility values for each unit based on previous research (L'Heureux, 2007; Bongajum, 2013; Veglio, 2017; Hebert, 2018; Ondercova, 2019).

					Rock Properties	
Devonian					Density (g/cm^3)	Magnetic Susceptibility (SI)
Early (Dalhousie)	Val D'amour	Dominantly subaerial mafic, ultramafic, intermediate, and felsic effusive and pyroclastic rocks, fine- to very coarse-grained volcaniclastic rocks, subvolcanic plugs and domes, and minor sedimentary rocks.	IV - Intermediate Volcanics	Thickness = 1900m - 5700m (West - East)	2.66-2.67	0.01 - 0.02
			S - Sedimentary		2.68	0.00005 - 0.02
			VS - Mixed Volcanics and Sedimentary		2.7-2.72	0.01 - 0.02
			MV - Mafic Volcanics		2.78	0.04 - 0.07
			MT - Mafic Tuff		2.78	0.04 - 0.07
	Sunnyside	Dominantly mafic pyroclastic rocks (mafic flows inc. pillows are subordinate).	MT - Mafic Tuff	Irregular N-S belt	2.78	0.04 - 0.07
			MV - Mafic Volcanics	Thickness = 160m - 500m (30m at Nash Creek)	2.78	0.04 - 0.07
			S - Sedimentary	500m based on avg. dip of 25 degrees	2.68	0.00005 - 0.02
	Archibald	Typically, aphyric and flow-layered, commonly spherulitic and perlitic, locally autobrecciated rhyolite. AT NASH, felsic pyroclastic and includes heterolithic lapilli tuff, bedded ash tuff, and epiclastic volcanic and coarse-grained tuffaceous sedimentary rocks	FV - Felsic Volcanics	Thickness = 155m - 760m estimated on eastern belt (155m at Nash Creek)	2.65	0.01-0.05
	Jacquet River	Mainly thin-bedded, parallel-laminated (common), fossiliferous (common), non- to moderately- calcareous, fine-grained sandstone, siltstone, and mudstone	S - Sedimentary	Thickness = (300m) 500m - 1200m	2.68	0.00005 - 0.003
	Wildcat Brook	Thin basal unit of sedimentary rocks, overlain by mafic flows and tuffs, and felsic volcanics in the eastern part of the belt	FV - Felsic Volcanics	Thickness = 1600m - 200m, Max thickness just west of Arleau Brook Fault	2.65	0.01-0.05
			MV - Mafic Volcanics		2.78	0.04 - 0.07
			S - Sedimentary		2.68	0.00005 - 0.02
	Mitchell Settlement	3 main sections: basal amygdaloidal mafic volcanic interbedded with sand & siltstone, sandstone with minor mafics, mafic flows w/ minor sedimentary rocks	MV - Mafic Volcanics	Thickness = 1000m to 1200m	2.78	0.04 - 0.07

Silurian					Gravity (g/cm^3)	Magnetic Susceptibility
Late (Dickie Cove)	Benjamin	Dominantly rhyolitic lavas, locally abundant felsic pyroclastics, mafic volcanics, minor intercalated fine to coarse volcaniclastic sedimentary rocks	FV - Felsic Volcanics	Thickness = ~1100m, potentially less in JRS eastern limb	2.65	0.01-0.05
			FT - Felsic Tuff		2.65	0.01-0.05
			MV - Mafic Volcanics		2.78	0.04 - 0.07
	New Mills	2 main sections: 1) felsic volcanic-clast conglomerate, sandstone, and siltstone 2) unbedded, unsorted felsic volcanic conglomerate (Deposited as subaerial flows)	CC - Coarse Grained Clastic Sedimentary	Thickness = 100m - 350m	2.68	0.00005 - 0.02
	Bryant Point	mainly porphyritic XOR amygdaloidal basaltic flows, minor breccias, pyroclastics, rhyolite flows, minor sedimentary rocks	MV - Mafic Volcanics	Thickness = 400m - 800m	2.78	0.04 - 0.07
			FV - Felsic Volcanics		2.65	0.01 - 0.05
			CC - Coarse Grained Clastic Sedimentary		2.68	0.00005 - 0.02
	South Charlo	conglomerate, coarse grained sandstone, quartzose sandstone, lithic wacke, siltstone	CC - Coarse Grained Clastic Sedimentary	Thickness = 90m - 450m (@belledune), thin on west side of Arleau Brook & thickens to the east	2.68	0.00005 - 0.02
Early (Quinn Point)	Limestone Point	sandstone, siltstone, limestone, shale… nearshore to shallow shelf, high-energy, depositional environment (fossils)	S - Sedimentary	Thickness = ~250m	2.68	0.00005 - 0.003
	Upsalquitch	calcareous siltstone, sandstone, minor shale	S - Sedimentary	Thickness = ~1000m	2.68	0.00005 - 0.003

previously (L'Heureux, 2007; Bongajum, 2013; Veglio, 2017; Hebert, 2018; Ondercova, 2019), and Callinex Mines Inc. 43-101 report (P&E Mining Consultants Inc., 2018; Tetra Tech, 2018). These data, if spatial, were compiled into a GIS database. Spatial data were reprojected to NAD83 UTM Zone 19N to ensure a common reference system was used throughout the modelling process. Other information useful for modelling, such as formation descriptions and estimated unit thickness, were compiled in a spreadsheet for future reference (Table 2). After selecting which datasets were best suited for the project scope, a survey footprint was determined using a combination of geophysical coverage & geological constraints (i.e., boreholes, petrophysics, surficial geology, etc.). Coverage was best for magnetic and gravity measurements, so data were sampled along seven profiles at 2-meter intervals within the coverage footprint (Figure 2). Each point along the model line was now associated with an X, Y, and Z coordinate, as well as a gravity and magnetic measurement. These data were used to construct the initial 2D modelling sections which would then be used as a starting point for 3D modelling. These modelling profiles are near perpendicular to regional structures and provide strong property contrasts that can be identified in geophysical modelling. Geophysical responses, high resolution topographic data, borehole data, formation descriptions, and petrophysics were used to constrain the model sections. Once complete, the 2D sections were imported into 3D modelling software to perform a stochastic inversion. This creates a lithological model based on physical properties, structures, and units assigned within the program.

2.3.1 – Rock Properties

Downhole logging is seldom an option at Nash Creek and as such, rock properties cannot be measured insitu. The properties of interest for modelling, density & magnetic susceptibility, have been assigned local estimates based on drill core measurements collected since 2007 (L'Heureux, 2007; Bongajum, 2013; Veglio, 2017 & Hebert, 2018). While this is a large potential source of error, limitations in modelling prevented. Bongajum et al. (2013) used the buoyancy method to collect 6000 density measurements across 32 boreholes in the Nash Creek area. Average density values for mafic, felsic, and sedimentary rocks were determined to be 2.78 ± 0.15, 2.65 ± 0.30, 2.68 ± 0.24 g/cm^3 respectively. The sulphide mineralization showed a greater average density (3.0 ± 0.23 g/cm^3) against the host rock (2.7 g/cm^3) as well. The standard deviations of each unit were not available but calculated afterwards using the original dataset.

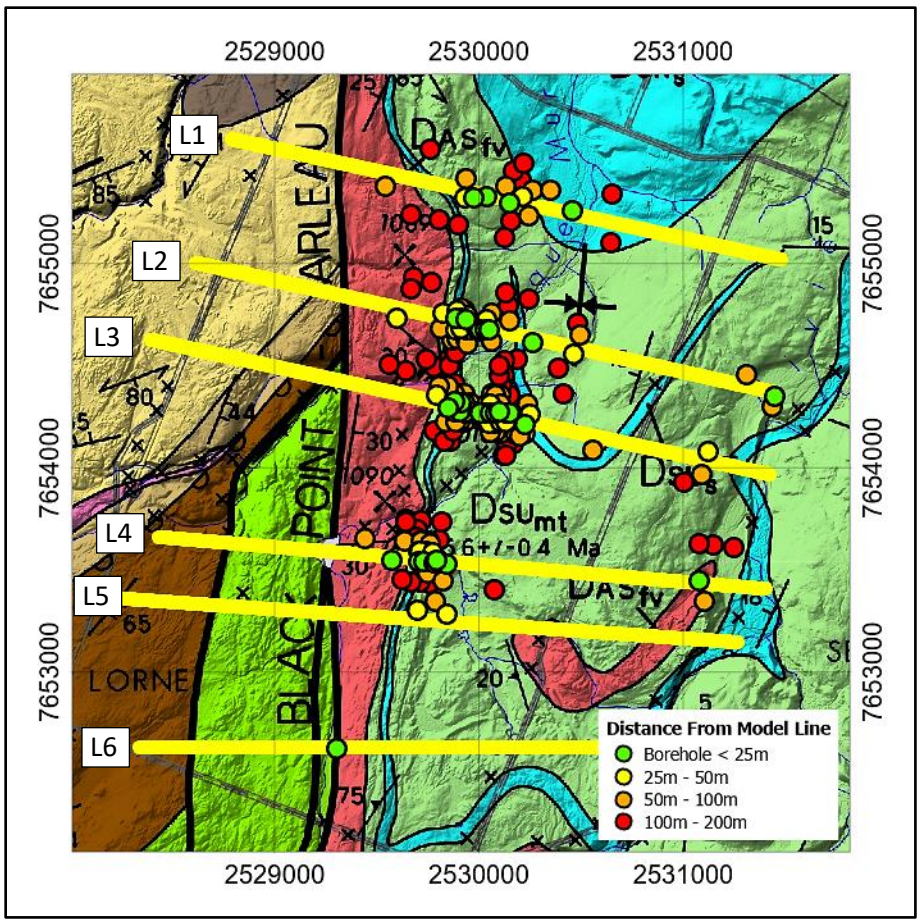

Figure 2 – Spatial distribution of boreholes within 200m of a model line at Nash Creek. Projected coordinates are New Brunswick Double Stereographic. Modified from Wilson (2013)

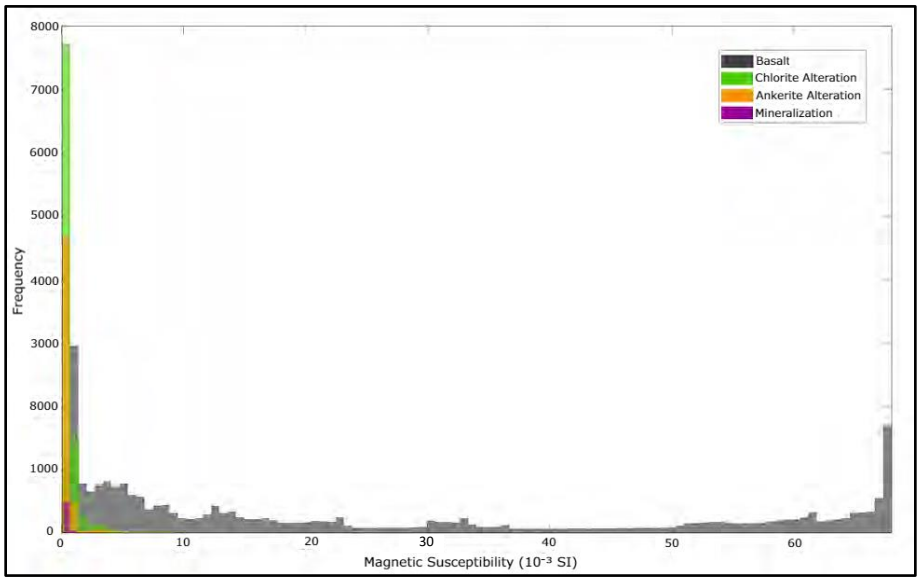

Figure 3 – Histogram of magnetic susceptibility at Nash Creek for seven boreholes drilled between 2007 - 2008. Measurements were taken with a KT-20 Magnetic Susceptibility Meter. These susceptibility values were classified on their hydrothermal association and show a bimodal distribution. Figure modified from Veglio (2017).

Magnetic susceptibility measurements were collected at 0.2m intervals for two boreholes in 2007, but a distinction could not be made between the brecciated basalt and the basaltic / mafic tuff units which host the mineralization (L'Heureux et al., 2007). Veglio (2017) furthered the magnetic susceptibility database by logging core from 15 boreholes, ranging from ~50m to ~600m depth. 70000+ data points were collected using the KT-20 magnetic susceptibility meter and showed a bimodal distribution ranging from $1x10^{-3}$ to $70x10^{-3}$ SI (Figure 3). When cross referenced with geology, altered & mineralized units have low magnetic susceptibility (~$1\text{-}5x10^{-3}$ SI), volcanic and fault breccias have slightly higher values (10-$20x10^{-3}$ SI), whereas the max values measured (~40-$70x10^{-3}$ SI) are attributed to basalt (Veglio, 2017). One factor that has not been addressed is remanent magnetization. This residual magnetic field can be orders of magnitude greater than induced magnetization and vary in direction from the current induced field. No remnant magnetization was accounted for in this report but how this impacts the model is touched on below.

2.3.2 – Geophysics

Geophysical survey coverage was a key determining factor in where modelling should take place (Figure 4). The earliest mine discoveries in New Brunswick can be attributed to the successful application of geophysical methods (McCutcheon & Walker, 2019). In the 1950's, airborne magnetic anomalies provided 'hotspot' targets in which ground-based electromagnetic (EM) surveys could be completed. These discoveries led to the formation of the Bathurst Mining Camp (BMC); a mining district known worldwide for its volcanogenic massive sulphide deposits. Although not within the BMC, Nash Creek is close enough to have benefited from the extensive geophysical surveying. Table 4 summarizes the geophysical surveys utilized for this study.

Magnetic Data

In 2004, Fugro (now CGG) were contracted to fly a fixed wing magnetic and electromagnetic survey over the Nash Creek area. This survey comprised 272 km of magnetic data, flown with EW lines (088° - 268°) at an average survey height of 120 m. Geotech Ltd. followed up with an airborne survey in 2006 that collected 367 line-km of data. Lines were spaced 150m apart with a sample rate of 10 Hz. These lines were flown in the E-W direction by helicopter at an average height of 65 meters above surface. Tie lines were flown perpendicular to the survey and were used to level the magnetic data. Data processing routines were the standard for this kind of surveying work (heading, lag, levelling, micro-levelling, IGRF). Further details can be found in the respective reports (Fugro, 2004 & Geotech, 2006). The final levelled and micro-levelled total field data were

compiled and gridded at 30m (Ugalde, 2007). In March 2018, Callinex Mines Inc. commissioned an unmanned airborne vehicle (UAV) magnetic survey, which was completed by a local contractor, and the data made available to the University of Toronto Research Group (Cunningham et al., 2018). The drone system allowed for a more detailed survey across the Nash Creek exploration area. It was flown 40m above the surface with flight lines spaced every 30m. This high-resolution survey allowed for larger anomalies to be distinguished into multiple parts. These data were micro-levelled and corrected using similar methods to the surveys discussed above. The total magnetic intensity was gridded at 6m cell size using a minimum curvature algorithm. From the two total field grids, 2D FFT processing was utilized to produce reduced to pole (RTP), first vertical derivative (1VD), and total horizontal gradient (HG) of the RTP grid.

Gravity Data

In 2006, SLAM exploration commissioned a ground gravity survey over the area of study detailed in Figure 4. The survey was conducted in winter (to facilitate access) and included 451 stations using a Scintrex CG-5 gravimeter and a Thales ProMark3 Differential Global Positioning System (DGPS). Horizontal precision ranged from 0.01 m in the open to 2-3 m in more densely forested areas while vertical precision ranged from 0.1 m to 5 m in the respective environment. 5-meter vertical precision is not indicative of the survey and would be better considered an outlier. In general, stations were collected every 10m over potential mineralization, and every 20-30m elsewhere. In 2007, 2017, and 2019, the University of Toronto research group collected gravity data with a Lacoste & Romberg G meter over access trails and a known shallow mineralization target of 180m^2. Drift, latitude, and free-air corrections were applied to determine the free air anomaly. All gravimeter surveys were compiled at this processing level. A Bouguer correction was applied with a density of 2.72 g/cm^3, a standard average rock value. Terrain corrections were calculated using the DGPS elevation data for the area as well as SRTM topography for the outer range. The free air anomaly and terrain corrected bouguer anomaly were gridded at 5m using a minimum curvature algorithm. From this, a regional-residual separation was completed using an upward continuation filter over the complete bouguer anomaly.

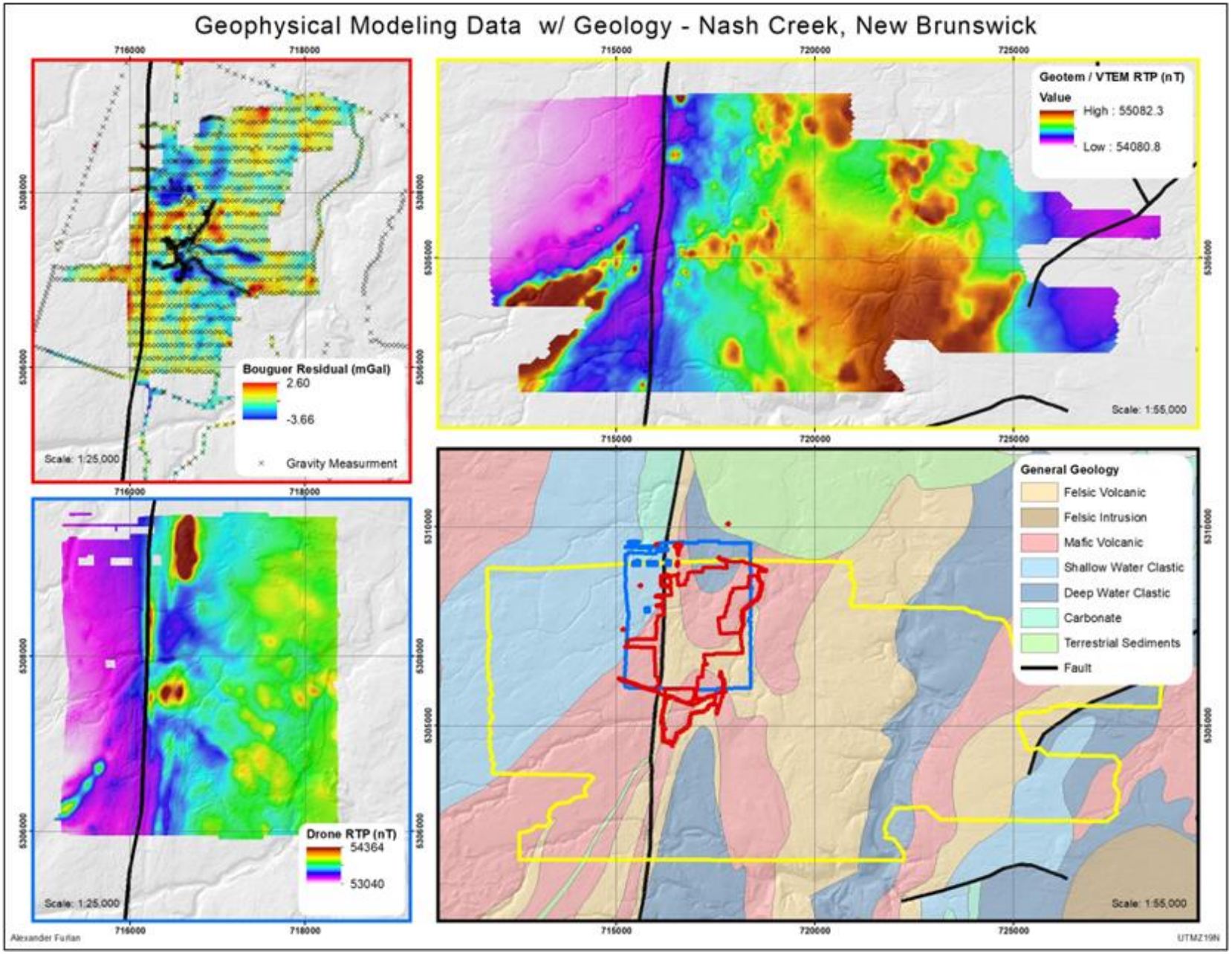

Figure 4 - Compilation of geophysical surveys with generalized geology. RED – Ground gravity data with station locations. YELLOW – GeoTEM / VTEM compilation of total field data. BLUE – Total field data collected using a drone survey system. BLACK – Survey coverage overtop general geology. Each footprint is coloured to match the outline of the appropriate data. Coordinates are projected using UTM Zone 19 N.

Table 3 – Compilation of geophysical surveys that cover Nash Creek, New Brunswick. Table is colour-coded as multiple datasets exist for the same geophysical technique. BLUE – Gravity, PINK – Magnetics, RED – IP/Resistivity, YELLOW - EM, GREEN – Surface data, TEAL – Radiometrics.

Type		Acq. Date	Products	Parameters	System
Gravity	Regional	1944 - Present	Free Air Anomaly, Bouguer Anomaly, 1st Vertical Derivative (1VD), Horizontal Gradient (HG)	230000 observations spaced 1-20km apart (avg 5-10km), Reduced to IGSN71 datum, used GRS80 formula for theoretical gravity values, Bouguer calculated using vertical gradient of 0.3086 and density 2.67.	Compilation (Various)
	Local (UofT/Slam Exploration)	2006	Free Air & Bouguer Anomaly, Upward Continuation, Residual, 1VD, HG	4 GSC stations tied to 11 new region scale stations, 55 stations every 10m over deposit, 20-30m in surrounding area, 55 stations every 2m over known shallow mineralization (180m^2), Reduction: drift, latitude, free-air corrections, Bouguer correction (2.72 used), minimum curvature @ 5m grid size.	Scintrex CG-5, ProMark3 DGPS
Magnetics	Regional	1947 - Present	Reduced To Pole (RTP), 1VD, HG	Gridded at 200m, line spacing of 800m (400m or less since 2000), altitude of 305m, leveled compilation, corrected for arbitrary datums, time variations, and different survey spec.	Compilation (Various)
	Local (Fugro/CGG)	2004	RTP, 1VD	Fixed wing, line spacing 200m, 4305km flown, height of 120m, 40m elevation.	MEGATEM
	Local (Slam Exploration)	2006	RTP, 1VD	E-W flight direction, 150m line spacing (1000m tie lines NS), 323 line-km.	VTEM
	Local (Ugalde, H.)	2017	RTP, 1VD, HG	Compiled by Ugalde, H.	VTEM & GEOTEM
	Local (Cunningham et al.)	2018	RTP, 1VD, HG	E-W flight direction, 30m spacing, 40m elevation.	SkyLance Drone w/ Cesium Vapour Magnetometer
	Local (Veglio, E., Hebert, C.)	2015-2017	RTP, 1VD, HG	Reading every 1s, Base station every 30s, ~3.3 squared km surveyed, not corrected.	Proton Precession Magnetometer
Induced Polarization (IP) / Resistivity	Local (Abitibi Geophysics)	2018	Resistivity & Chargeability Depth Slices	Depth slices derived from 3D resistivity and chargeability models. Models were not available for use.	OreVision IP
EM	Local (Slam Exploration)	2006	Apparent Conductivity	Apparent conductivity is calculated from the channel located 1.13 milliseconds after the termination of the impulse.	VTEM
Surface	Regional	2016	DEM	DEM derived from airborne LiDAR point cloud (.las). Available at 1m & 2m, vertical datum CGVD2013.	LiDAR
	Local (Furlan, A.)	2018	Hillshade, Curvature	Created using GIS software.	ArcGIS Pro
Radiometrics	Regional	1969 - 2011	U/Th/K Composite Images	Compilation of 370+ gamma-ray surveys. 50L of Sodium Iodide detectors flown at 120m. Line spacing varies from 200 – 5000m.	Compilation (Various)

Surface Topography

In 2015, New Brunswick started its LiDAR mapping project that would eventually cover the entire province. At Nash Creek, the LiDAR data was available at 6 points per square meter along with a digital elevation model (DEM) gridded at 1m (Service New Brunswick, 2016). This DEM was used to create a hillshade for visualizing topography with the geophysical and geological datasets available for use. A curvature raster, which calculates the second derivative of a topographic surface in each cell based on the surrounding 8 cells was also computed using ArcGIS. A curvature raster combined with high resolution topography data can highlight or emphasize structural features with surface expressions (Zeverbergen, 1987). Being a second derivative, a curvature raster is susceptible to noise, but low pass filtering can help eliminate artefacts.

Additional Data Sources

An extensive radiometric dataset is available for Canada which covers the survey area. Potassium (K), thorium (Th), and uranium (U) counts are used to identify rock types and contacts between units (Geological Survey of Canada, 2017). A DCIP survey was completed in 2018 by Abitibi geophysics, but raw data is not publicly available. Depth slices of the resulting 3D resistivity & chargeability models were used to help identify conductive bodies, how they vary with depth, and the structure present.

2.4 – Modelling

Modelling Nash Creek was a multi-staged process making use of the software packages ModelVision and GeoModeller. To simplify the 3D approach, 2D sections were first created along the modelling lines mentioned in Section 2.3. ModelVision allows the user to create 2D cross-sections along traverses that are optimized by given geophysical or geological data (Tensor Research, 2018). These sections included rock units seen in the geological maps, created geophysical responses that matched the responses sampled to the database, and use borehole logs to constrain geology in the subsurface. While ModelVision provides a good starting point, it only allows for uniform property distributions across a modelled body which may contain multiple lithologies. Furthermore, rock density & magnetic susceptibility are greatly affected by metamorphism & deformation leading to property variations within the same unit. Nash Creek has a complex deformation history so assigning one value to an entire formation is too simplified. To counteract this problem, modelling was finished in GeoModeller. This software allows the user to

set a distribution of physical property values within a unit instead of defining it entirely by one value. The 2D sections constructed in ModelVision, along with surface geology (Wilson, 2013), were used to build the 3D model in GeoModeller. This software assembles geological and geophysical data into one by building complex and implicit 3D geological models based on previously collected borehole, geophysical, and petrophysical data (Intrepid, 2012). It allows the user to interpolate and extrapolate a 3D model from 2D cross-sections while providing a plan view of the survey area to determine where lithological and structural contacts may lie at the surface. The resulting model is geologically reasonable while respecting the physical rock properties that were measured in the field. Lastly, this geological model was inverted to determine magnetic, gravitational, and lithologic distributions in the subsurface and further elucidate our understanding at Nash Creek.

2.4.1 – 2D Sections

Non-uniqueness describes how the same geophysical signature can created synthetically by an infinite number of models (Dentith & Mudge, 2014). To counteract this, 2D sections were created using constraints imposed by a combination of petrophysical rock properties, borehole logs, geophysical surveys, and geological maps (Figure 5). First, geological, and structural contacts were traced from the surface geology map (Wilson, 2013) onto the model sections. These contacts act as near-surface vertices for the modelled bodies. Large features on the geological map, such as the Jacquet River Syncline, guide the general shape of bodies between sections. Borehole logs from over 40 years of exploration were used to constrain the models at depth (Figure 2). Borehole logs were ranked based on their distance from each section, with preference placed on boreholes located directly along the model line. These core logs were used to control the sections at depth but with some caveats. First, some lines had more borehole coverage than others. Line 6 has one borehole located within 25 meters while line 3 had sixteen. Along the less populated lines, matching density and magnetic susceptibility signatures was given priority over matching borehole geology (Figure 6). Here, the issue of uniform properties within a model rears its ugly head. Some modelled units encompass a large portion of the model and no amount of adjusting a single density or magnetic susceptibility value would improve the fit without drastically the units. While this is a viable option for models with minimal prior information, formation descriptions provided by the province also include unit thicknesses that were adhered to. Some formation descriptions had the thickness at Nash Creek reported, but others were interpreted from the entire unit.

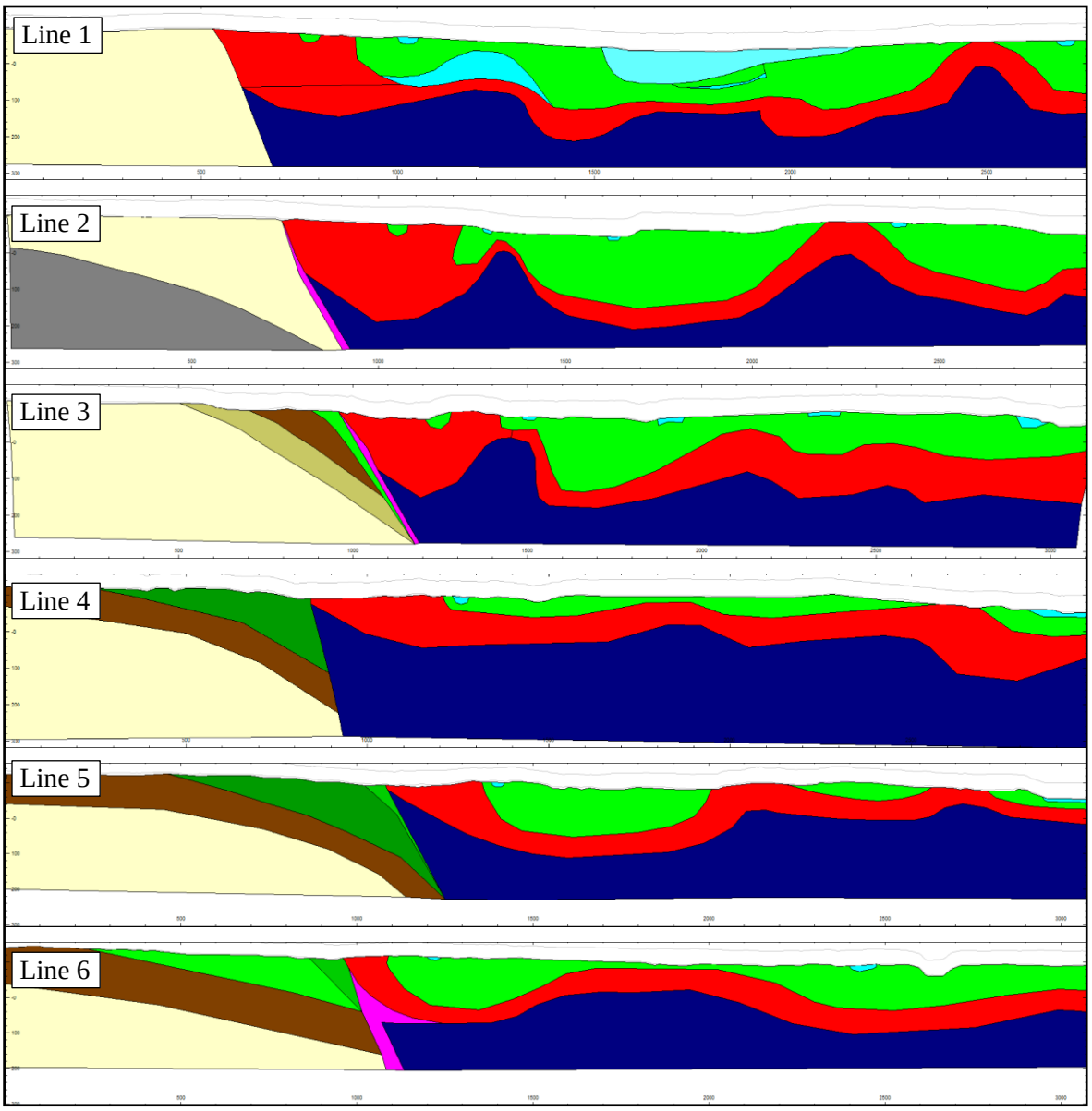

Figure 5 – 2D sections created along model lines 1-6 as seen on Figure 2. Units are represented with the same colour as Figure 2 (Wilson, 2013) except for the dark blue and pink unit. BLUE: generic rock type meant to encompass an average density and susceptibility value of all rocks not seen in the surface geology maps. PINK: Intruded dykes along the BPAB fault.

The second caveat comes from the structural complexity of the Nash Creek area. As mentioned in Section 2.2, this region has undergone several stages of deformation. This deformation is compounded by stages of interbedding volcanic and sedimentary units (resulting from the shallow shelf environment). This repeated sequence is reflected in the borehole logs but cannot be accurately modelled within ModelVision. To counteract this problem, general trends of lithology were used instead of trying to match each interval described in the core logs. Lenses of sedimentary rock within volcanics units were lumped together assuming the bulk physical properties of the

volcanics would dominate the signal over the clastics. Magnetic susceptibility and density were the two physical properties modelled. Other geophysical datasets were available, but coverage was lacking, or the data were not compatible with ModelVision. These datasets were instead used in a supplementary manner. Each modelled body was assigned a density and magnetic susceptibility to match the geophysical signatures along each section. These values were based on the petrophysical studies done by previous researchers (L'Heureux, 2007; Bongajum, 2013; Veglio, 2017 & Hebert, 2018). When modelling, the average density and magnetic susceptibility values for each unit were used as a starting point and adjusted as needed (Table 3). Once each model fit the data reasonably well, the sections were exported as images. From here, these images were georeferenced along each model line and used as a guide for 3D modelling in GeoModeller.

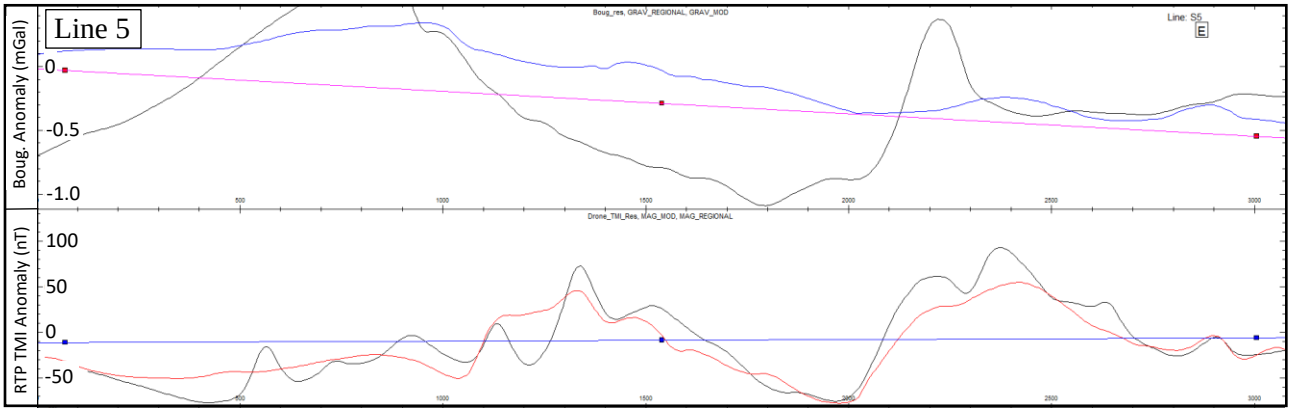

Figure 6 – Modelled and observed Bouguer gravity and RTP total field responses for Line 5. (TOP): BLACK: observed data (Bouguer residual), BLUE: modelled Bouguer residual, PINK: regional gravity field. (BOTTOM): BLACK: observed data (reduced to pole total field), RED: modelled RTP total field, BLUE: Regional RTP total field. Poor fit in some areas could be explained by the assumptions made while modelling (such as lumping packages together).

2.4.2 – 3D Modelling

Unfortunately, ModelVision could not assign a range of values to a single unit. For example, where interbedding exists at the survey site, the same density is assigned to the entire package. This proves too unrealistic when dealing with the highly interbedded and deformed rocks of the Chaleur Bay Synclinorium. GeoModeller addresses this issue by inverting sone initial model the user constructs into a voxel model. Each cell within a voxel model can be assigned a magnetic susceptibility or density value based on the property distribution given by the user. This allows for greater variability within a unit that may have deformation or altered sub-units within.

Before producing this voxel, an initial geological model must be constructed. Stratigraphic and structural relationships are important to establish so each 2D section were imported as a

georeferenced image. The section images were then used as a baseline to trace structural and unit contacts into the 3D model. A stratigraphic package was constructed within GeoModeller to prevent the 3D model from creating an impossible lithology when interpolating between 2D sections (Figure 7). Along with the stratigraphic relationships, structural relationships were also established about the BPAB fault. Figure 7 shows which lithological units intersect the fault and when constructing the initial model, it will make sure that BPAB fault cuts through all these units.

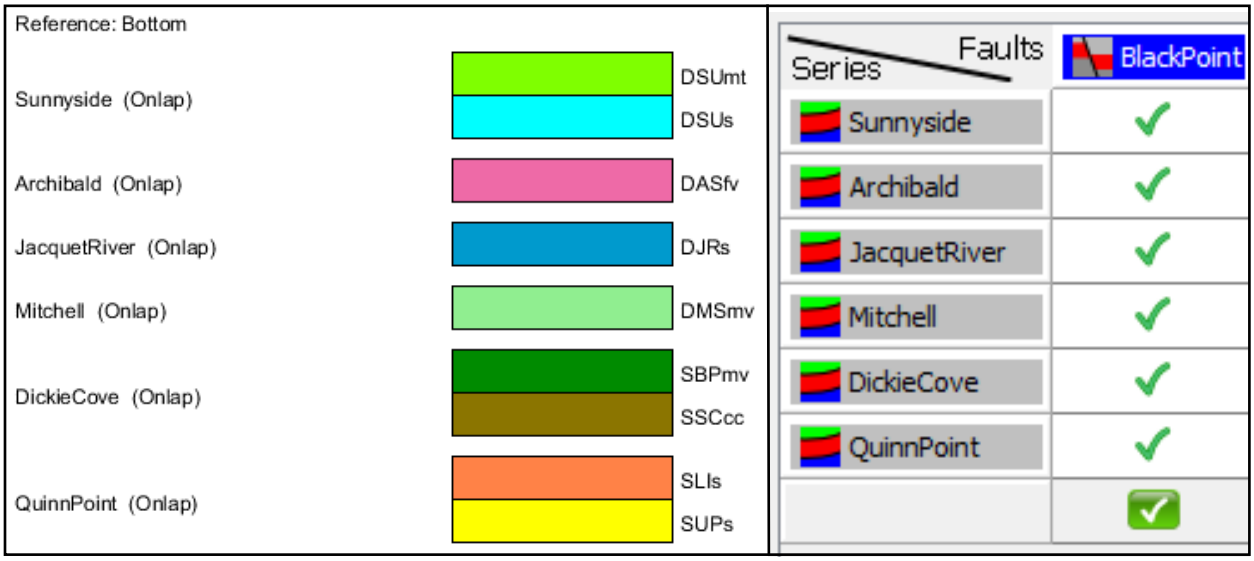

Figure 7 – (LEFT) Stratigraphic package used for 3D modelling. While extrapolating the model from our 2D sections, this would keep units in the correct order according to the law of superposition. (RIGHT) Recording of the Black Point Arleau Brook Fault and the units it transects. When the fault was modelled, this would assure all units selected were offset by the fault.

This feature allows us to have Silurian and Devonian formations juxtaposed across the fault. Using bedrock geology maps, unit contacts were also traced onto the surface of the 3D model. These contacts guide unit distribution *between* sections when interpolating the initial model. The combination of contacts (both in section and plan) gives our model constraint in all 3 dimensions and will act as 'true' model points for the inversion algorithm. Figure 8 shows the interpolated initial model. A plan view of this model (Figure 9) is similar to the surface geology map (Wilson, 2013) but with a few clear dissimilarities. One example is the inclusion of Jacquet River sediments at the surface, south of line 5. This unit was not adequately modelled and its distribution in the subsurface is unlikely to be as seen in this 3D model. Ideally the model would match the surface units, but for this thesis, not as much weight was given to matching the contacts at surface. With minimal outcrop, thick overburden, and several deformation events, this distribution of units leans heavily on the interpretive side. Formation thicknesses were taken into account when constructing the 2D sections, but the interpolated 3D model does not, and some units might be thinner or thicker.

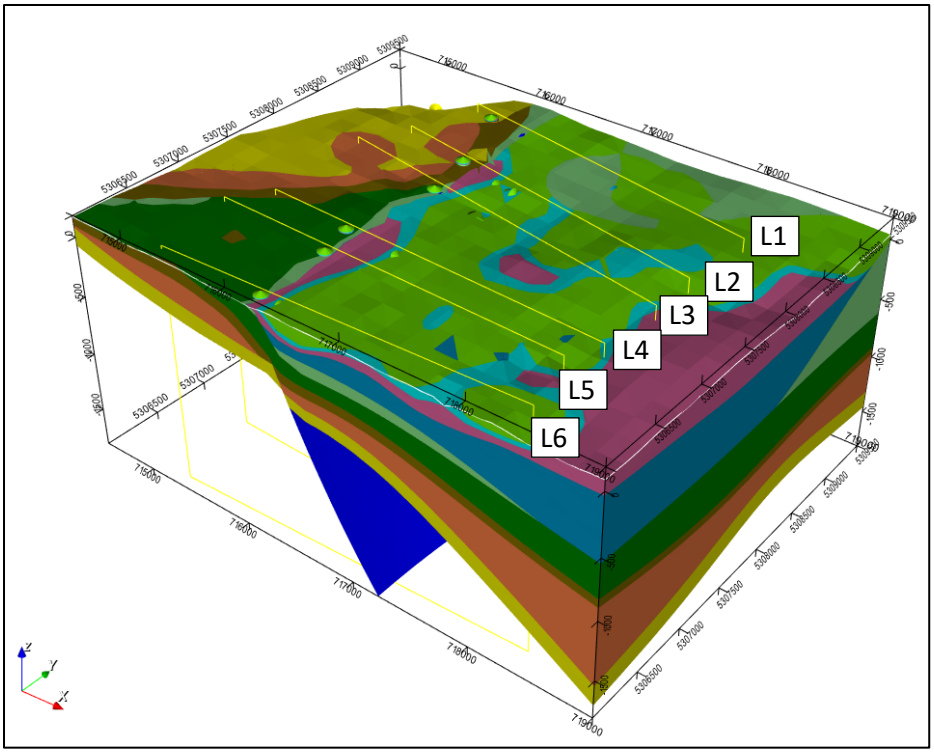

Figure 8 - Full 3D lithological model of Nash Creek. Model colours match stratigraphic package shown in Figure 7. Yellow lines indicate location of 2D cross sections.

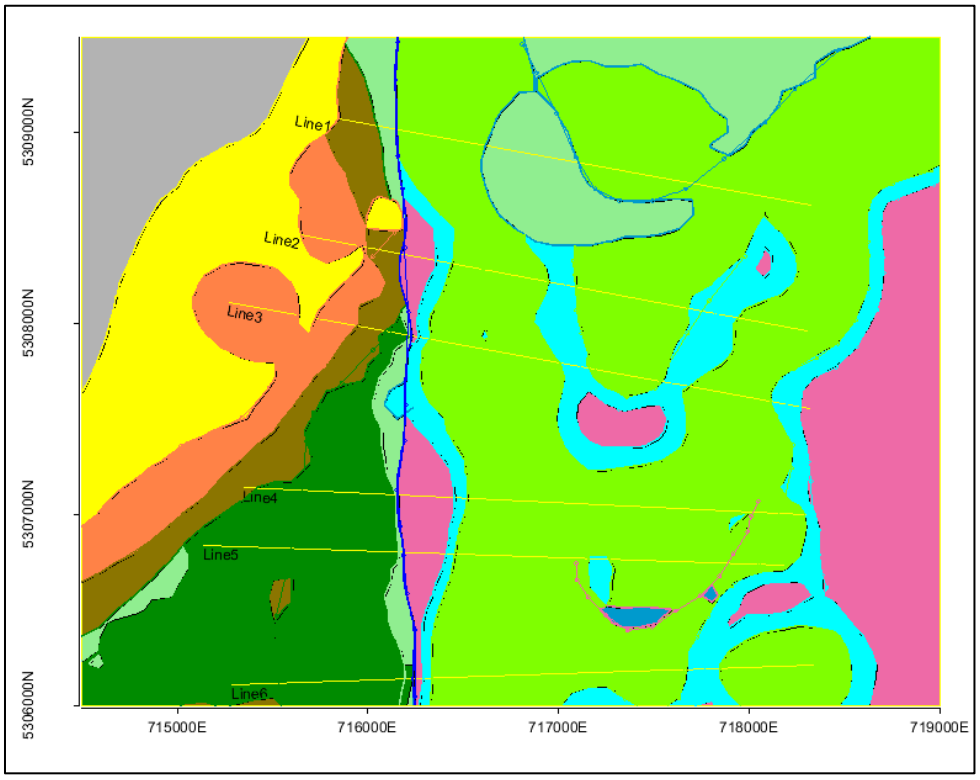

Figure 9 – Plan view map of 3D lithological model. See Figure 7 for colour table to identify stratigraphic packages. While similar to Wilson (2013), there are quite a few anomalous patterns stemming from interpolation. Ex) Jacquet River Sediments (JRS) seen at surface south of line 5. Projected coordinates are NAD83 UTM Zone 19N.

With the initial model constructed, physical property distributions were assigned to each unit. These distributions are based on petrophysical measurements collected at Nash Creek and give each unit a range of density and susceptibility values that can be assigned to individual cells within the unit (L'Heureux, 2007; Bongajum, 2013; Veglio, 2017; Hebert, 2018). At this point, our initial model is complete, and a stochastic inversion can be used to refine our geological model using the density and susceptibility ranges outlined above. In GeoModeller, the stochastic inversion will be computed 100,000 times wherein each iteration with adjust the properties to improve the gravity and magnetic data misfit. It is important to note that the structural and stratigraphic relationships established in the initial modelling phase are respected through the inversion process.

Figure 10 shows the results of the inversion in cross-section view along line 5. The models labelled as 'Final' in this figure are voxels, and their 'blocky' appearance is a result of the cell size. Where our initial model had a single set of properties for each unit, voxels must assign individual susceptibility, density, and lithology properties to each cell. Considering our subsurface contacts were traced along the 2D sections, it is not shocking that the final lithological model would be nearly identical along the profile. The least well-defined boundary in the final lithological model is between the Archibald Settlement & Jacquet River Formations. For the most part, the Jacquet River sedimentary unit has been made thicker at the cost of the Archibald Settlement mafics (Figure 10 – red box). While not necessarily incorrect, the distribution of the Silurian units east of the fault fails to show any synclinal shape. Since no 2D modelling was done of the Silurian units to the east of BPAB fault, their distributions are simply layered, dipping to the east. Since we are in a syncline, we would expect these units to flatten out and approach the surface further to the east. The 3D model extends approximately 2 kilometers east from the BPAB fault while the Silurian units located immediately west of BPAB are not seen in the east for 6 km. It is entirely possible then that the Silurian units will continue for another 4 km and within this space, complete the synclinal form, outcropping east of the survey site. Along with the lithological model, density and susceptibility models were also created (Figure 11). Unfortunately, the distributions of physical properties derived from petrophysics have substantial overlap and thus, distinguishing the lithological units geophysically is troublesome. This issue was compounded by our inversion parameters where instead of gradual variation within units, we see one dominant density or susceptibility value with minor, single cell, deviations.

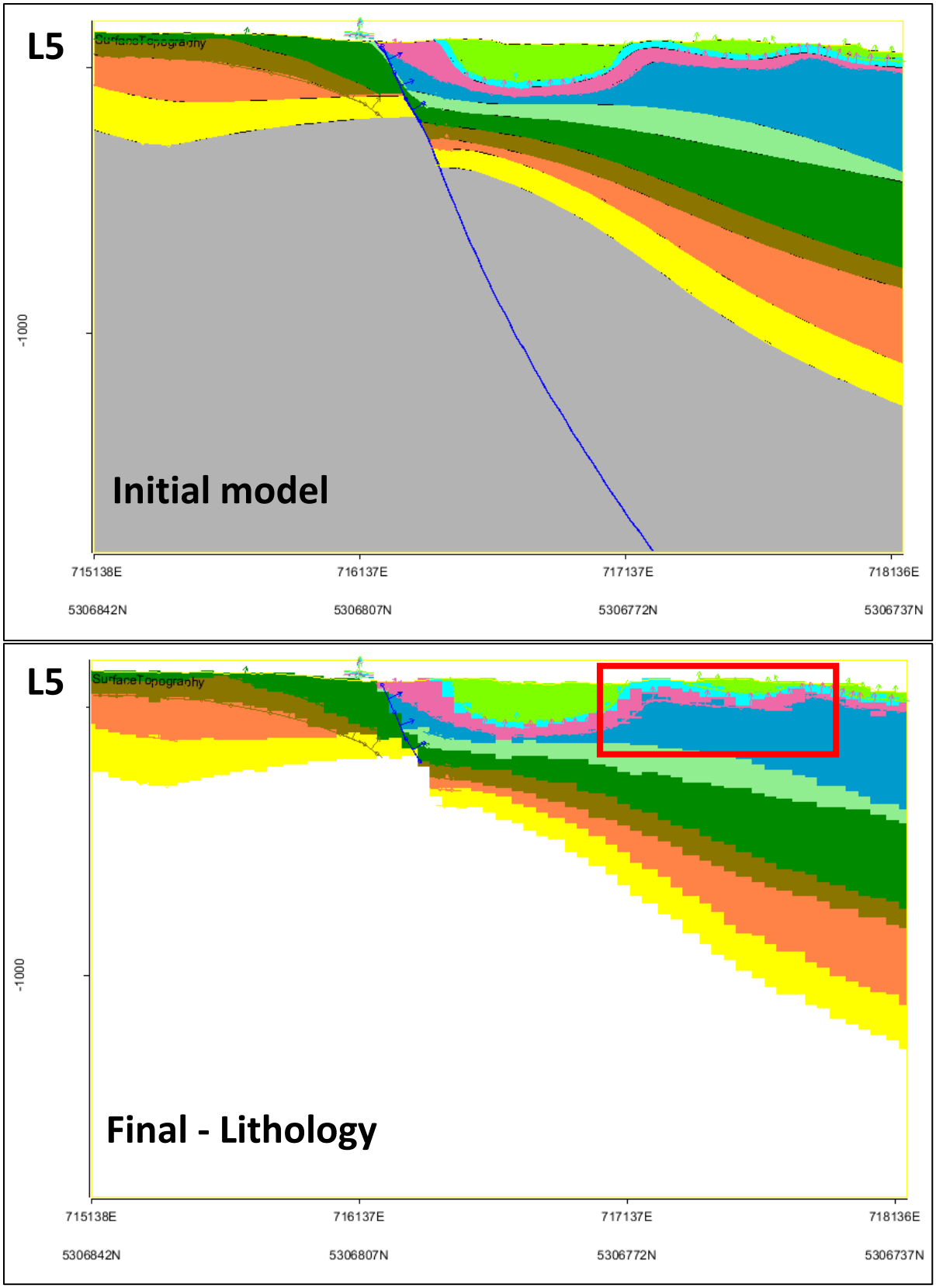

Figure 10 - Initial & Final lithological models for Line 5. See figure 7 for colour table. Red box highlights the discontinuous mafic unit mentioned in the text. Projected coordinates are NAD83 UTM Zone 19N.

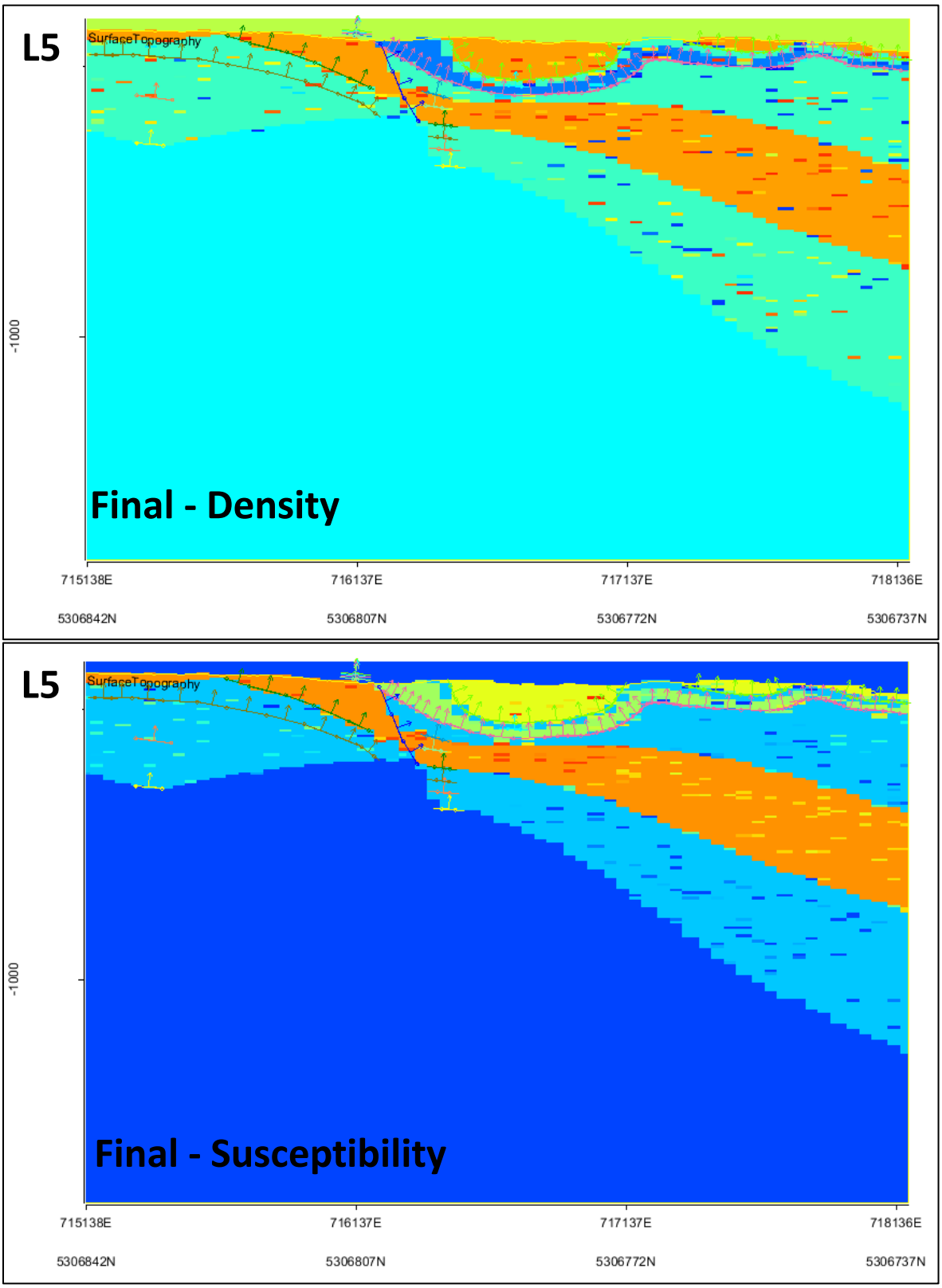

Figure 11 – Final density and magnetic susceptibility models. Colour bars are not shown but warmer colours indicate greater magnitude. Speckle pattern arises from the stringent inversion parameters not allowing smoother variability. Projected coordinates are NAD83 UTM Zone 19N.

2.5 – Discussion

The application of 3D modelling using previous geophysical and geological datasets was, in part, a success. The 2D sections and 3D models were constructed using realistic magnetic and density signatures by choosing their range of values from petrophysical measurements. One glaring issue with this project are the inverted property models produced by GeoModeller. Access to this software was lost during the COVID-19 pandemic and as such, no further improvements could be made on the initial geological model, or the inversion parameters used. While property models were created, the parameters used for this initial stochastic inversion were too stringent, not allowing enough variation in the values. Although we had density and magnetic susceptibility ranges from past petrophysical studies, these ranges needed to be expanded and allowed more overlap in values to be closer to the true model. The deformation at Nash Creek inherently means clear contacts will be hard to find but we see several in the inverted property models. More time with GeoModeller, or similar software, would allow us to further optimize the geological model while improving the inversion parameters to better match what is seen at the deposit in Nash Creek.

Differences between the modelled response and the signatures used to derive the model can be attributed to several factors. First, discrepancies between measured rock properties, borehole geology, and the geophysical signatures did not allow for the constructed models response to match the magnetic and gravity surveys perfectly. The 2D sections and 3D model were created using geophysical data as a supplementary dataset to support what geology was seen in the borehole data. Second, the complexity of Nash Creek could not be captured in the geophysical and geological datasets. Nash Creek has undergone substantial deformation multiple times throughout history. This complexity can be seen in the borehole data where lenses of sediments are intercalated with basalt units. These lenses impact the geophysical signature but are near impossible to model using the methods chosen for this report. In such circumstances, an estimate of bulk density and magnetic susceptibility were used to inform the model, deviating from the true model. Lastly, dykes exist in the survey area (Veglio, 2017) but their path to the surface is still unknown. It has been speculated that the late-stage dykes at Nash Creek used the pre-existing BPAB fault as a conduit to reach the surface. If this were the case, it would explain the strong magnetic anomalies that could not be modelled without including a highly magnetic unit not described in any of the regional geology maps. To better understand the morphology of these dykes, the BPAB fault must be understood as well (Figure 12). Currently, there are no strike & dip measurements available

directly on the BPAB fault. Using the contact between the Silurian and Devonian units within the 3D model, the BPAB fault was traced, with the dip range derived from this interpolated surface. A potential range of dips from 56 to 74 degrees East are seen, in line with what we would expect for a graben-like structure. Given the fact there is no outcrop in this region, some geophysical surveying over the fault would be ideal for constraining this structure at depth. Seismic methods could be applied but increasing the depth of investigation is costly. Another method with an ideal depth of investigation is Extremely Low Frequency (ELF) EM. Since conductive fluids tend to travel along pre-existing structures, an EM survey could provide better constraint on the dip of the fault, and depth extent as well.

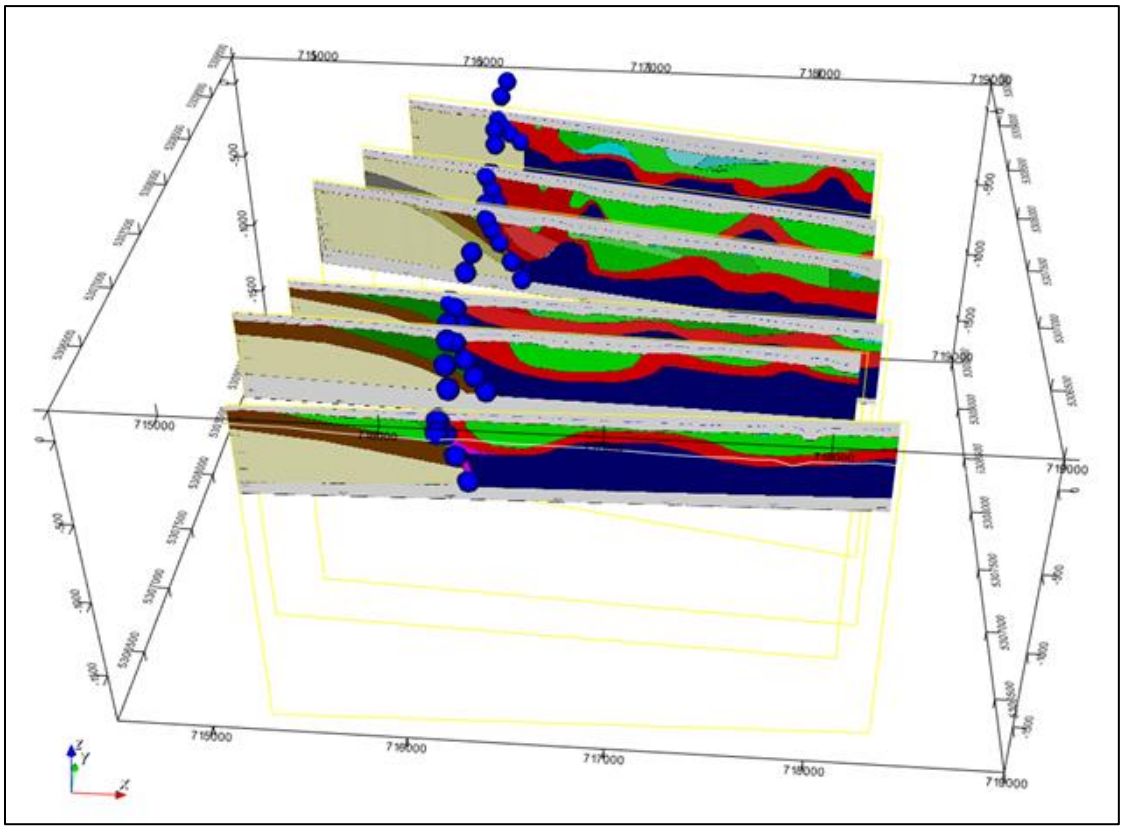

Figure 12 – 3D model space with 2D cross-sections and BPAB fault trace. Fault trace was interpolated (blue dots) using the sections & the modelled contact between the Silurian and Devonian units. Dip values ranged from 56 to 74 degrees, but further constraint of these values at depth would help our understanding of the fault morphology and the Nash Creek sulphide deposit. Projected coordinates are NAD83 UTM Zone 19N.

2.6 – Conclusions

3D modelling allows us to construct a representation of the subsurface using the knowledge available to a researcher. As technology advances, different types of datasets can be included in the modelling process to provide a more accurate simulation. This was seen throughout chapter 2

as multiple datasets were used with ModelVision and GeoModeller to create lithological models. These models, both 2D & 3D, accounted for borehole geology as well as geophysical signatures from the plethora of airborne and ground-based surveys collected over the Nash Creek deposit. The end goal of modelling was to elucidate a better regional understanding of the Nash Creek area. Unfortunately, the complexity of modelling and clerical issues limited what could be inferred. Substantial overlap between physical properties and intercalated units makes modelling different units an arduous task. Line 5 from figure 5 shows 3 units (aside from the minor surface unit) make up the modelled response on the eastern side of BPAB fault. Figure 6 shows the modelling data for line 5 where a mismatch between the observed and modelled density is seen. Since these units extend eastward to the end of the section but the mismatch is only a few hundred meters, there is too much unaccounted variation in the subsurface. If modelling stayed in ModelVision, a solution could be to break the larger units into smaller units with similar, but different densities (or magnetic susceptibilities). This poor fit could also be an indication that some geophysically important unit is not being modelled. Little drilling has been done near line 5 (see figure 2) and as such, a subunit might be responsible for this decrease in density. Since the mismatched gravity is roughly in line with the fold axis of the JRS, it could also be that a greater percent of low competency rocks found their way into the nose of the fold during deformation. Nearby core logs (between 50 to 100 m away) show intercalated units, so the density discrepancy could indicate there is a westerly transition from sedimentary dominant to mafic dominant within the Sunnyside Formation. The most interesting elucidation came from the 3D model where a range of dips were derived from the BPAB fault. Thick overburden and a lack of outcrop prevents direct measurement of the fault and as such, geophysical modelling of the contact provided dip values ranging from 56 to 74 degrees. The contacts associated with BPAB fault are not linear, so a line of best fit was needed to digitally measure the dip. Veglio (2017) hypothesized the BPAB fault at Nash Creek acted as a conduit for hydrothermal mineralization and later, the dykes parallel to the fault. These dykes are believed to have ceased hydrothermal fluid flow at Nash Creek, killing the precipitation of sulphides. So, while the BPAB fault did not influence the initial deposition of sulphides, it would later provide a key fluid pathway for sulphides to precipitate into fractured rocks.

It is recommended that further geophysical surveying is completed to constrain the dip and depth extent of the fault. The IP/resistivity depth slices mentioned in Section 2.3.2 show a conductive contrast across the fault (Figure 13). While the full model was not accessible, it was only modelled

to 200 meters below sea level. Since our interest is constraining the fault at depth, methods like ELF-EM would be ideal. Unlike seismic methods, which requires a greater energy source and larger array to see deeper, ELF-EM is a passive system that can survey several kilometers into the subsurface. While ELF-EM is not new, the raw data (known as tipper data) does not provide a physical property (in this case, conductivity) directly. For tipper data to relate to conductivity, it must first be inverted. Currently, this method of analysis is limited by the software required for inverting ELF data. Chapter 3 aims to construct an inversion workflow that uses open-source software for maximum compatibility and produces reliable conductivity models that can be used to evaluate structures and conductive features at depth, like those seen at Nash Creek.

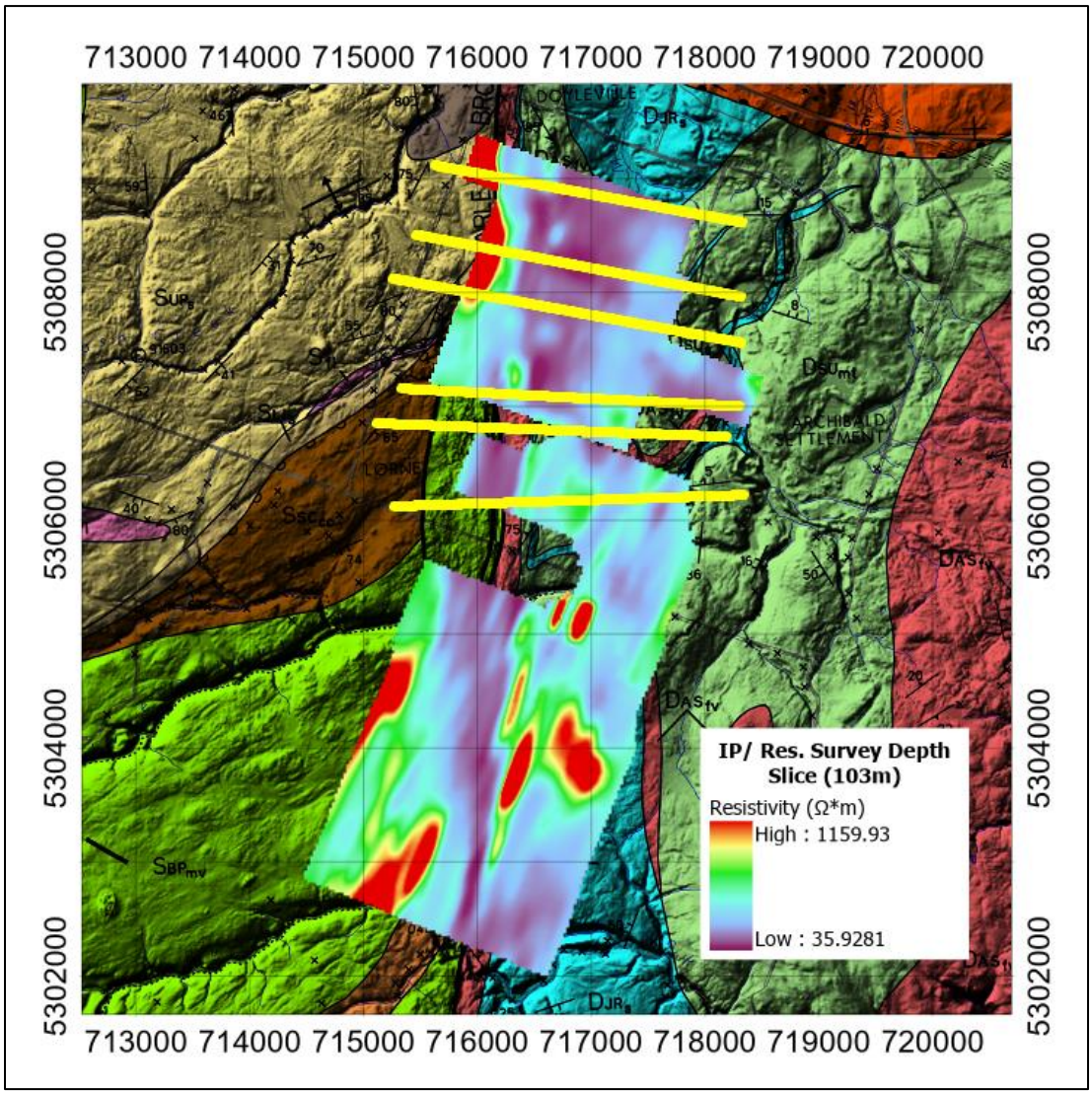

Figure 13 - Resistivity depth slices at 103m deep. Yellow lines indicate Nash Creek modelling sections used for this thesis. Clear break in resistivity is seen along the fault indicating a good contrast that could be imaged by other resistivity mapping systems. Projected coordinates are NAD83 UTM Zone 19N.

3.0 - ELF & SimPEG Inversions – Key Anacon VMS Deposit at Bathurst, NB

3.1 – Introduction

The previous chapter showed how synthesising multiple datasets is an effective tool for building a reasonable 3D geological model. While the model provided some insight into the Sunnyside Formation, a lack of information about the BPAB fault hindered analysis of the region. This fault is a large, regional scale feature that played an important role as a pathway for hydrothermal fluids. Constraining this fault geometrically would improve our understanding of the Silurian-Devonian contact. How deep the fault extends into the earth, as well as how shallow or steep the dip is, will impact how fluids use this fault as a pathway. If a significant conductivity contrast was to exist, say from remobilized sulphides about the fault, EM methods could use that contrast as a conductivity 'tracer'. This process is akin to a Cine Esophagram; a medical test where a barium solution is ingested, and x-rays are taken of the patient. The barium solution interacts with the x-ray radiation to create a clear image of the gastrointestinal (GI) tract. The pathway taken by the barium solution (hydrothermal fluids) through the body (host rock) can be traced and used to study the size and shape of the GI tract (fault). When selecting a follow up geophysical survey, the method must be able to penetrate thick overburden to investigate the structures below. Magnetotelluric (MT) surveys not only have the depth extent needed but highlight 3D conductivity structures. Typical MT surveys are lengthy and expensive, but a 'little brother' to MT exists known as ELF-EM. While comparatively inexpensive to collect, ELF data was limited by the software available to invert it. Recently, however, an open-source inversion package known as 'Simulation and Parameter Estimation in Geophysics' (SimPEG) has become a viable option for inverting ELF data. The following chapter outlines a new workflow used to produce 3D conductivity models from tipper data. A python script nicknamed 'Santa's Workshop' was written to streamline importing, formatting, and inverting ELF data. A sample ELF dataset was collected over the Key Anacon VMS deposit (Bathurst, NB) to test the new code. The SimPEG-derived models were compared to existing wireframes of the sulphide horizons. These wireframe models were derived from borehole logs and geophysical data making them ideal for comparison. The results of this test survey show that conductive bodies can be accurately modelled, even with a small dataset.

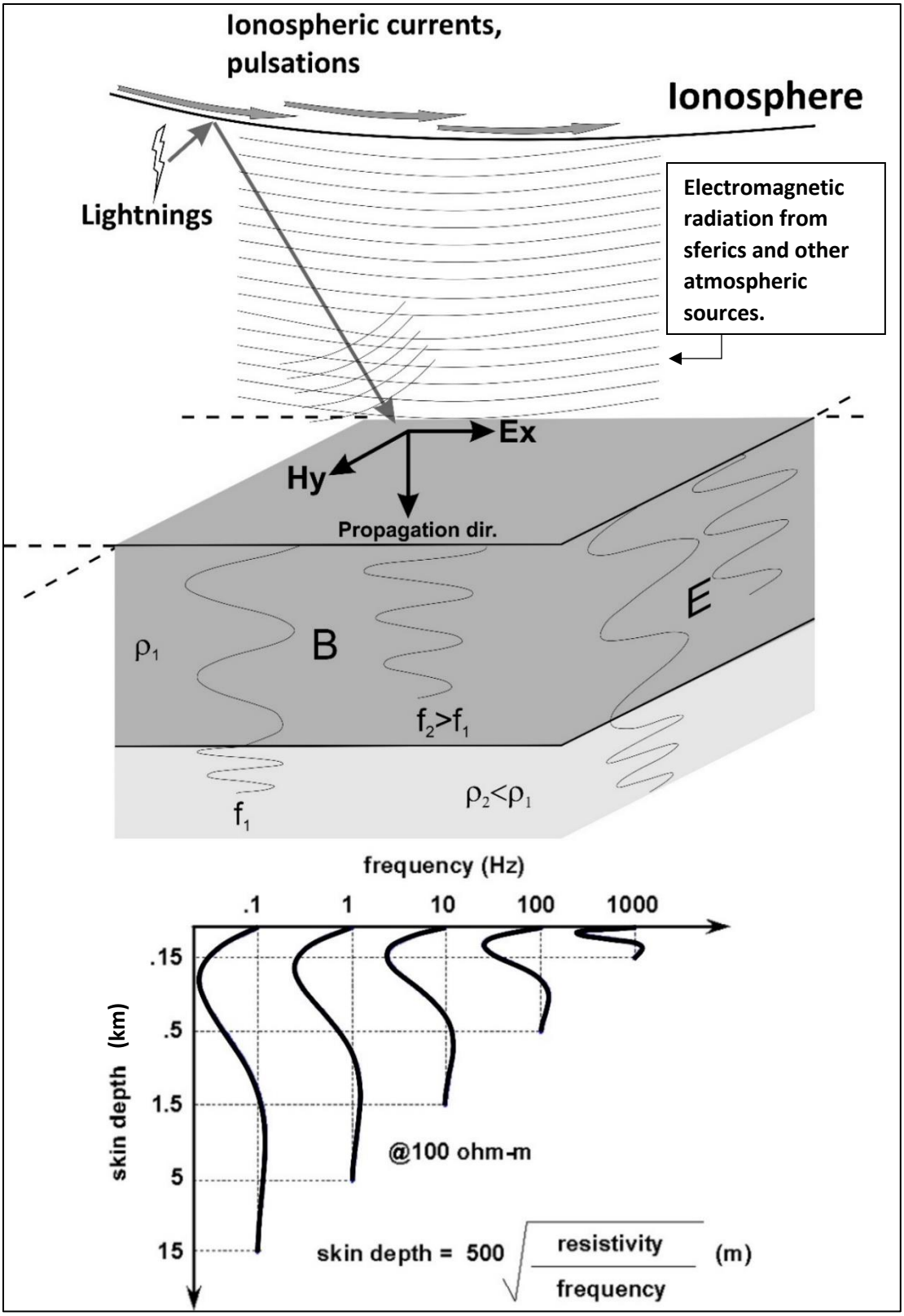

Figure 14 – The 'everything' figure for MT. (TOP) Shows energy sources for MT data and how they interact with the surface. Higher frequency of the wave or lower resistivity of the subsurface means less depth penetration. (BOTTOM) Shows how skin depth, or the depth to which we can detect changes, is related to both the frequency & resistivity of the subsurface. This is simplified to only account for non-magnetic spaces.

3.2 – Magnetotellurics & Tipper Theory

Magnetotellurics (MT) is a passive EM exploration technique that utilizes naturally produced electrical currents (tellurics) to study the resistivity structure of the subsurface (Simpson & Bahr, 2005). Most EM systems require a controlled source (i.e., 'active' EM), but MT takes advantage of the natural, time-varying geomagnetic field (Figure 13). Several researchers (Tikhonov, 1950; Rikitake, 1950; Cagniard, 1953) independently eliminated the problem of an unknown source amplitude by relating the ratios of orthogonal, horizontally polarized electric- (E) and magnetic- (H) fields to the resistivity profile beneath the measurement. By this method, the conductivity structure of the Earth can be determined at depths ranging from tens of meters to several hundred kilometers. In most environments, two factors impact the depth of investigation: the lowest frequency of investigation / longest period measured (dependent on recording time), and conductivity of the subsurface:

$$\delta = p(T) = \sqrt{\frac{T}{\pi \mu \bar{\sigma}}}$$

where δ or $p(T)$ is the skin depth in meters. Skin depth is the depth at which the measured field has attenuated to $1/e$ of the original amplitude. T is the period, μ is magnetic permeability, and $\bar{\sigma}$ is the average conductivity of the penetrated medium. This equation can be simplified in two ways: by using the permeability of free space, μ_0, where $\mu_0 = 4\pi \times 10^{-7}\ {}^{\mathrm{N}}/_{\mathrm{A}^2}$ and applying the relationship between period and frequency ($T = 1/f$). The constant μ_0 is most appropriate in rocks that are dominantly non-magnetic. With this assumption, the more useful skin depth equation is:

$$\delta \approx \frac{503.8}{\sqrt{\bar{\sigma} f}}$$

Where f is the frequency of the incident wave and $\bar{\sigma}$ is unchanged. From this equation, skin depths can be estimated for different frequencies (Figure 13). For a test measurement over a uniform granite body ($\bar{\sigma} = 10^{-3}$ S/m), we would expect a 1000 Hz wave to penetrate ~16 meters before the signal were too weak to distinguish it from the background. While traditional MT methods require measuring the electric and magnetic fields, Schmucker (1970) first described a transfer function that linked the horizontal (H_x, H_y) and vertical (H_z) magnetic field components to conductivity

changes in the subsurface (i.e., a magnetovariational measurement). Jansen & Cristall (2017) described this relationship as:

$$H_z = T\vec{H} = (T_{zx} \quad T_{zy})\begin{pmatrix} H_x \\ H_y \end{pmatrix}$$

Where H_z, H_x, H_y are magnetic field components, and T_{zx} & T_{zy} are dimensionless ratios (commonly referred to as tippers). Tippers get their name by 'tipping' the magnetic field vector away from horizontal in response to 3D conductivity variations. T_{zx} & T_{zy} are two unknowns in the same equation and as such, require two independent signal event polarizations as outlined by Holtham & Oldenburg (2010):

$$T_{zx} = \frac{H_y^{(2)}H_z^{(1)} - H_y^{(1)}H_z^{(2)}}{H_x^{(1)}H_y^{(2)} - H_x^{(2)}H_y^{(1)}}$$

and

$$T_{zy} = \frac{-H_x^{(2)}H_z^{(1)} + H_x^{(1)}H_z^{(2)}}{H_x^{(1)}H_y^{(2)} - H_x^{(2)}H_y^{(1)}}$$

Where (1) and (2) each denote an independent polarization. The resulting ratios are complex (having both in-phase & quadrature components). If measurements were taken across a strong conductivity contrast, it would result in a positive T_{zy} value on one side and a negative T_{zy} value on the other (in other words, a cross-over anomaly). Similar to controlled-source VLF, tipper data allows a conductor to be detected between sparsely located stations. One caveat is that compact 3D bodies have significantly diminished tipper responses compared to 2D geological strike features (Wannamaker et al., 1984). This makes MT ideal for large- to regional-scale conductivity structures. Most of the usable MT signal is generated by lightning activity (i.e., sferics) near the equator which propagates as a plane wave between the Earths surface and ionosphere (Figure 13). These layers act as a waveguide resulting from their strong conductivity contrast. The result is a broadband signal which can be decomposed, analyzed, and interpreted using a variety of geophysical techniques.

Figure 15 – Photo of an AFMAG prototype which would lay the groundwork for ZTEM surveying (airborne ELF). Photo was modified from Legault (2012).

3.3 – Surveying & Instrumentation

The earliest system to exploit natural magnetic fields operated in the audio frequency range (20 Hz – 20,000 Hz), was aptly named Audio Frequency Magnetotellurics (AFMAG) (Ward, 1959). Separating the time- & space-variance of the measured fields was a fundamental issue that led to the use of a comparative measuring technique (Section 3.2). This system was implemented under the assumption that time variations affected the sensors identically, while space variations did not (Ward et al., 1966). Further development of the MT method and AFMAG system resolved many limitations preventing the efficient collection of tipper data (Vozoff, 1972; Labson et al., 1985). Improvements to instrumentation & data processing allowed a broader adoption of these methods among researchers. Labson et al. (1985) had the breakthrough of using cross-spectral estimates of T_{zx} & T_{zy}, resulting in data that was free from the auto-spectral noise component inherent in tipper data. This approach would be known as the 'reference tipper method', a more simplified representation of AFMAG data (Prikhodko, Kuzmin, & Bagrianski, 2020). Roughly 20 years later, this method would be successfully implemented with the development of ZTEM (Z-Axis Tipper Electromagnetics), an airborne AFMAG system (Figure 14) (Kuzmin, Lo, & Morrison, 2005). ZTEM measures the vertical magnetic field component from an airborne receiver while measuring horizontal components of the same field at a base station (Lo & Zang, 2008). A time series is recorded at 2 kHz, binned, and processed to generate six transfer functions between 30 Hz and 720

Hz using a Fast Fourier Transform (FFT). Tipper vectors are extracted from the in-line (T_{zx}) and crossline (T_{zy}) components of the signal. This results in 4 components: in-phase T_{zx} (rE), quadrature T_{zx} (iE), in-phase T_{zy} (rN), & quadrature T_{zy} (iN) across 6 frequencies between 30-720 Hz. To account for the noise induced by the tilting of the airborne receiver, 3 GPS modules are positioned on the loop and track its movements for later corrections (Geotech Ltd., 2013). The incident waves used for ZTEM surveying are within the Extremely Low Frequency (ELF) band of the EM spectrum (ranging from 1-300 Hz). In terms of geophysical exploration, these frequencies can be used to explore great depths of up to 2 kilometers in accordance with skin depth (Hildes, 2014). Continuing to push the potential of tipper surveying, Kuzmin, in tandem with Arrawac Associates Inc., would take the concepts behind ZTEM and make a ground-based version known as the ELF-EM survey system (Figure 15).

Figure 16 – ELF-EM system on site in New Brunswick. The receiver coil is in front of the operator while the survey console is to their right. A 15-meter data cable would be attached between the two before surveying began. The system in the operators' hand is a DGPS solution not required for the ELF.

3.3 – ELF-EM Survey System

Purchased by Aurora Geosciences Ltd. in 2012, the ELF-EM system measures spatial attitude and ellipticity of the local time-varying magnetic field. This measurement reflects horizontal changes in subsurface conductivity (Braden, 2012). Three orthogonal coils within the ELF receiver measure the magnetic field components at each station. These air coils are packaged together with preamplifiers, a digital compass, and GPS antenna in a plastic pod weighing roughly 11 kilograms, light enough to be carried by one operator. The console unit, where preliminary processing occurs, is tethered to the pod by a 15-meter data cable and operated by the second crew member. This console hosts a PC-104 computer running Linux, a 24-bit analog to digital converter (ADC), a GPS receiver, and other peripheral devices all powered by an external 12V rechargeable battery. Using a similar method to ZTEM, the ELF-EM extracts four tipper components (rE, rN, iE, & iN) across 8 frequencies. These frequencies are: 11, 22, 45, 90, 180, 360, 720, 1440 Hz. Unlike ZTEM, these components are calculated in real time and displayed on the console as a vector plot using in-line and crossline components (Figure 16). As the time-series increases, data stacks improve the signal to noise ratio & produce a robust measurement. These changes are seen on the console, allowing the operator to determine when a reading has become stable (i.e., the vector components are not changing position on the vector plot). Tipper measurements are said to be rotationally invariant (i.e., do not change with respect to angle) (Jansen & Cristall, 2017). This simplifies surveying by allowing any orientation of the receiver so long as a common azimuth is used when deriving the components (Chave & Jones, 2005). The three coils used for measurement are self leveling (within reason) and situated so each calculated component (iE, rE, iN, & rN) are derived from more than one coil. Like any system operating within this frequency range, the ELF is susceptible to powerline noise. While 50 and 60Hz filters exist on the console, field tests in New Brunswick showed that ELF surveys should in general, stay 2km away from the nearest powerline. The onboard GPS lacks the accuracy of modern solutions but is easily substituted with a handheld option. These coordinates can be transposed to the output dataset during processing. In terms of survey operation, the ELF has several benefits over other ‘deep imaging’ geophysical methods. Cut lines or array set-ups are not need (small environmental footprint), only two operators are required (less expensive), and production ranges from 2-4 line-km a day. In the authors experience, 6-8 line-km per day were possible with ideal conditions and physically fit operators. Data is

exported via a RS-232c to USB adaptor as an XYZ file. A sample ELF file is included in Appendix A.

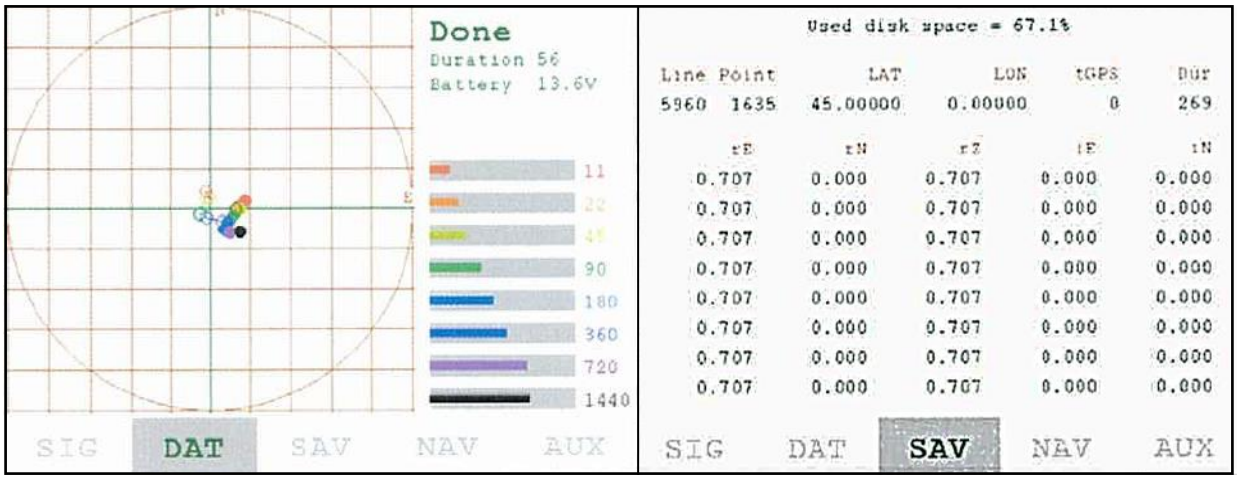

Figure 17 – (LEFT) ELF vector plot as seen while recording a measurement. The bars on the right indicate signal to noise ratio and are colour coordinated to match the vector plot. Solid points are vector plot real data points which the hollow points represent the imaginary component. (RIGHT) After a recording is taken, it is saved on this screen. The user can scroll through the ELF data file to make sure nothing is out of the ordinary. An example file as exported is shown in Appendix A.

3.4 – Processing ELF-EM Data

As mentioned above, preliminary data processing is done on the survey console (Figure 16). Tipper components for each frequency are recorded and organized using 'line' and 'station' values entered by the operator at the time of measurement. The GPS position (X, Y, Z), compass azimuth, signal to noise ratios for each frequency, and a measure of industrial noise removed by the 50/60Hz filter are included as well. Final processing can be done using any geo-software capable of handling XYZ files. Aurora Geosciences Ltd. (AGL) use Oasis Montaj to handle ELF data and have created multiple in-house scripts to speed up data processing. For this report, AGL standard processing procedures were used. Raw XYZ files (typically multiple, one for each survey day) are imported into a single Geosoft geodatabase. The first stage of quality control is to remove anomalous data points through two iterations. Initially all components are plotted as profiles to see how the trend varies across all frequencies (Figure 17). Components that show significant deviation from the trend are eliminated. Next, tipper vectors are plotted in a plan-view map by combining the in-line and crossline components. Anomalous tipper vectors are easily identifiable as their direction or magnitude will deviate significantly from the rest of the dataset (Figure 18).

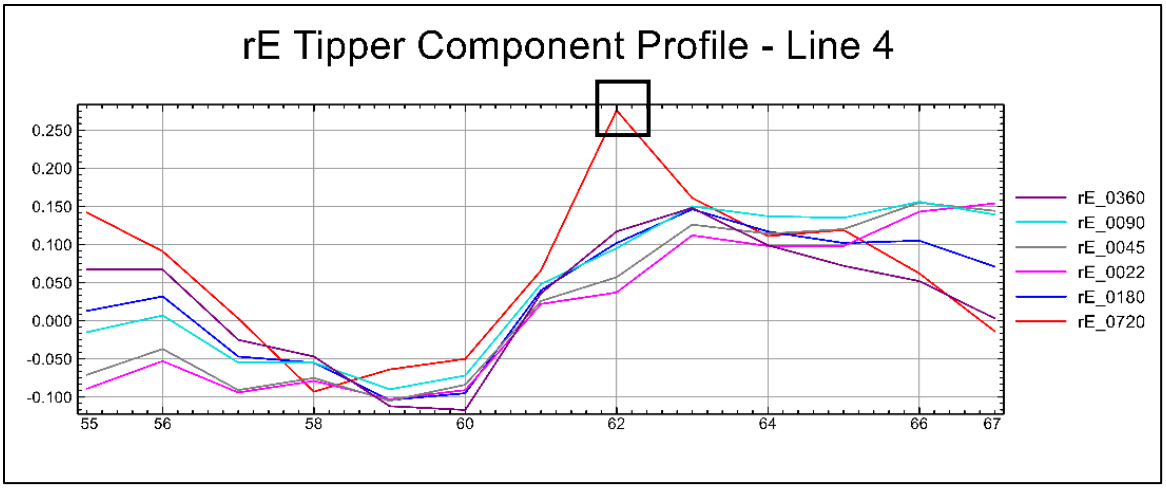

Figure 18 – Crossline component of the real ELF signal (rE) for Line 4 at Key Anacon. Anomalous datapoints can be eliminated at this time. A reading that would be removed is highlighted with a black box. This varies significantly from the rest of the dataset and should be eliminated to prevent anomalies propagating into later deliverables.

After repeats are averaged, and error channels are created for each component, the final database is ready for analysis. Following quality control, tipper components can be gridded and looked at individually. These grids show cross-over anomalies where conductivity changes in the subsurface. This can be difficult to interpret and requires looking at 4 separate components to 'see' the whole picture. A solution to this issue is presented by Pedersen (1998), who developed the 'Peaker' parameter for airborne tensor VLF. This equation used horizontal divergence of tipper components to aid in mapping morphologically long fracture zones by centering the anomaly over the fracture (akin to an RTP filter on a magnetic dataset).

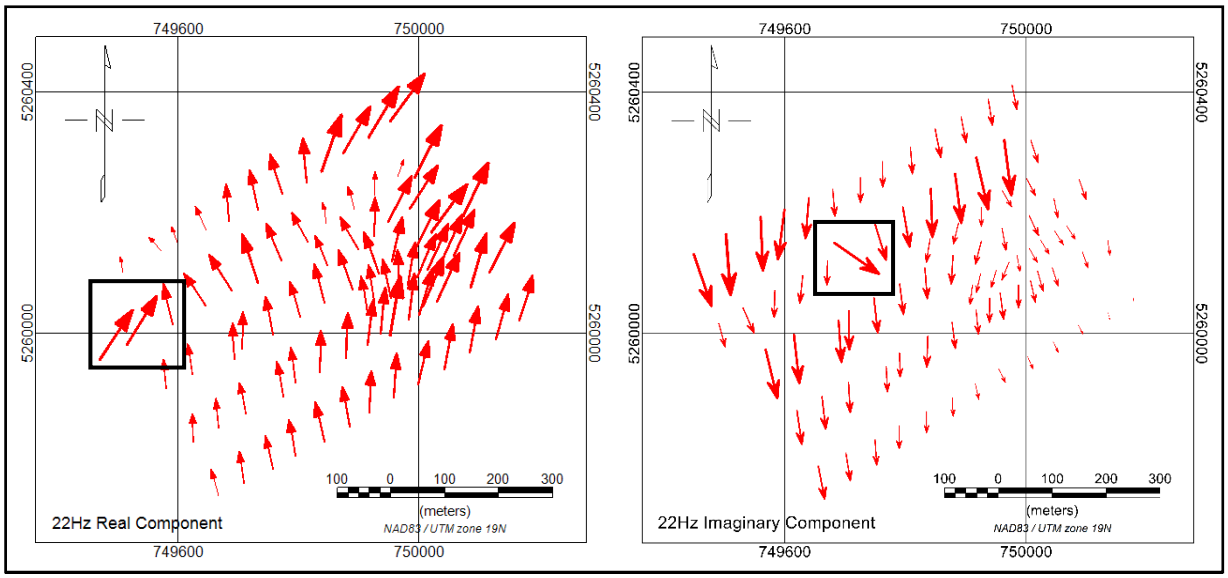

Figure 19 – Real and imaginary tipper components of a 22Hz signal recorded by the ELF at Key Anacon. Vectors that break from the trend significantly are removed. Examples in each dataset are highlighted in black boxes.

This parameter can be represented mathematically as:

$$Peaker = (\nabla \cdot T) = \left(\frac{\partial T_{zx}}{\partial x} + \frac{\partial T_{zy}}{\partial y}\right)$$

Where $\frac{\partial T_{zx}}{\partial x}$ is the x derivative of the in-line component & $\frac{\partial T_{zy}}{\partial y}$ is the y derivative of the crossline component. Legault (2010) used this parameter with ZTEM data over a copper/gold porphyry deposit and found it produced minima over conductive bodies. AGL uses this parameter to identify deep conductive structures but refers to it as Total Divergence (Figure 19). Being a derivative, the Peaker parameter produces sharper contacts but loses some of the long wavelength signal present in the tipper data (i.e., the top of a conductive body will be resolved better than the bottom). To preserve information at depth, tipper components can be summed after undergoing a 90-degree phase rotation, also known as a Hilbert Transform (Legault et al., 2012). This parameter produces peaks over conductive bodies (but lack the edge resolution of the Peaker). Since geophysical exploration is typically followed by drilling, resolving the top of a conductor with greater detail is more useful than the longwave information lost.

3.5 – The ELF Processing Problem

While the products above help visualize conductivity variations, there lies one significant issue; tippers are sensitive to conductivity contrasts(dimensionless ratios), not absolute conductivities. Contrasts are seen but cannot be related to a specific depth without some understanding of the subsurface conductivity. The solution to this problem is informed inverse modelling (inversion). Simply put, geophysical inversion is the process of using observations to determine a set of causal factors that could produce said observations. Inverting potential field data is not a new concept and has been achieved by various groups (de Groot-Hedlin & Constable, 1990; Smith & Booker, 1991; Rodi & Mackie, 2001). The most pertinent inversion algorithm to ELF processing was REBOCC (Reduced basis Occam's inversion) developed by Siripunvaraporn & Egbert in 2000. This algorithm was based on previous work by de Groot-Hedlin & Constable (1990) known as Occam's Inversion. The REBOCC algorithm significantly reduced the memory and CPU power required for processing tipper data compared to Occam's. It was originally designed for 2D inversions of MT data, but further advancements made it available in 3D where it was renamed WSINV3DMT (Siripunvaraporn et al., 2005; Siripunvaraporn & Egbert, 2009). Unfortunately, technology is improving rapidly, making it hard for developers of such niche software to keep up.

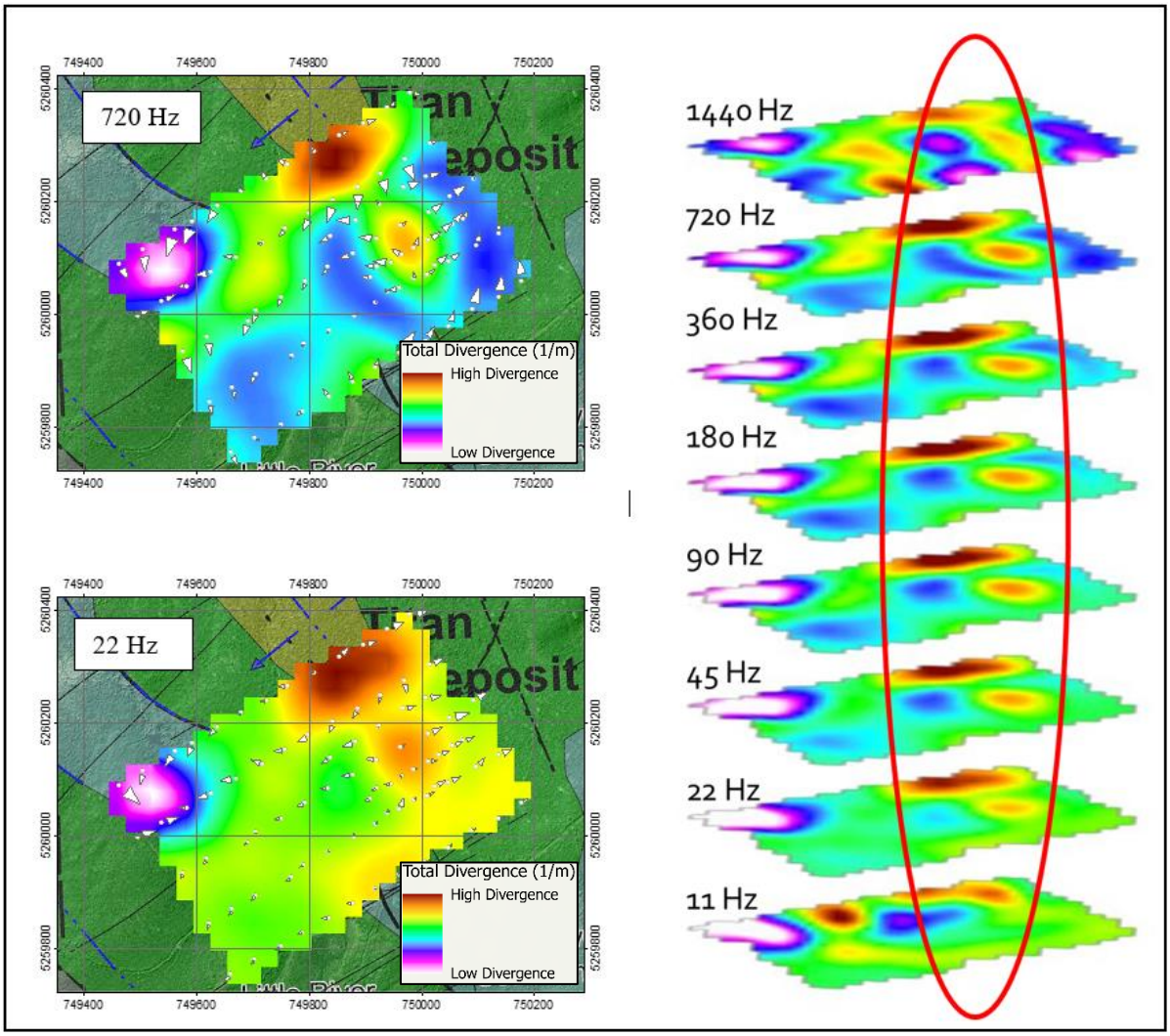

Figure 20 – (TOP LEFT) 720Hz total divergence grid for Key Anacon. 720 Hz vectors are shown on top with the background map taken from Osisko Base Metals (2019). (BOTTOM LEFT) 22Hz total divergence at Key Anacon. 22Hz vectors are shown on top with the same map for the background. (RIGHT) All total divergence grids displayed in 3D space. Red oval highlights a strong conductivity contrast across all frequencies. The depth extent of this anomaly is dependant on the subsurface conductivity. Projected coordinates are NAD83 UTM Zone 19N.

The REBOCC source code was written in Fortran 77 and compiled using gfortran (g77) on Cygwin, a Unix-like shell that runs on Microsoft Windows computers. This language is no longer supported by the platform and as such, has left this inversion code in a peculiar situation. For Aurora Geosciences to run the existing inversion code, it must be done on a legacy distribution of Linux that is still compatible with WSINV3DMT and g77. Inversion solutions that can run on a modern Windows computer exist, like ModEM3D (Kelbert, Egbert, & Tandon, 2014) and GIFtools (Kowalczyk & van Kooten, 2012), but these have expensive subscriptions, making them not easily accessible to researchers or smaller exploration companies.

3.6 – The SimPEG Solution

Recently, there has been a rise in open-source solutions capable of working with tipper data (Cockett et al., 2015; Heagy et al., 2017; Krieger & Peacock, 2014). Open-source software is an invaluable asset for geoscientists as it frees up resources (time / money) to be used elsewhere in a project. These open-source solutions all run in Python 3.0 (Van Rossum & Drake Jr., 2014), a modern programming language that runs natively on x64 Windows computers. One of these solutions, SimPEG (Simulation and Parameter Estimation in Geophysics), was developed in 2015 (Cockett et al.). This package provides a collection of geophysical simulation and inversion tools built within one framework. It can work gravity, magnetics, DC resistivity, IP, and EM data in 1- to 3-dimension of space. Recently, tipper data was made useable through the electromagnetics package developed by Heagy et al. (2017). This was a key breakthrough for ELF processing and opened the door for SimPEG to replace WSINV3DMT for 3D tipper inversions. The tools required to invert tipper data are provided by SimPEG, but the user must still create their own workflow to apply these tools (Figure 20). A python script for 3D tipper inversions in SimPEG was created for this thesis and used at the Key Anacon VMS deposit in New Brunswick. The script used to invert and model ELF data is presented in Appendix B.

3.6.1 – Santa's Workshop

The parameters of interest are briefly described below but readers are directed to Cockett et al. (2015) for full definitions. SimPEG allows the user to apply several regularization routines but for simplicity, the SW code only uses sparse regularization. To ensure the inversion algorithm recovers a plausible model (i.e., fits our observed data), it makes use of an L2 normalization to determine the data misfit. Since values will be squared, it is important to have clean data with as much obvious noise or outliers removed before inverting. The Santa's Workshop (SW) code requires SimPEG to be installed through an x64 python IDE. The SimPEG installation guide used Spyder IDE, so the same application was used here (Raybaut, 2009). SW requires two input files: tipper data and a DEM over the survey area. The former is created by exporting a quality-controlled ELF dataset while the later can be created in multiple ways. Typically, digital elevation models are available in raster format but for the purpose of this code, the user must use a 'raster to point data' function available in several geospatial software packages (Oasis Montaj, ArcGIS, & QGIS, etc.). On start-up, the input files are imported as SimPEG data arrays. From here, a GUI (graphical user interface) provides a set of parameters for the user to complete the inversion (Figure 21).

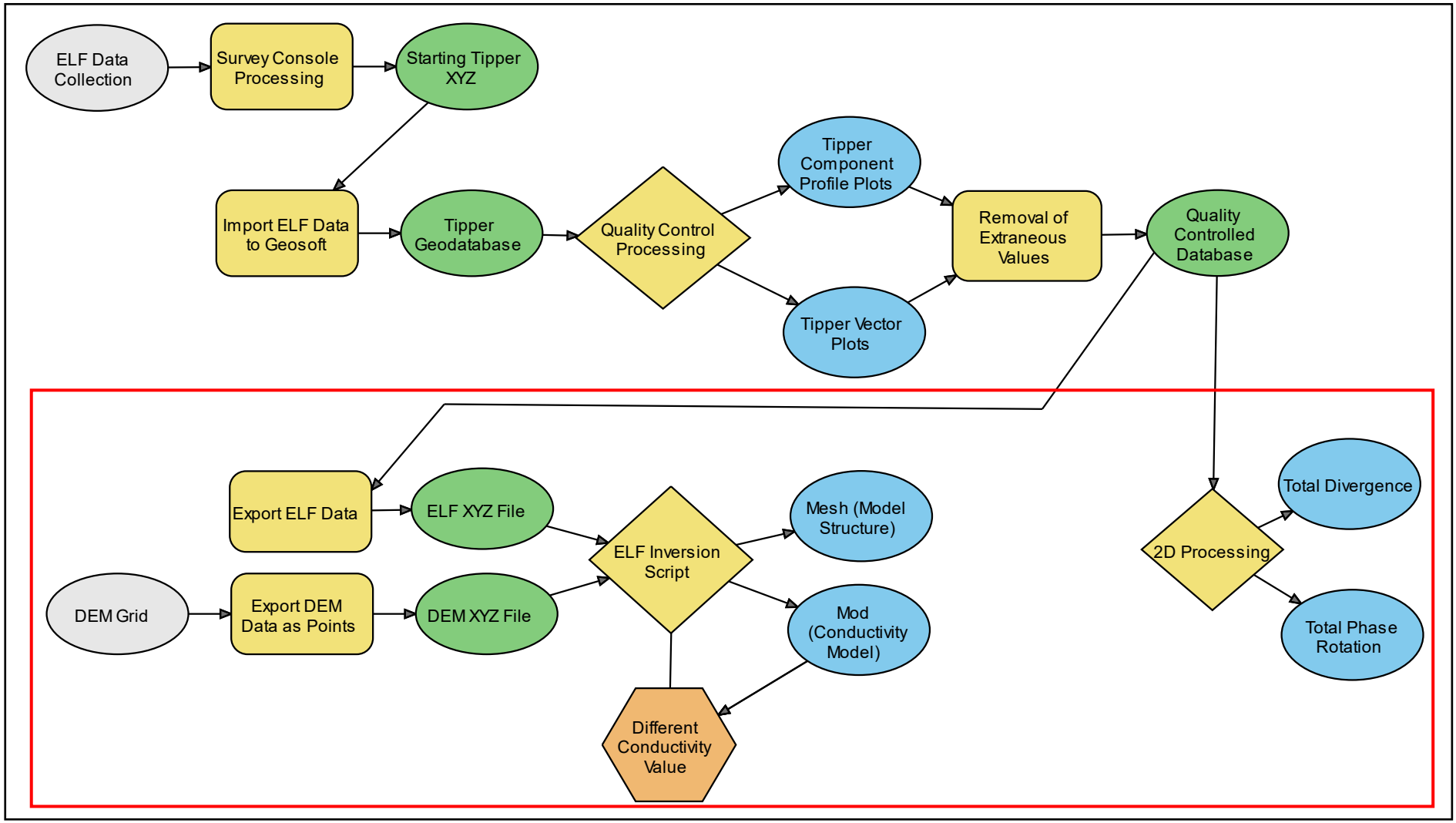

Figure 21 – Updated ELF inversion workflow from data collection to 3D conductivity model production. The section highlighted in red is the workflow for 3D conductivity modelling added in this thesis.

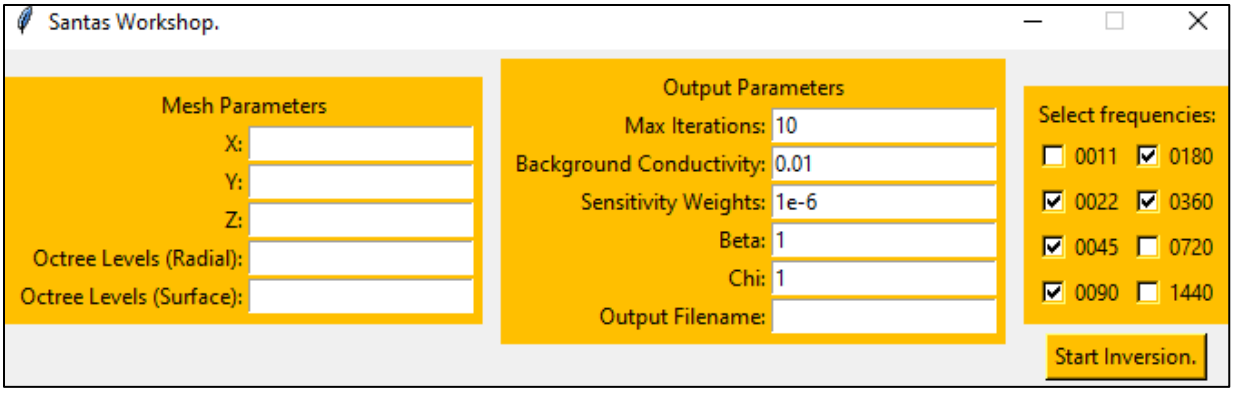

Figure 22 – Santa's Workshop GUI. The left pane has the user select their cell size as well as how quickly the cell size increases away from observed data points. The middle pane has the user set the number of iterations, background conductivity of the half-space, three parameters that impact how the algorithm matches the predicted data to the observed data, and a name for the file. The right pane allows the user select which frequencies they want to use for the inversion before hitting start.

Once parameters are set, a mesh is constructed using the user-specified cell size and an octree array. An octree mesh is a tree-like data structure that takes an initial cube and discretizes it into octants (Bern & Plassmann, 2000). In SimPEG, an octree mesh is first constructed from the smallest (base) cell size (Figure 22). From here, the octree levels (an array of values) specify how quickly cell widths grow away from a set of points. Each value in the octree array specifies how many cells occur at that level before increasing by a multiple of 2. The discretization process minimizes the number of cells required. This is crucial to minimize processing time when modelling low frequency sources as the inversion algorithm needs to add padding cells around the survey area to account for the physical size of the EM waves. Padding is set dynamically to two times skin depth by combining the lowest frequency and background conductivity with equation 2. The background value is important for proper padding and should be typical of the survey area. It is best practice to use prior information from geological maps, previous geophysical surveys, petrophysics, or borehole data, to select this value. Assigning an appropriate background conductivity puts the starting model closer to the true model, which is inherently better for the optimization algorithm. The degree to which a model is fit to the observed data is controlled mainly by the Chi-factor (user set parameter). A Chi-factor of 1 is standard but may be adjusted depending on data quality. If the dataset is clean, a Chi-factor < 1 may be used. Noisy or unreliable datasets may need the Chi-factor > 1 to produce a decent fit. The 'Beta' parameter in the Santa's Workshop GUI (Figure 21) is the cooling schedule of the trade-off value. This parameter sets the rate of reduction of beta each time the inversion problem is solved. If this rate is too low, significant changes between iterations will not happen and an appropriate fit will take much longer.

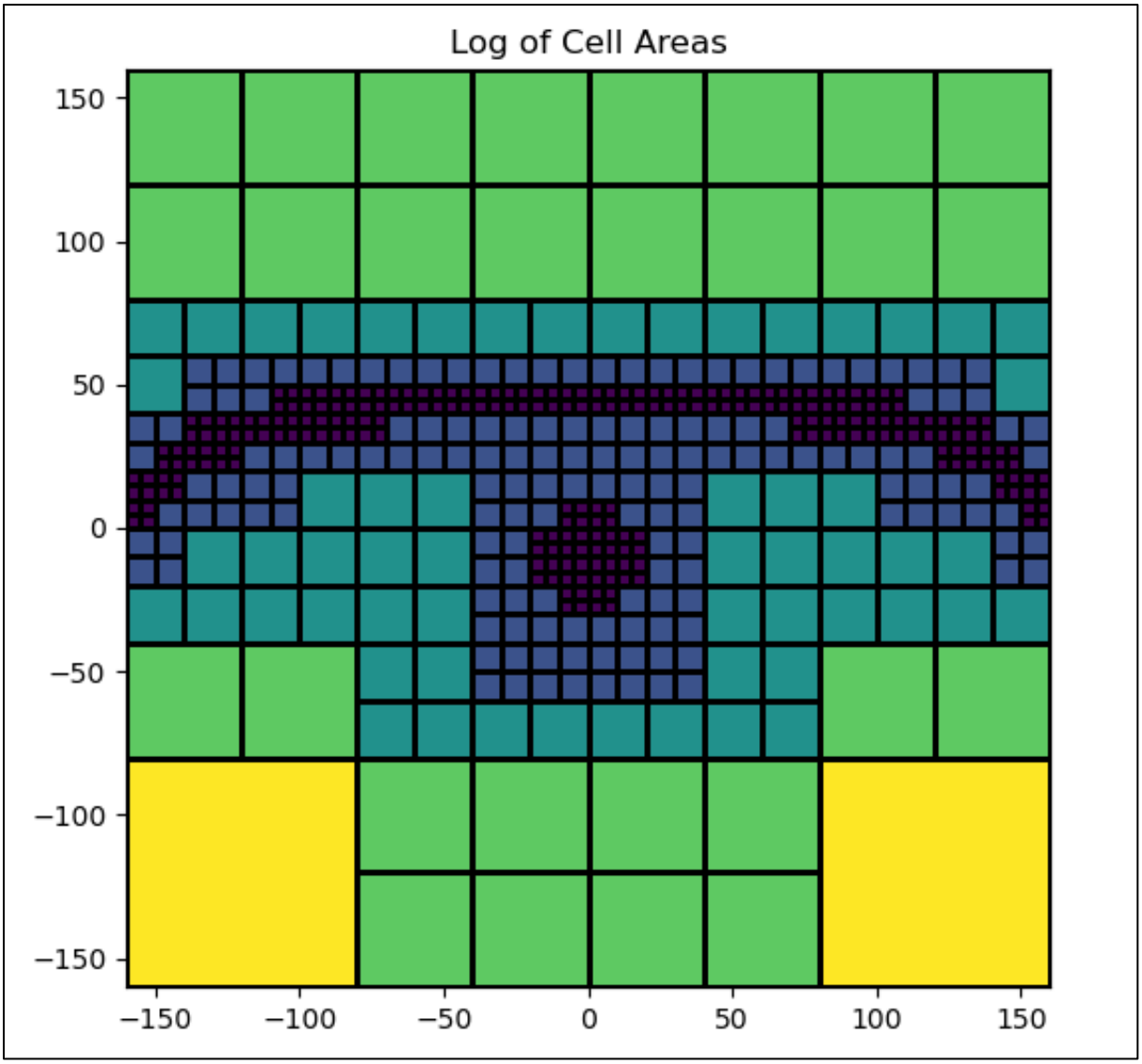

Figure 23 – Demonstration of an OcTree data structure. Figure shows a synthetic plan view map, with units in meters. Where observed data exists, the cell size is 5 m (core cell size). The cell size doubles along each axis as the distance increases from the observed data. They are 5 m (dark blue), 10 m (light blue), 20 m (teal), 40 m (green), 80 m (yellow). This collection of cells at 2x the core cell size is known as an OcTree level. The user sets how quickly cell sizes increase by using an array of integers in Santa's Workshop.

The last parameter that impacts the final model fit are the sensitivity weights. This value is used to ensure that each iteration does not preferentially change cells at one particular depth. Once a satisfactory model is given, the code exports a UBC-format 3D model (.msh / .mod) along with quality control plots for each frequency used in the inversion (Figure 23). These plots present the observed data, predicted data, and residual between the two for the final iteration produced by the SimPEG code.

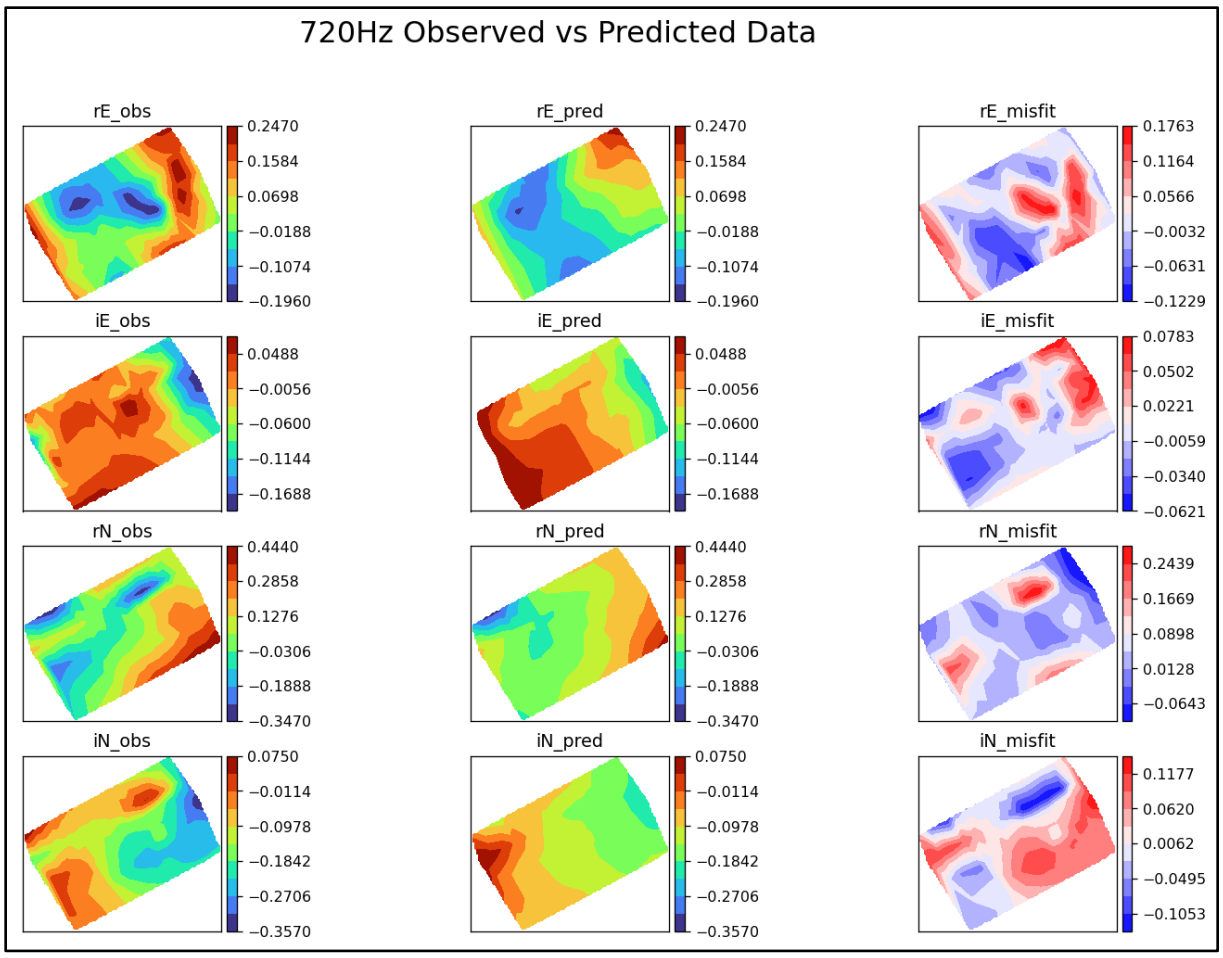

Figure 24 – Quality control plot produced by Santa's Workshop for the 720Hz frequency at Key Anacon. Areas where the model are underfit or overfit at this frequency become obvious. The user can either alter the parameters and rerun the inversion or keep the misfit in mind while interpreting the model.

3.7 – Test Inversion: Key Anacon Titan Deposit near Bathurst, NB

To test the effectiveness of Santa's Workshop, the code was used to create a conductivity model from a small survey collected at the Key Anacon Titan Deposit near Bathurst, New Brunswick in 2019 (Figure 24). Osisko Base Metals has a 43-101 report that was used for this thesis (Tetra Tech, 2018). Hosted in the Tetagouche Group as part of a bimodal volcaniclastic-sedimentary sequence, the Key Anacon Titan deposit is partially overlain by an eastern Carboniferous unconformity (Figure 25). Efforts have been made to describe the geology underneath the cover, but lack of outcrop, bedding, and reliable / well-recognized marker horizons have limited past work (Desautels, 2019). The deposit is characterized by steeply dipping and tight isoclinal folds. At least four phases of deformation have been recorded and correlated to events recorded elsewhere within the Bathurst Mining Camp (BMC). Key Anacon Titan is a VMS deposit hosting zinc, lead, copper, silver, and iron sulphides akin to other deposits located within the BMC (Brunswick 6 & 12 are

hosted within the same horizon). The deposit generally strikes between 325-335 degrees with a dip of 77 to the southwest. The sulphides are hosted within the fold nose and along 4 separate lenses, creating a pocket of mineralization near surface with multiple narrow limbs extending down dip (Figure 26). A copper stringer zone exists below the main deposit with a similar strike but shallower dip. These steep vertical conductivity contrasts are excellent to test an ELF survey.

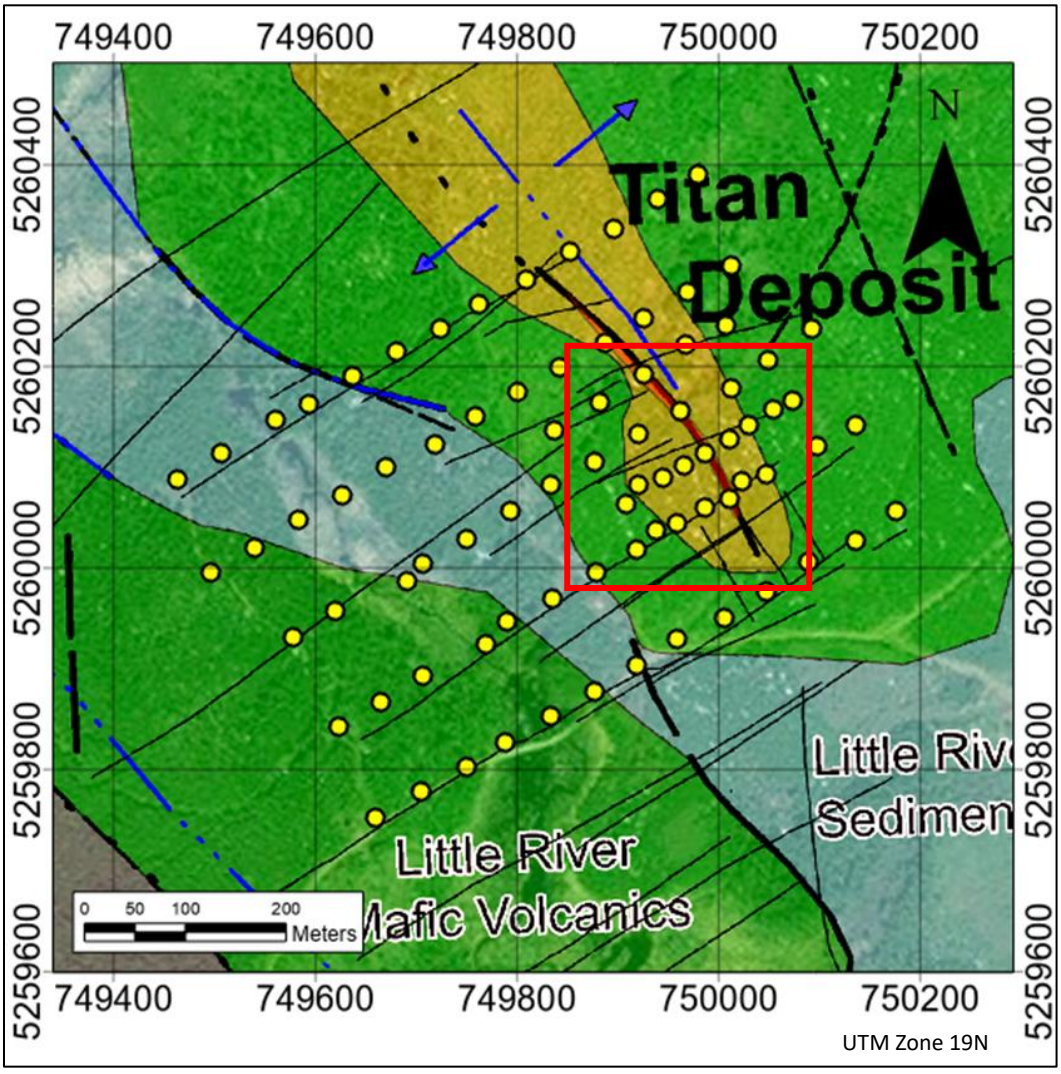

Figure 25 – Site location for Key Anacon ELF survey in 2019. Yellow points are station locations while the target deposit is outlined in red. The background map was provided by Osisko Base Metals. This map has removed the Carboniferous cover on the eastern side of the survey.

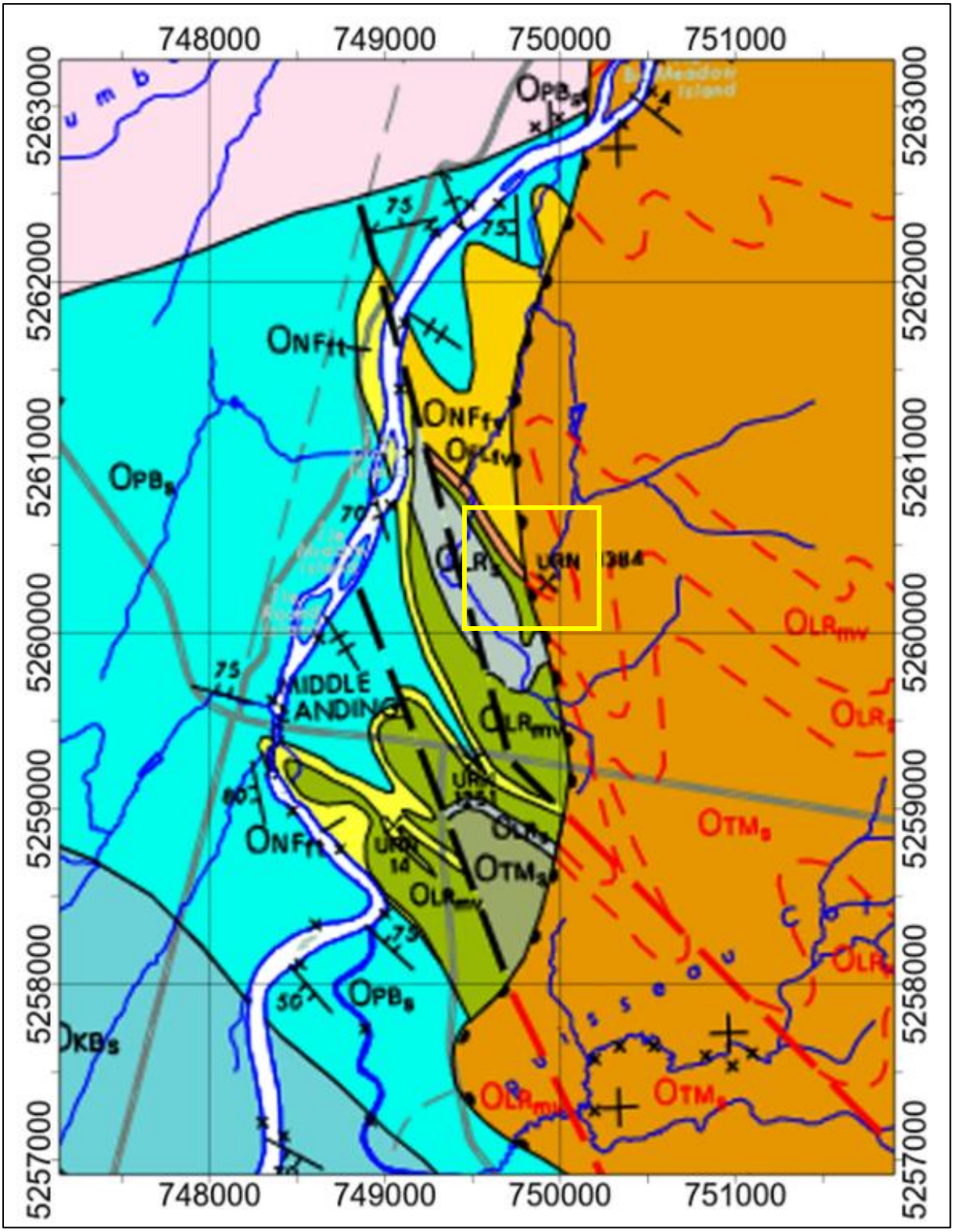

Figure 26 – 1:50,000 scale map of the Key Anacon area. Titan deposit outlined with yellow box. Structures under the carboniferous cover (red) were derived from diamond drilling and geophysical surveying. Map modified from Wilson et al. (2014) and reprojected using NAD 83 UTM Zone 19N..

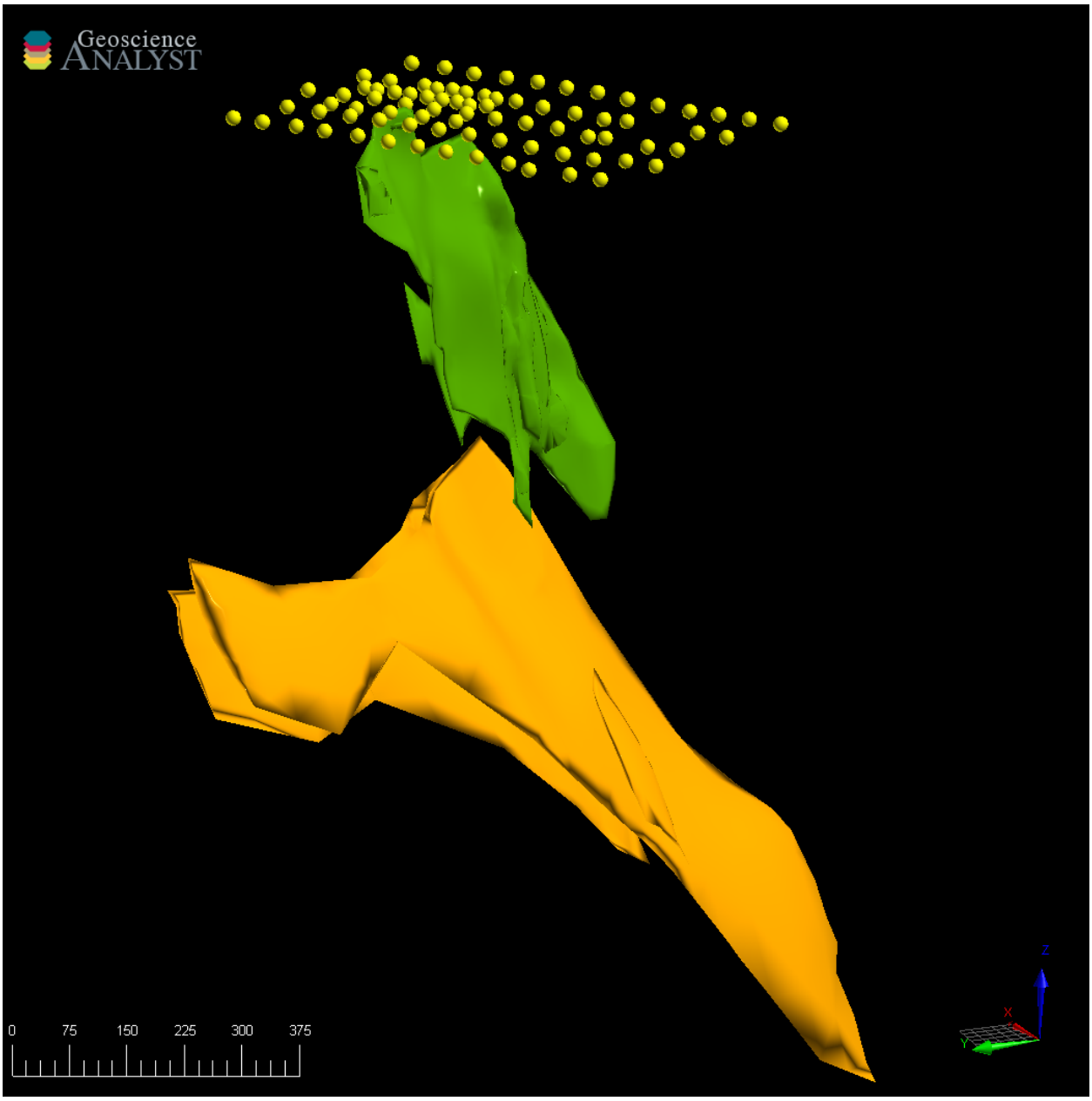

Figure 27 – Wireframe models of the Key Anacon Titan deposit (GREEN) and a potential copper stringer zone (ORANGE). This figure is looking southeast. Y-axis in bottom right corner is equivalent to North. (YELLOW) Survey points. 3D wireframes taken from Tetra Tech (2018).

82 ELF stations were collected over the deposit, covering an area of ~25ha. This data was collected by two surveyors, one holding the ELF receiver and console, the other collecting GPS data. Typically, the ELF collects GPS location data, but this module was broken at the time of recording. Two days of surveying at a moderate pace were required to collect the data. Once complete, the dataset underwent standard ELF processing as outlined in figure 20. After filtering and quality control, the tipper measurements were input into the ELF inversion code. X,Y, and Z core cell

sizes were set to 25 meters. This core cell area extends 700 below surface and was given a background conductivity value of 0.01 S/m. Background values of 0.1 & 0.001 S/m were used for additional models but most of the analysis uses the first model since it was most typical of the environment (background conductivity = 0.01 S/m). The remaining inversion parameters were left as the default. The resulting 3D model is shown below (Figure 27).

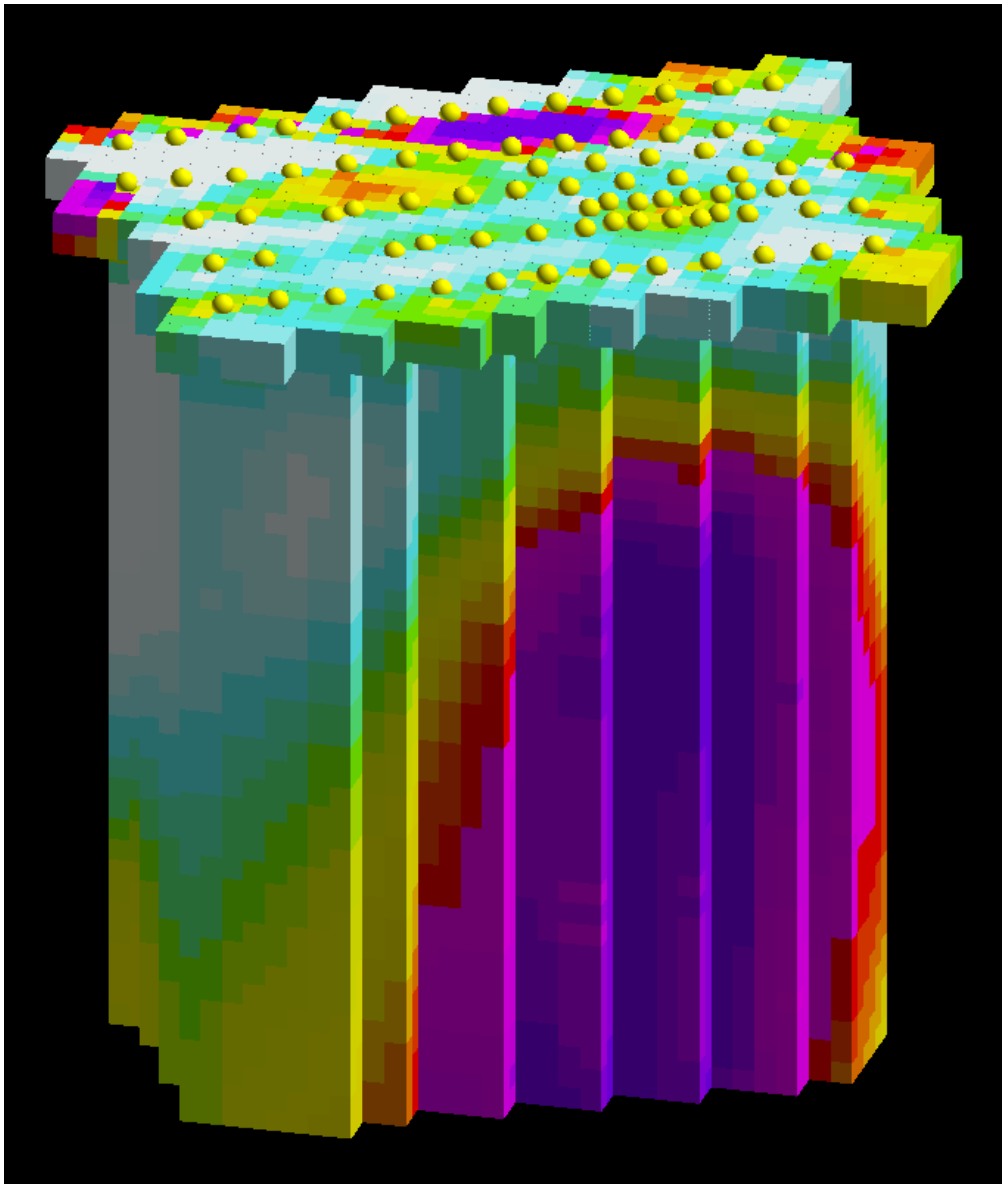

Figure 28 – 3D conductivity model derived from the 2019 ELF survey at Key Anacon Titan. Conductivity values range from 0.00078 S/m – 0.25246 S/m. Figure is looking north. Yellow spheres at surface are survey points.

While the absolute conductivity values assigned in this model could be contested by IP or other EM methods, we are interested in the *contrasts* between high and low conductivity values. Without supplementary conductivity data, this is all we can take from tipper data. When high values are

isolated, the conductive structure becomes clearer (Figure 28). There are two main conductivity highs in the ELF-derived model. One is small and near surface, while the other is a much larger, elongated feature that continues down to the bottom of the model. The anomalies strike approximately 330 degrees, in line with what was described in the 43-101 report. The elongated body shows a near vertical dip but this decreases with depth (Figure 29). As mentioned above, wireframe models of the mineral horizons exist. These models were constructed using a combination of borehole data and IP / MT geophysical surveys. While the individual horizons could not be identified, a zone of elevated conductivity encapsulates most of the wireframe sulphide lenses. The potential zone located underneath the known deposit has a shallower dip than the sulphide horizons above it.

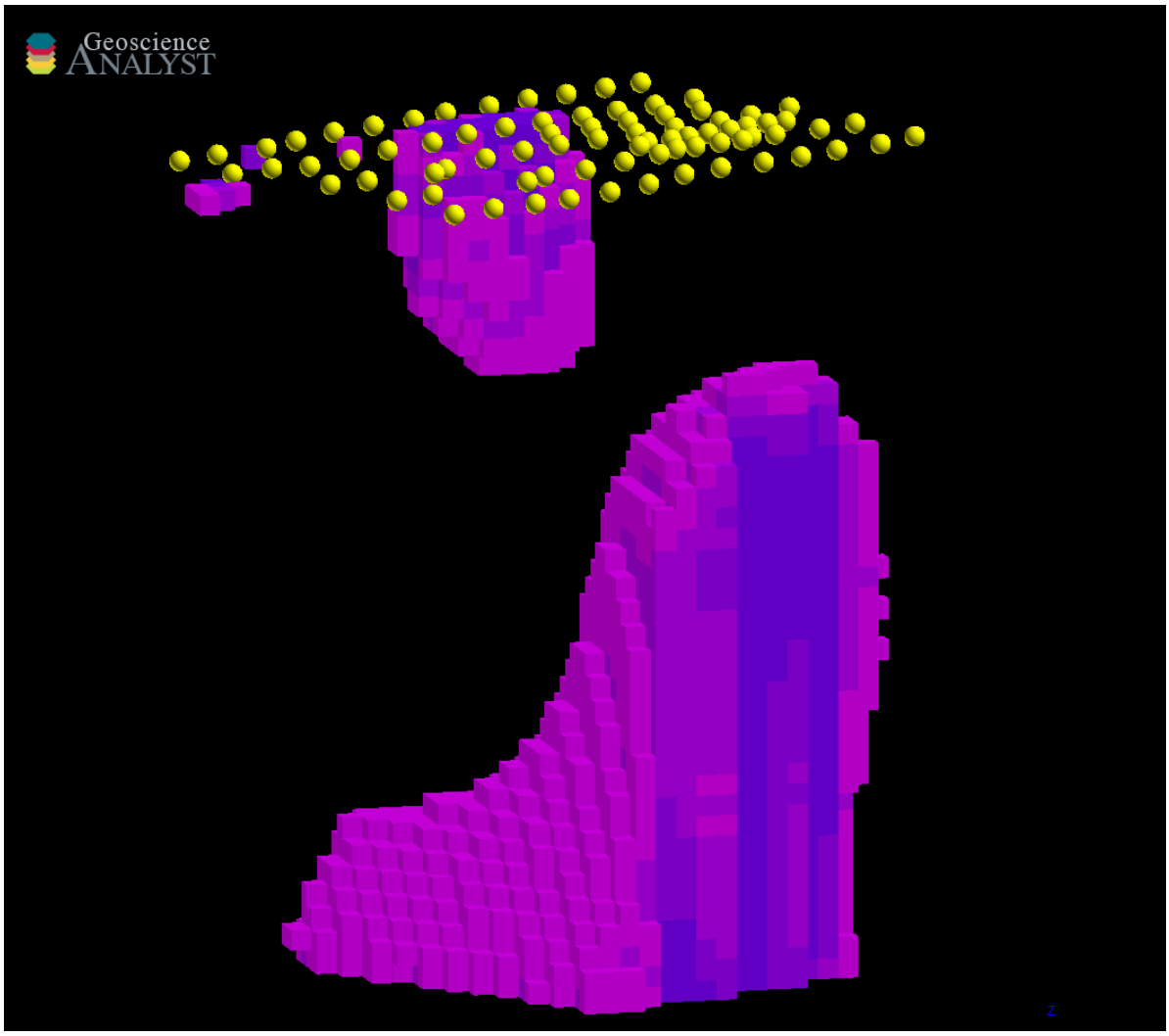

Figure 29 – 3D conductivity model only showing values > 0.1 S/m. Isolating high conductivity values shows two sources of conductivity contrasts. The deeper elongated anomaly expands along strike with depth. Figure is looking north-northeast. Yellow spheres at surface are survey points.

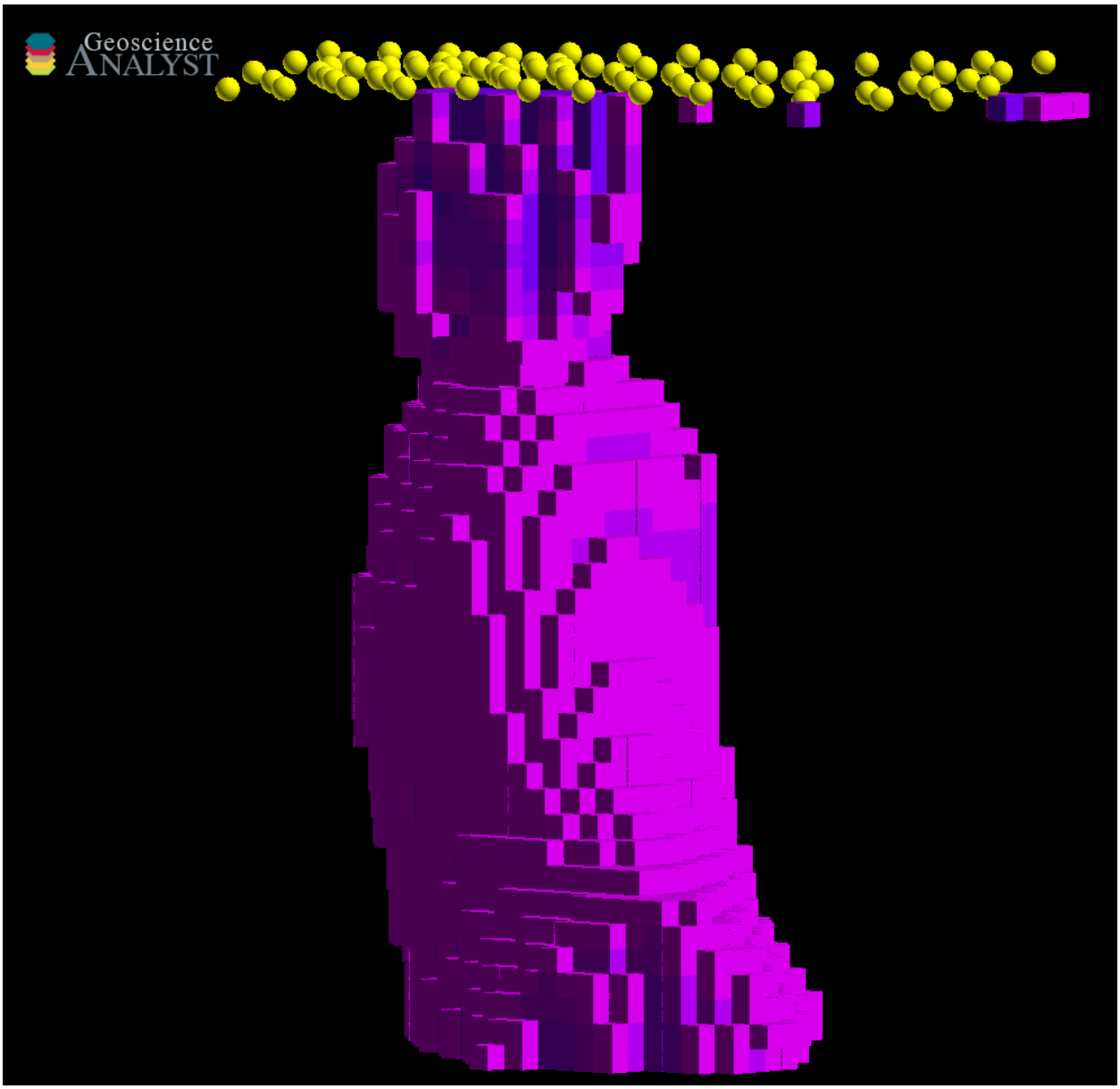

Figure 30 – 3D conductivity model only showing values > 0.1 S/m. Looking south-southeast at the model shows how the deeper conductive anomaly changes dip with depth. Yellow spheres at surface are survey points.

At Key Anacon, the SW code produced an acceptable model that fit with an independently derived wireframe model of the same deposit (Figure 30). Since tipper data isn't measuring true conductivity, changing the background value can produce vastly different models. Since conductivity varies so greatly in the subsurface, it is good practice to create multiple models across several orders of magnitude. While these results might be obviously too conductive or resistive, it can emphasize large features that are consistent between models. For this study 0.01 S/m was determined to be the most appropriate background value and as such, was used for interpretation. Using previous geophysical surveys or existing geological knowledge, an appropriate background

conductivity can be determined so tipper responses are modelled as accurately as possible. While not currently implemented in the SW code, SimPEG can incorporate a starting voxel model. This would be ideal for brownfield exploration as a starting conductivity model with structures would greatly improve the accuracy of the tipper-only model.

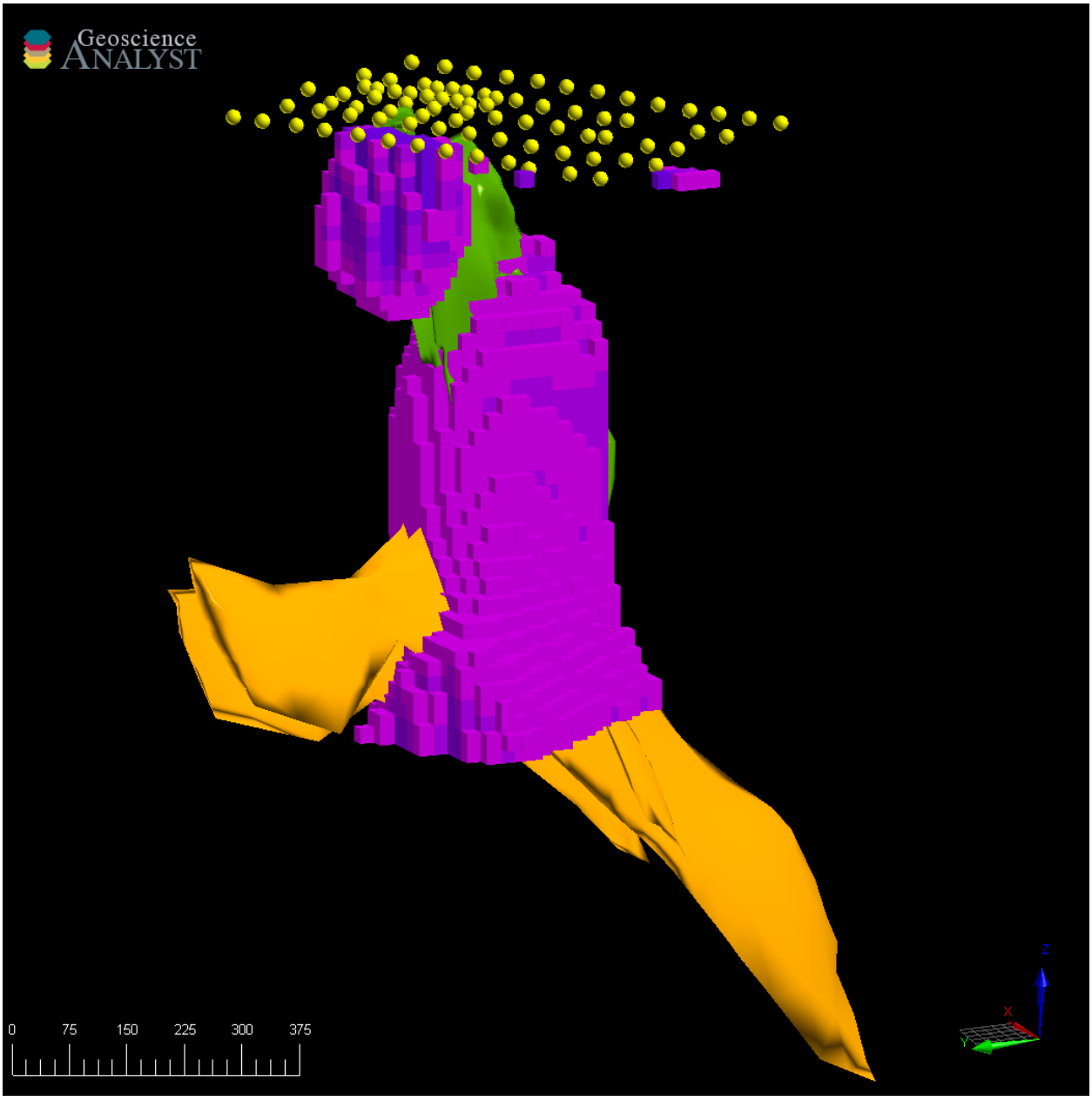

Figure 31 - 3D conductivity model only showing values > 0.1 S/m (PURPLE) overlain on top of the mineral horizon (GREEN) and potential stringer zone (ORANGE) wireframes. The change in dip between sulphide horizons and potential stringer zone are represented well in the conductivity model. Figure is looking southeast.

3.8 – Conclusions: The Open-Source Era

The combination of tipper data and SimPEG open-source inversions has forged a key steppingstone for ELF surveying. ELF-EM data was previously limited to 2D plan maps showing total divergence and an inversion workflow that was outdated and difficult to run on modern computers. Now, 3D conductivity models can be computed in a relatively short amount of time. SimPEG proves to be a modular and robust package that can be built upon to give the user more control over conductivity modelling than previously offered. While individual horizons were not detected, the zone of high conductivity determined by the ELF model encapsulated these horizons while showing the model is sensitive to dip changes as seen at depth in the potential zone. It is important to keep in mind the time required to create this model when analyzing it. A crew of two surveyors over the course of two days were able to collect all 82 ELF stations. 64-bit multithread processing has greatly sped up inversion times with the test dataset taking no more than 30 minutes to complete. The 'plug-and-play' nature of the SW code allows models to be created without modifying the script. That said, these models could be improved further with the addition of running a joint inversion or the use of a starting model from a previous survey. At Key Anacon specifically, a larger footprint over the deposit with greater station spacing would be ideal to improve the survey results. The larger footprint would fully encompass the wireframe models, allowing for a more direct comparison. While the data collection side is rather streamlined, these tipper models are based on ratios and rely heavily on the conductivities assigned by the user. A quick solution, if there are no previous models, is to run the inversion with multiple background conductivities to produce a range of potential models. These can be interpreted alongside borehole data and other geophysical surveys to see which model fits the other datasets best. In greenfield exploration, ELF conductivity models point to major conductive features that can be resurveyed using a higher resolution survey method. In brownfield exploration, any previous survey that identifies real conductivity values can be used to improve the ELF model fit. Even with its shortcomings, ELF-EM has positioned itself to be a cost-effective reconnaissance tool available to small and large exploration companies alike.

4.0 - Application of Santa's Workshop 3D modelling – Burwash Landing, YK

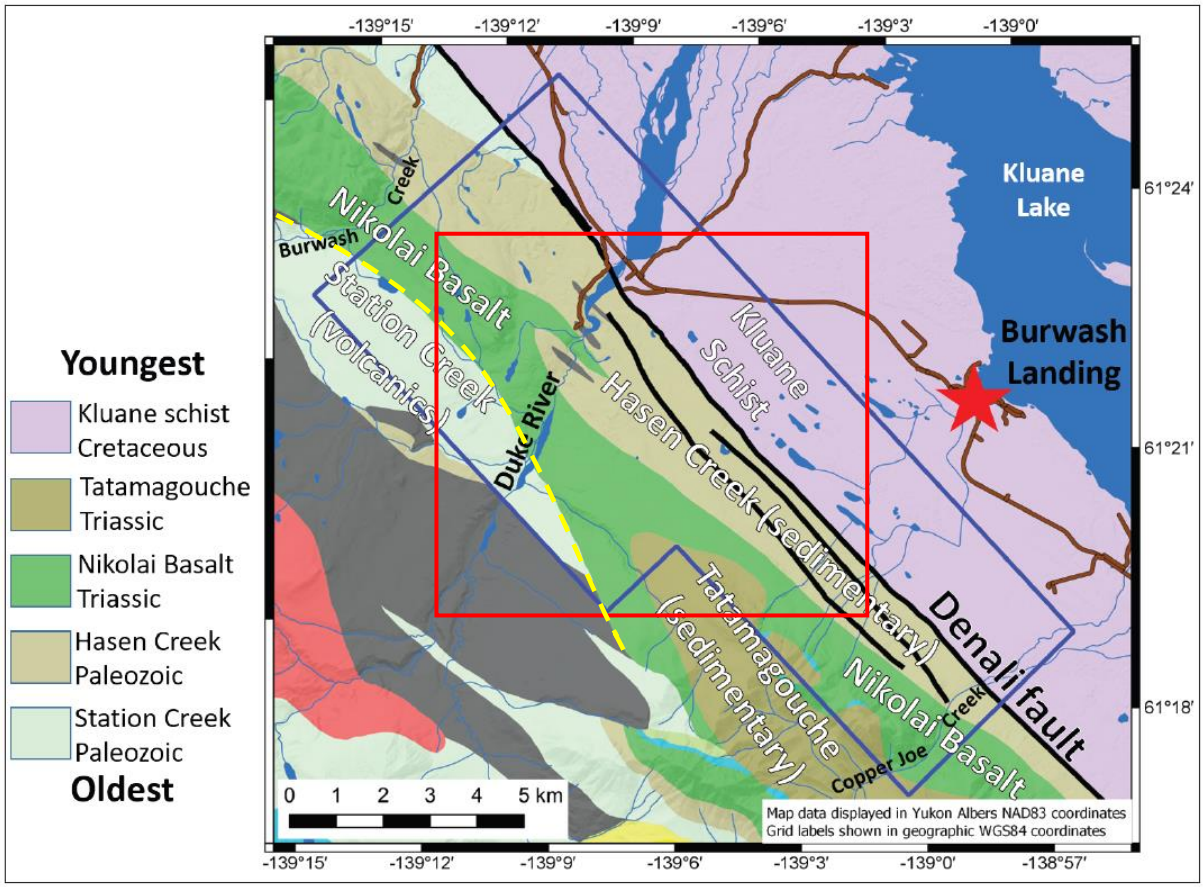

Figure 32 - Survey outline and geological setting of the 2020 geothermal exploration study. ELF survey footprint is outlined with a red box. Bock's Creek fault (DASHED YELLOW LINE) follows the contact between the Nikolai Basalt (GREEN) and Station Creek Volcanics (LIGHT GREY-GREEN). The Denali Fault and related splays are shown as thick black lines. UNITS NOT LISTED IN LEGEND: Kluane ultramafic complex outcrops multiple times in the survey area (DARK GREY), Wade Creek Pluton (RED), Chitistone Limestone (LIGHT BLUE) and Amphitheatre Conglomerates (YELLOW) are seen just south of the survey area but not within. Figure modified from Witter (2020).

4.1 – Introduction

In 2020, a study of Burwash Landing, Yukon was published to identify potential sources of geothermal energy (Witter, 2020). Drill targets were selected along regional structures that had potential to intersect regions of warm, near-surface conductive fluids. The ideal environment for geothermal fluid upwelling is a transtensional pull-apart structure, common along strike-slip faults (Faulds & Hinz, 2015). The Denali fault, an active crustal-scale feature with dextral strike-slip & some reverse motion, has Currie point depth data which suggests the average crustal geotherm is elevated in the survey area (Witter et al., 2018). Townend et al. (2017) studied the Alpine fault in New Zealand, an analogue environment to the Denali, and found extensive fracturing in the hanging wall. Meteoric water circulation through this region of the Alpine fault system raised

subsurface temperatures to ~84°C at a depth of 818m allowing for geothermal wells. As part of the Burwash Landing geothermal study, ELF data were collected to identify conductive structures potentially associated with areas of increased permeability. Here, warm geothermal fluids upwell close to the surface resulting from fault associated rock fracturing. At the time of publication, the only ELF inversion package available was the REBOCC code from 2000. A 2D model of subsurface resistivity was produced, but the quality of this model is highly debateable. One of the recommendations suggested in the Yukon Geological Survey (YGS) report was a full 3D resistivity (or conductivity) model that extended ~1 km deep. Using the new inversion code presented in chapter 4, the existing ELF data was re-inverted into a full 3D model, extending ~2 km into the subsurface. The goal of this chapter was two-fold: first, complete a full 3D inversion and compare the conductivity models with those provided in the YGS report; second, re-evaluate the drill targets considering the improved model.

4.2 – Geologic Setting

Israel et al. (2005) provided the most comprehensive study of the bedrock geology in the Burwash Landing area (Figure 31). Located along the edge of the Kluane Range, most of the survey area is underlain by the Wrangellia Terrane. Truncated by the northwest – southeast trending Denali Fault, the northeastern portion of the survey is characterized by Kluane Schist. At Burwash Landing, the Wrangellia Terrane consists of arc volcanic & sedimentary rocks of the Skolai Group (Late Paleozoic). Within this Group, the Station Creek Formation represents a volcanic arc that was overlain by marine sedimentary deposits of the Hansen Creek Formation during arc subsidence. The Station Creek Formation has extensive outcrop, but the base of the unit is nowhere exposed. It is dominated by volcanic breccia, tuff, basaltic lava flows, and epiclastic rocks. The Hansen Creek Formation sees a gradual thinning of the unit toward the southeast which has been described as a "transition zone" of decreasing volcanic deposition & increasing sediment input. This formation is majorly composed of marine clastics, carbonates, chert, and conglomerates while also including fossiliferous siltstone, turbidites, mudstones, and occasionally sandstone. The Skolai Group are unconformably overlain by sparse outcrops of the Nikolai & McCarthy Formations (Mesozoic). The Nikolai Formation is seen within the survey area and consists of subaerial basalt flows which outcrop throughout the region. The thickness of this unit is not well constrained but can reach up to ~1km thick. A second unconformably overlain assemblage known as the Tatamagouche Formation overlaps a portion of the Nikolai basalt to the southwest of the survey

site. According to Israel et al. (2005), it is undecided if this package is part of the Wrangellia Terrane or an overlap assemblage. The Tatamagouche Formation is strongly deformed and composed of argillite, sandstone, greywacke, conglomerate, and calcareous siltstone. Throughout the Wrangellia Terrane there are a series of intrusive bodies attributed to the Kluane mafic-ultramafic complex (Hulbert, 1997). These intrusives are composed mostly of peridotite and dunnite with minor amounts of pyroxenite and gabbro. The thickness of the intrusives are majorly unknown but multiple exposures are seen along the Duke River. On the northeastern side of the Denali Fault the Kluane Schist represents a highly deformed sedimentary package deposited during the Late Cretaceous. There is a lack of horizon markers, but slight lithological distinction can be made between the biotite rich-schist, muscovite rich-schist, and cordierite-bearing gneiss over hundreds of meters (Stanley, 2012). This unit is overlain by a thick sequence of Quaternary sediments which show a minimum thickness of ~390 m at the town of Burwash Landing (Witter, 2020).

Structurally, there are three main phases of deformation recognized: A pre-Middle Triassic compressional event, a mid-Cretaceous contractional event, and lastly, a post-Cretaceous strike-slip faulting event (Denali Fault). The initial compressional event is difficult to interpret due to overprinting of younger structures however, stratigraphic relationships indicate uplift of the Paleozoic units occurred before deposition of the Triassic units. Following this, mid-Cretaceous deformation can be characterized by upright to locally overturned, and tight to isoclinal folds that strike northwest to southeast. These fold structures are accompanied by southwest-verging thrust faults. The final deformation event occurred in the Late Mesozoic and resulted in regional-scale folds and the Denali fault system. This fault and its associated structures overprinted previous deformation with a dextral strike-slip motion. It is responsible for ~370km of right-lateral displacement sometime between the mid-Cretaceous and modern times (Lowey, 1998). The Denali fault separates the Wrangellia Terrane from the Kluane Schist and proves to be the main target for geothermal exploration in the 2020 YGS report. The modern tectonic regime along this portion of the Denali fault is transpressive with right-lateral deformation rates of ~2mm/year & sub 1mm/year vertical deformation. On the southwestern side of the Denali fault, clay-rich units of the Hasen Creek and Tatamagouche formations are not likely to have the capacity to maintain open fractures. Within the Wrangellia Terrane, the Bock's Creek fault is another major structure that cuts through the survey area. The fault motion is not well constrained, but it offsets Paleozoic and Mesozoic

stratigraphy, has multiple small-scale splays, and crosscuts older, steeply dipping faults. For geothermal exploration, the Kluane Schist, Nikolai Basalt, and volcanic rocks of the Station Creek formation are favourable environments as they have an ability to maintain open fracture space for meteoric waters to circulate. The Kluane Schist is most favourable as this rock type makes up the Denali fault hanging wall where extensive fracturing is possible due to the transpressive environment (as seen at the Alpine fault in NZ).

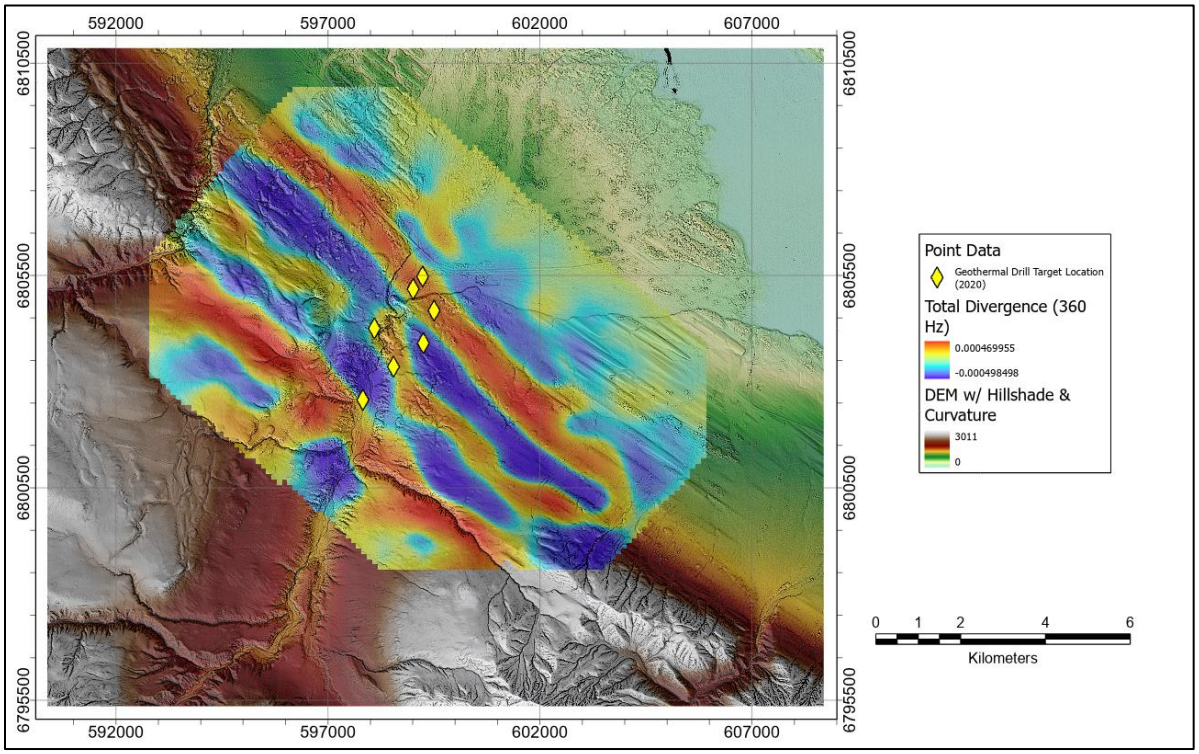

Figure 33 – Total divergence of 360Hz ELF tipper data. Tipper data is overlain by a hillshade and curvature data derived from ArcticDEM to show topographic variation. Geothermal drill locations selected by Witter (2020) are shown in yellow.

4.3 – ELF Data at Burwash Landing

Before constructing conductivity models, ELF data can be interpreted using traditional plan-view methods. Total divergence (as outlined in chapter 4) of the ELF data at Burwash Landing was initially interpreted to have multiple linear NW-SE trending structures visible across several frequencies (Figure 32). The two major linear anomalies were spatially associated with traces of the Bock's Creek and Denali fault. The third linear feature between the two main faults was identified as a right-step offset fault structure that was located similarly in both the magnetics and gravity datasets (Witter, 2020). This right-step linear anomaly dissipates with increasing depth (decreasing frequency) in the total divergence grids indicating it is most likely a shallow feature (Figure 33). The Bock's Creek fault shows a broad anomaly that stays consistent through all the

frequencies. This could be attributed to the fracture prone Nikolai basalts that underlie most of the fault. This unit would have undergone brittle deformation during the D2 event creating a fractured unit along the fault where waters could more easily circulate (Witter, 2020). While total divergence can indicate conductivity contrasts, the 3D structure of these conductive bodies is largely unknown. Considering the purpose of the YGS project, understanding this 3D structure is imperative to determining the best locations for a borehole and the angle in which to drill. To model these potential structures, a REBOCC inversion was used to create a conductivity model that fit the tipper data within a certain misfit. Due to the processing issues mentioned earlier, only a 2D inversion was possible at the time.

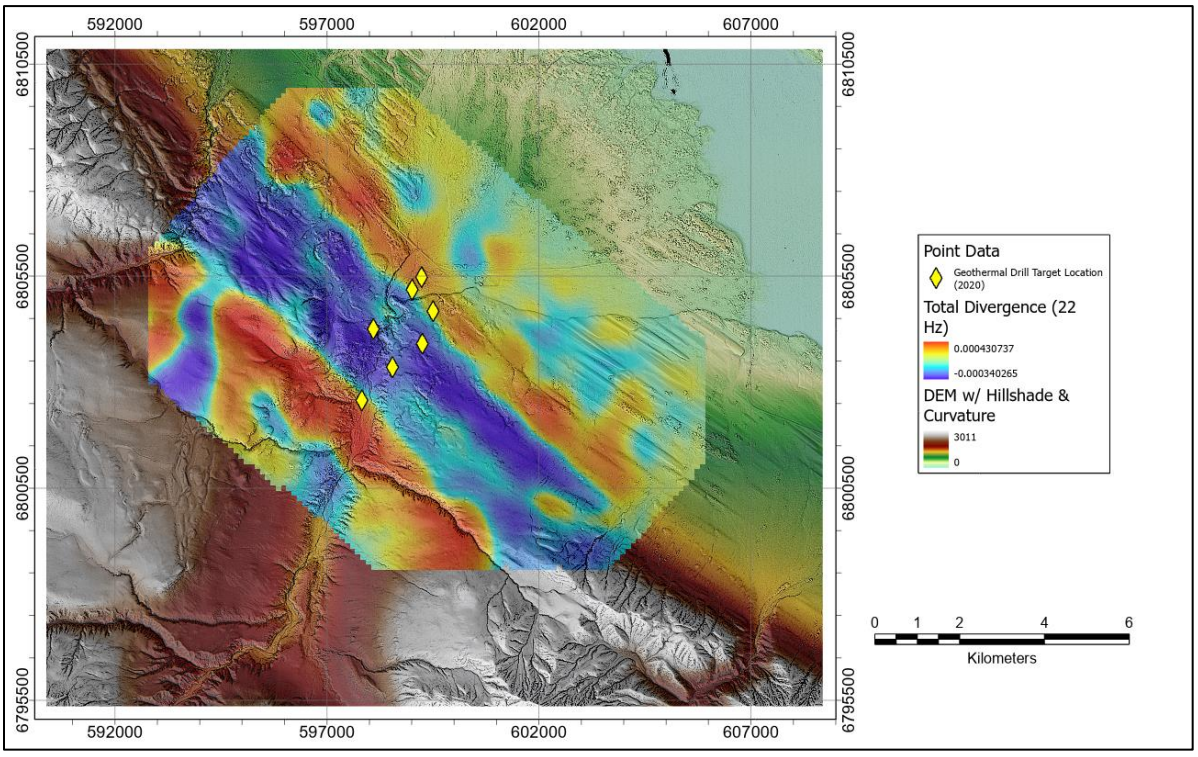

Figure 34 - Total divergence of 22Hz ELF tipper data. Tipper data is overlain by a hillshade and curvature data derived from ArcticDEM to show topographic variation. Geothermal drill locations selected by Witter (2020) are shown in yellow. Conductive anomaly between major NW-SE trending structures has disappeared in the lower frequencies.

4.4 – 2D Conductivity Models

The original ELF data was collected by AGL in 2019. Lines were spaced 1km apart while stations were spaced at 250m. This data was processed followed the same routine outlined in chapter 3. After quality control, twelve 2D resistivity profiles were constructed using the REBOCC inversion, three of which are shown below (Figures 34). Each profile had a horizontal cell size of 125m & a variable vertical cell size ranging from 20m to 2000m. Topography was not considered

during the inversion process and was added after the models were complete. Multiple reference models were tested but the most stable for inversion proved to be a uniform half space with a background value of 10Ωm or 0.1 S/m. In the YGS report, the only unit clearly identified were the Quaternary sediments located on the eastern side of the cross sections, in the shallow subsurface. A 2-3km area surrounding the Denali fault trace shows high conductivity values. This zone has been attributed to three potential sources: 1) zone of fractured rock infiltrated by conductive fluids, 2) fractured & altered bedrock containing clays or other conductive minerals, or 3) graphite-bearing bedrock.

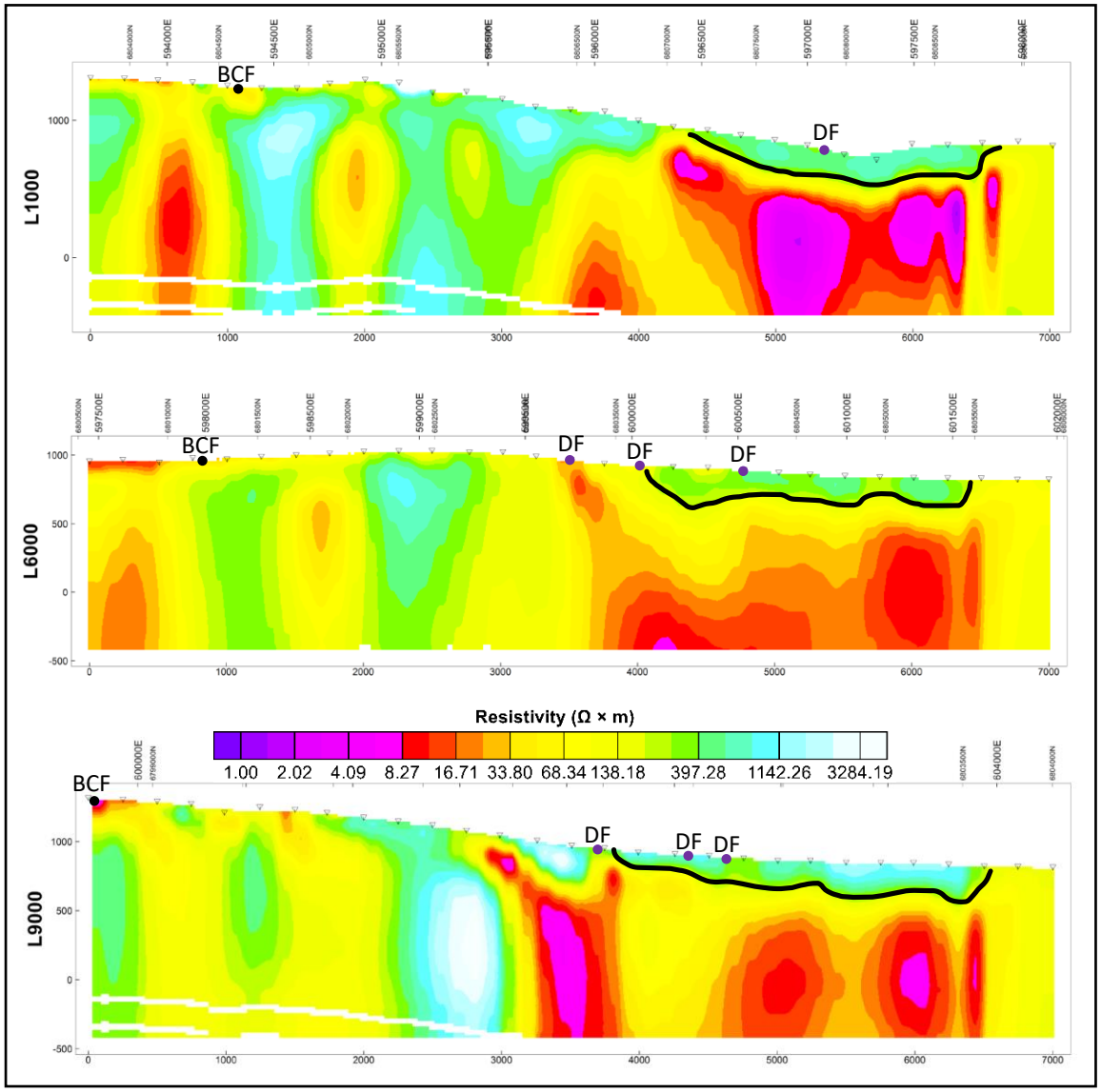

Figure 35 – 2D resistivity sections of Burwash Landing. BCF – Bock's Creek Fault, DF – Denali Fault, and Black line – location of Quaternary sediments. Colour bar and cross-sections are displayed using a log/linear scale. The range of values were determined from the entire 2D dataset so one colour bar applies to all 3 sections. Geographic location of cross sections are labelled on Figure 33. Sections modified from Witter (2020).

Bedrock to the west of the Denali fault has been identified as Hasen Creek formation while the Kluane Schist (both muscovite- and biotite-rich subtypes) makes up the eastern side. The Witter report (2020) found little evidence of a sharp conductive change across the boundary of the Denali fault separating the two units. Zones of high conductivity are discontinuous with some anomalies forming narrow, vertical features (Figure 34). These features were cautiously attributed to crust dismemberment by faulting, vertically oriented geologic structures, but more likely, artefacts of the inversion process. The southwestern portion of the survey area is characterized by moderately conductive values. These values have been attributed to the Station Creek formation where geometry suggests a variety of dip angles for the Bock Creek fault. The central portion of the survey area was found to have a poor correlation with either of the units mapped by Israel et al. (2005). Witter (2020) concluded that interpretation of the 2D resistivity sections was challenging, stemming from the uncertain spatial relationship between the subsurface conductivity and the inferred fault structure. Tipper data is sensitive to 3D conductivity variations so limiting an inversion to 2D will inherently skew the interpretation. Since the survey area is characterized by two major linear structures that cross the entire survey, creating a full 3D model helps model cross-line anomalies not seen in a 2D inversion.

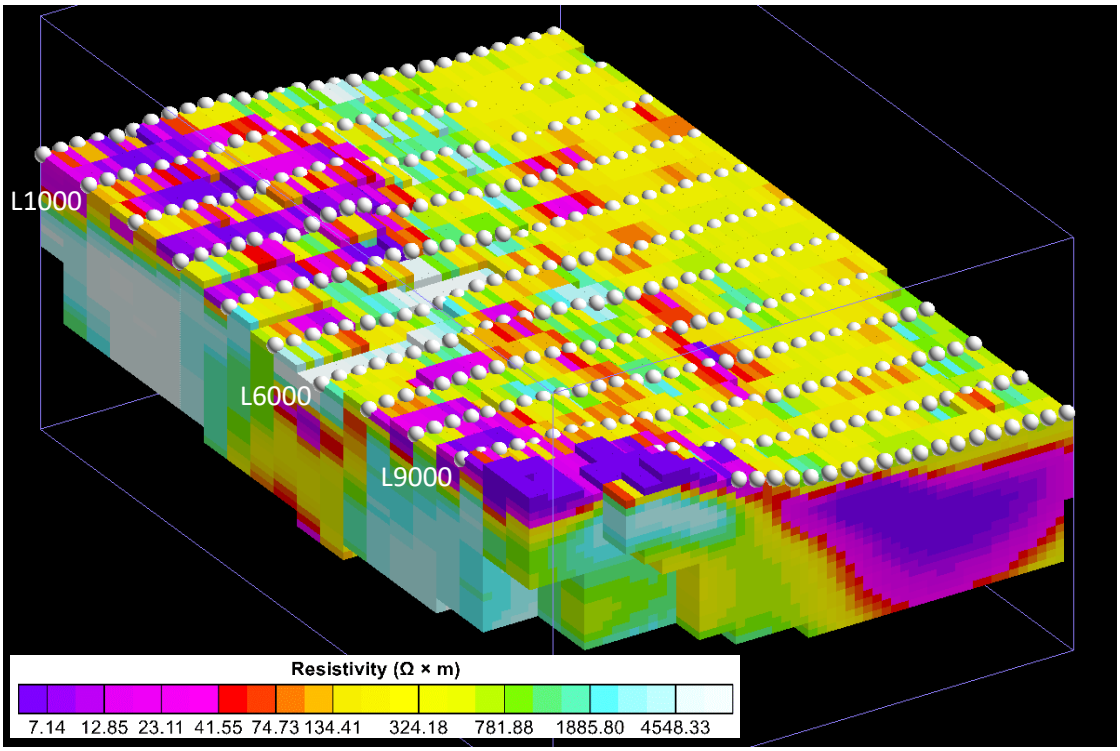

Figure 36 – 3D conductivity model derived from Santa's Workshop with a background value of 0.01 S/m. Station locations are displayed with a white sphere. Figure looking north. NOTE: For simplicity, colour table shows resistivity.

4.5 – 3D Conductivity Model

Using the inversion script outlined in chapter 3, a full 3D conductivity model was created for the YGS geothermal survey (Figure 35). Due to computational limitations, a 'coarse' cell size of 500m (X-axis) by 125m (Y-axis) by 100m (Z-axis) was used. Unlike the 2D sections, topography can be handled within the code and was used to refine the model before the inversions began. Considering the nature of tipper data (which highlights conductive contrast, not absolute conductivity), background conductivities of 0.001, 0.01, and 0.1 S/m were used to create multiple models. While the depth extent of an anomaly change depending on background conductivity, the XY locations of these contrasts tend to stay the same. Highly conductive background values result in shallower anomalies while the opposite tends to elongate the anomalies. The 3D model was directly compared to the 2D sections by looking at slices of the model along the same axis as those given with the YGS report (Figure 36).

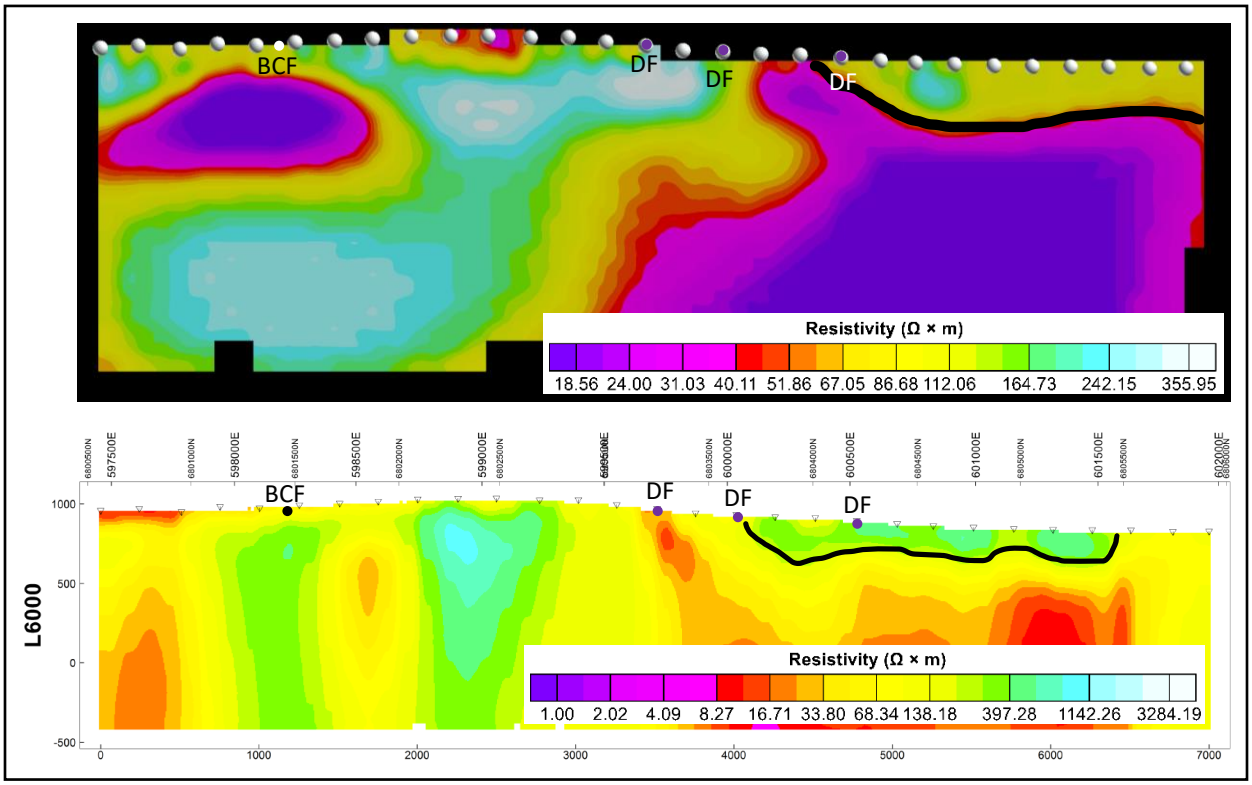

Figure 37 – L6000 comparison between 3D and 2D inversions. Surface location of major structural features are labelled the same as Figure 32. Suspected Quaternary sediments are highlighted with a black line. NOTE: The 3D model extends 2 km into the subsurface while the 2D sections, only 1400 meters.

Unlike the 2D inversion, conductive anomalies are more continuous along-line. Some similarities can be seen between the two datasets, but most of the 3D results paint a different picture than the 2D counterpart. The discontinuous anomalies in the 2D inversion are narrow horizontally but

extend quite deep. Comparing line 6000, the 2D results show several vertical anomalies which were interpreted as potential faults. A 'finger' of high conductivity can be seen near the center of the section, dipping to the northeast. The same line derived from the 3D model shows two major conductive anomalies; 1) a shallow but strong conductive contrast under the Bock Creek fault trace and 2) a strong conductive contrast under the Denali fault trace that continues to the bottom of the model but dipping to the southwest. These 'smoother' anomalies, especially along the Denali fault, create a continuous, easy to interpret structure compared to the 2D counterpart (Figure 37).

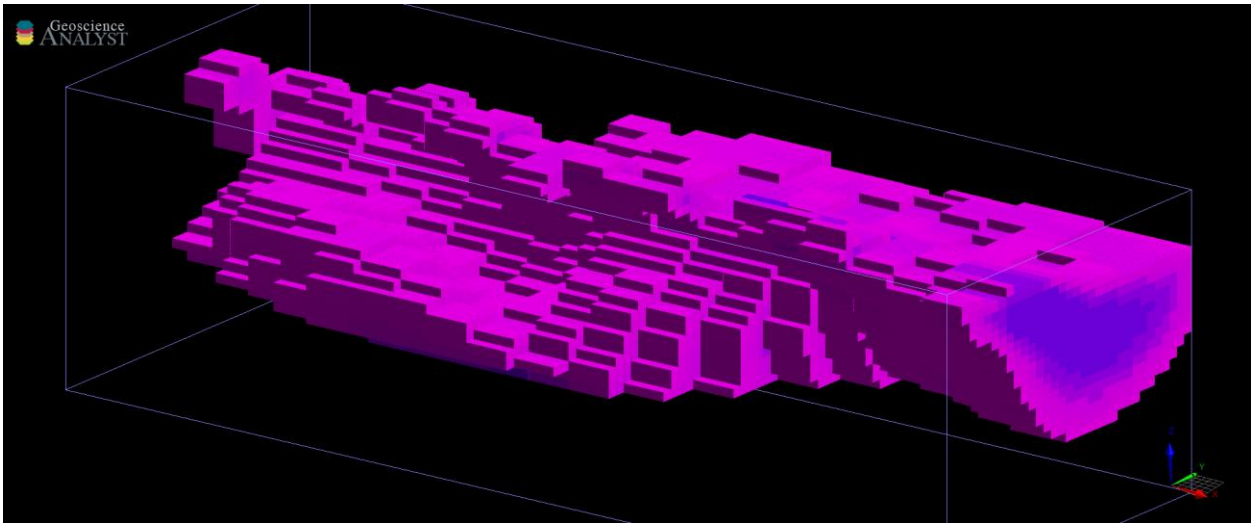

Figure 38 – High conductivity values (>0.05 S/m) related to the Denali fault trace. This conductive anomaly is continuous and easier to interpret as one large structure rather than multiple small structures as identified in the 2D interpretation.

While these can be compared as sections, the main advantage of the new model is its three-dimensional nature. When looking in 3D, there is a sharp conductivity contrast at the Denali, and less so, the Bock's Creek fault. Unlike the discontinuous 2D sections, these anomalies can be traced along the entire dataset and match digital traces of the faults (Figure 38). Instead of putting the user in a position where they need to relate discontinuous anomalies across widely spaced profiles (1 km), the SimPEG derived model shows a continuous across-line zone of high conductivity, taking away some of the guess work needed to extrapolate 2D sections into 3D.

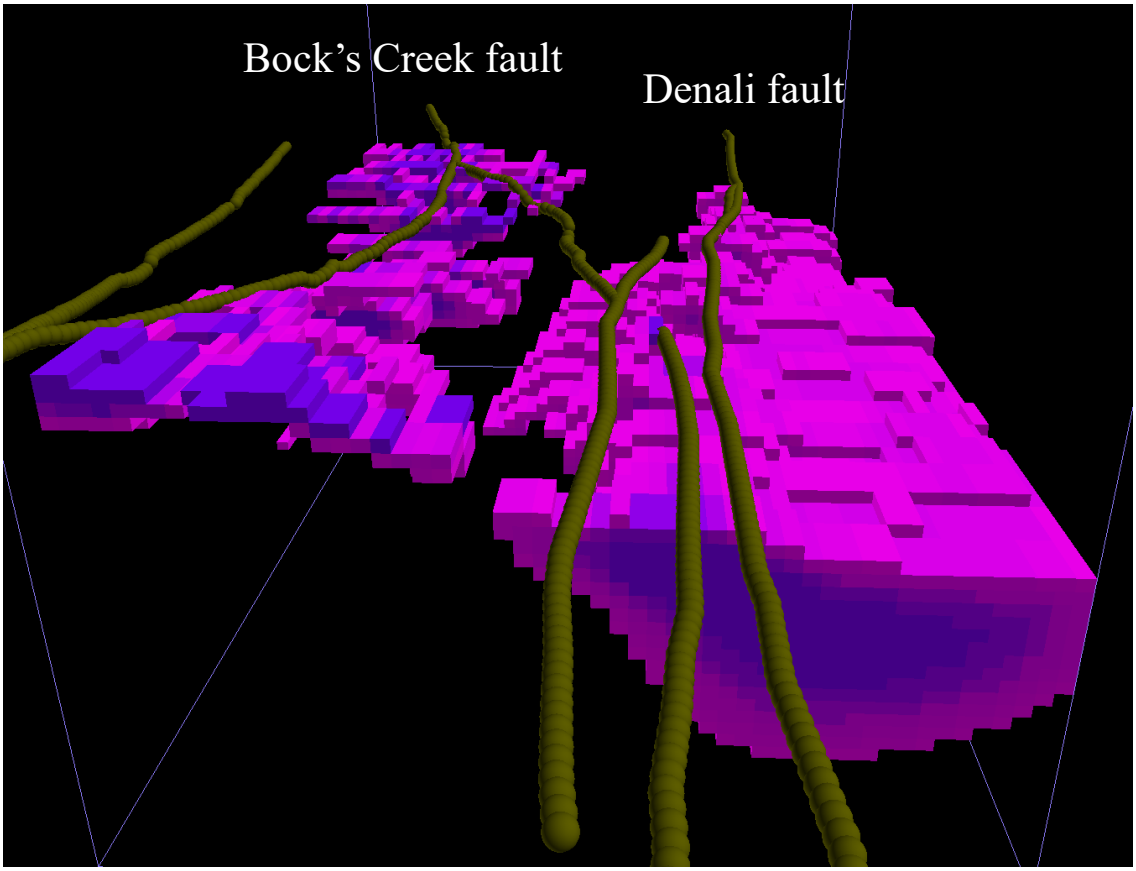

Figure 39 – Isolated high conductivity values (>0.05 S/m) compared with existing fault traces. The Denali fault shows a conductive anomaly that extends down over 1km. The conductive anomaly associated with Bock's Creek is only a few hundred meters thick. Figure is looking north.

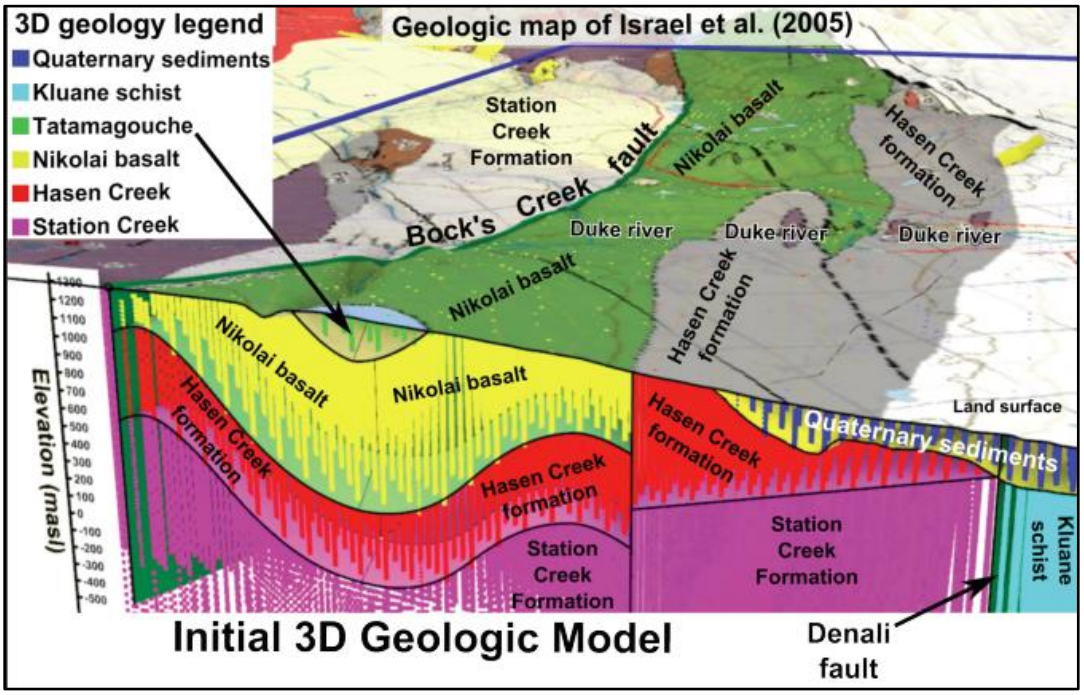

Figure 40 – Initial 3D geological model for Burwash Landing, YK. Figure modified from Witter (2020).

4.6 – Comparison with Geological Model

With the new 3D model complete, a reinterpretation of the geology and structural features is possible. The geological model provided by the YGS is described as a starting point with many assumptions taken. That said, it provides the most comprehensive model of the survey area and can be used to reinterpret the ELF data given the new inversion results. When the original model was interpreted, Witter (2020) noted a lack of similarity they attributed to 'a potentially more complex environment than once thought'. Using the 3D model, a simpler distribution of conductivities was found that could be more easily related to the previous geological interpretation. In the survey area, there are 6 major units, and two major structural features identified by previous work (Israel et al., 2005). A cross-section of the geological model is available in the YGS report between lines 7000 & 8000 of the ELF survey (Figure 39). The Nikolai basalt, Hasen Creek, and Station Creek Formation lie folded between the two major faults (Bock Creek & Denali). On the eastern side of the section, Quaternary sediments overlay the Denali fault trace with Kluane schist to the east of the fault. When the 2D section is compared to this geological model, only the Quaternary sediments can be identified, as noted by the author. The 3D model in this area is much closer to the template geology provided. In the 3D model, the Quaternary sediments are still visible to the east. Unlike the geological model, however, these sediments end when they reach the Denali fault trace (Figure 38). The large conductive anomaly under the Quaternary sediments on the eastern side of the fault are related to the Kluane Schist. While only one fault trace is shown on the geological model for the Denali fault, Bender & Haussler (2017) report multiple strands in this area. Since conductivity contrasts are being modelled, a potential explanation is that the response from the fault is overprinting the signal from the quaternary sediments. This cluster of fault traces is where the conductivity high approaches the surface. This has been attributed to the deformed Kluane unit (labelled DZ) to the northeast of the Denali fault. The deformation here has likely allowed fractures to open up and conductive fluids to reach shallow depths along this preferential pathway. To the southwest of the Denali fault splays, we see a much different subsurface structure compared to the 2D model. By grouping conductivity values by their strength, folding patterns can be seen (Figure 40). These are potentially related to one of the deformation events, most likely the late-Mesozoic since the folding seen is regional and not overturned or isoclinal. Farther southwest, the Bock's Creek fault strikes in the same direction as the Denali fault. Unlike the Denali fault, Bock's Creek fault trace is not as strong at depth. The fault motion for Bock's Creek is

unconstrained and has several small splays that could indicate its energy was dissipated along these instead of concentrated in one large structure like the Denali. The Bock's Creek fault trace follows a river which, combined with fracturing in the rock & the Nikolai Basalt signature, could cause the strong conductive anomaly that appears near-surface. The relationships identified between the initial geological model and the 3D conductivity model along this section were the basis for interpreting the rest of the 3D conductivity model.

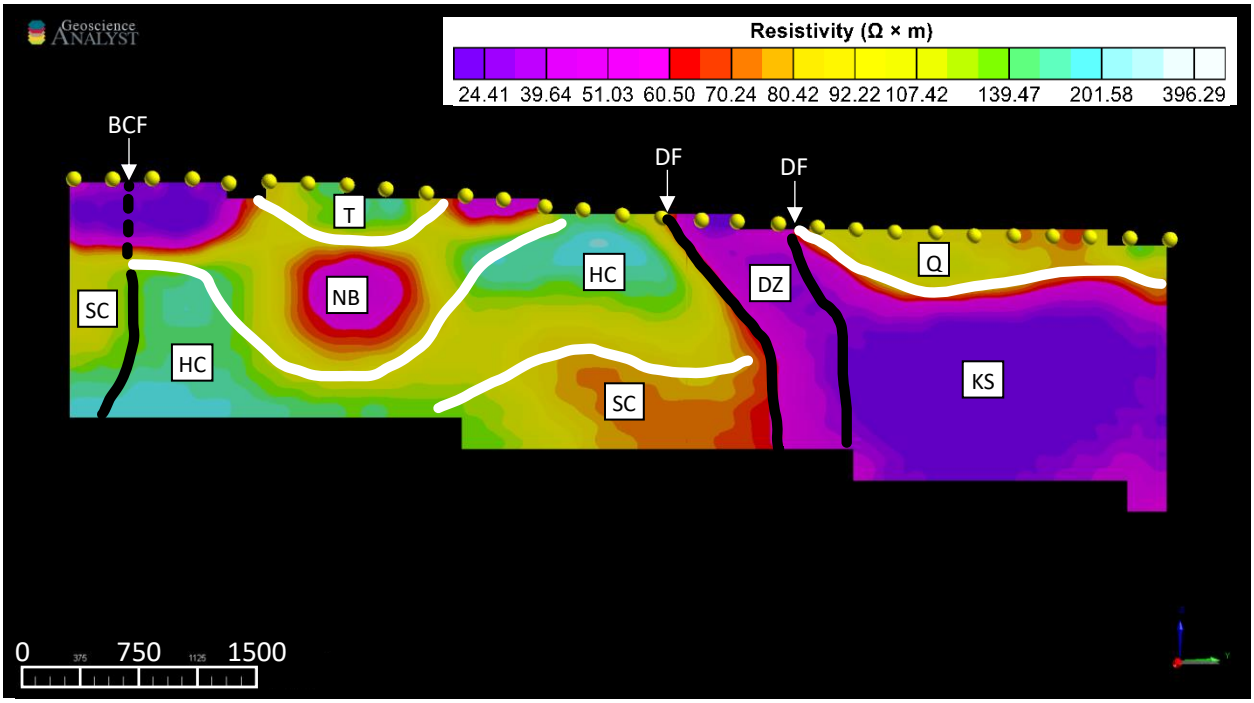

Figure 41 – Geological and structural interpretation of a section between line 7000 and 8000. Reader is looking northwest, perpendicular to the survey lines. WHITE LINES: Potential unit contacts, BLACK LINES: Potential fault traces, BCF: Bock's Creek Fault, DF: Denali Fault, SC: Station Creek Formation, NB: Nikolai Basalt, T: Tatamagouche, HC: Hansen Creek, DZ: Deformation Zone, KS: Kluane Schist, and Q: Quaternary Sediments.

4.7 – 3D Structural Interpretation

While comparisons can be made between the 3D conductivity slices, 2D resistivity slices, and geological model, interpreting the full 3D model is imperative. First, the model can be sliced horizontally at different depths to see how conductive anomalies change as we look deeper into the subsurface (Figure 41). Directly under the Denali Fault trace, the high conductive anomaly is seen at its shallowest (200 m). Looking deeper into the model, the conductive high coincides with the mapped Kluane Schist unit. Interestingly, around 1000 meters deep, there is an isolated high that could be a splay of the Denali fault that detached and subsequently deformed from dextral motion. This could also be a portion of Kluane Schist that has broken off due to the fault motion.

Since the signatures directly under the Denali Fault are too similar to differentiate from this isolated high, more surveying or drilling is needed to better understand this relationship. At greater depths, these two anomalies coalesce, potentially indicating a complex fault motion where dextral slip changes with depth (Figure 42).

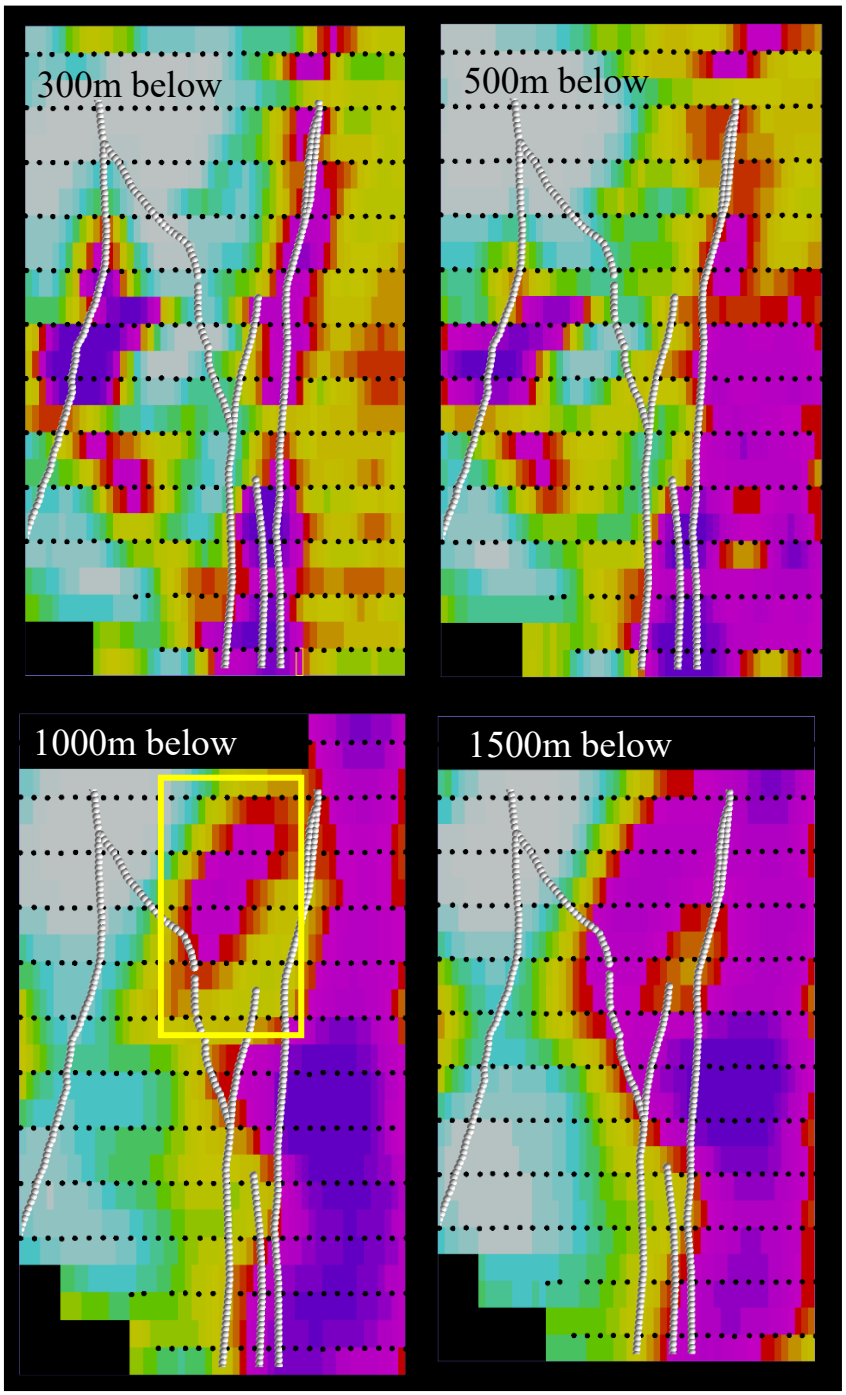

Figure 42 – Depth sections of 3D conductivity model. At shallow depths, a thin linear anomaly is seen. Slices looking deeper show the northeast as highly conductive. At 1000m below surface, a distinct conductive anomaly (yellow box) is seen before coalescing with the major anomaly by 1500m. Figure looking northwest.

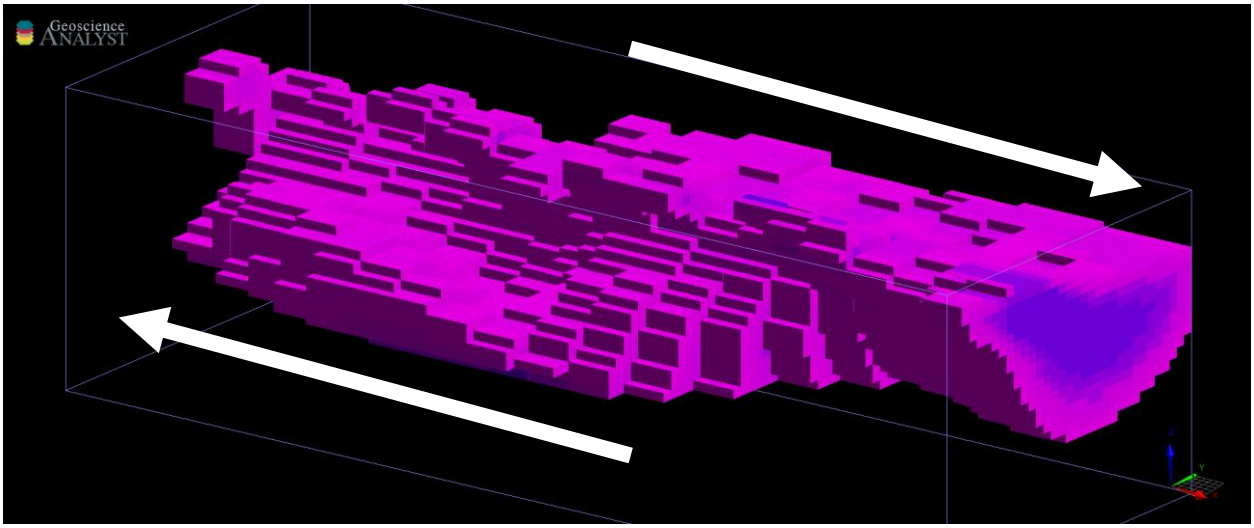

Figure 43 – High conductivity values (>0.05 S/m) related to the Denali fault trace with potential fault motion. Deformation along the Denali fault resulting from a transpressive regime could cause the complex fault shape seen in the center / northwest.

At depth, the southwestern portion of the survey area is dominated by two resistive highs that underlie two topographic highs. These conductive lows taper out toward the center of the block, with the near surface becoming highly conductive. When looking at slices of the model, there is a shallow conductive anomaly that follows Bock's Creek fault trace. As topography dips down between the two peaks, so does the shallow conductive anomaly. The anomaly is at its largest underneath the Duke River which transects Bock's Creek fault (Figure 43).

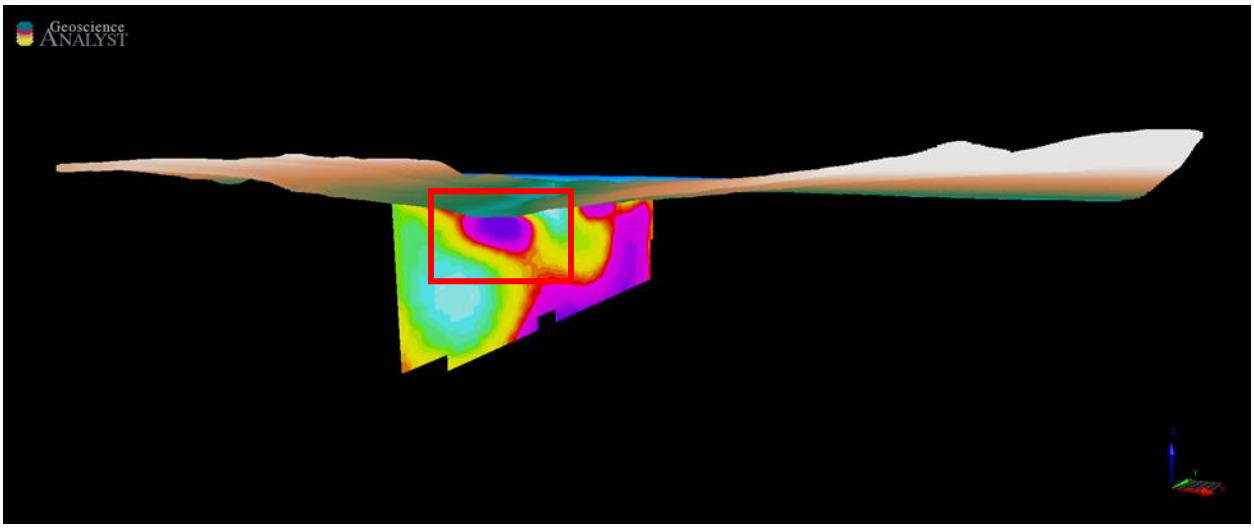

Figure 44 – 3D model section underneath the Duke River. Conductive anomaly highlighted with red box runs perpendicular to Bock's Creek fault. At depth, the anomaly comes close to coalescing with a broad, deep conductive anomaly.

No anomaly was directly associated with the entire Duke River trace so the conductive high seen underneath the southwest portion are attributed to deformation of Bock's Creek fault or potentially

surface water infiltrating the fractured basalt unit. Looking at across-line slices of the 3D model shows a clear indication of the complexity of the Denali fault trace (Figure 44). 500 meters southwest of the Denali Fault, a conductive anomaly is seen sitting approximately 1500 meters deep. The magnitude of the anomaly slightly increases but the spatial extent does not change as we approach the fault. As we approach the fault, a shallow conductive anomaly is seen to the southeast. The top of the anomaly is horizontal but at depth, we see thickening to the southeast. Northeast of the Denali fault, the two major conductive anomalies begin to coalesce and by 1500 meters from the fault, they are one anomaly. This pattern could be indicative of deformation around the Denali Fault and leads to a few interpretations. First, the work done by Israel et al. (2005) shows that along with dextral strike-slip, the Denali Fault also has some reverse fault motion. The greatest separation between the conductive anomalies is seen closest to the fault. Figure 44 (sections 2 – 4) could be showing the Kluane Schist (conductor) undergoing deformation and fracturing as it grinds across more competent rock. If reverse dextral strike-slip is occurring, the southwest portion of the Kluane Schist conductor appears to be detaching and thrusting upward. The second interpretation includes more than just the Kluane Schist. The Kluane Ultramafic Complex is a major plutonic unit southwest of the survey area but outcrops sporadically within the survey area. The deeper conductive anomaly southwest of the Denali fault (Figure 44 – Section 1) is underneath one of the mapped ultramafic intrusions. This could mean that the deeper anomaly is associated with one of these intrusions and the complex shape seen in figures 42 & 44 are a result of the Kluane Schist interacting with it. Fault traces mapped by Bender and Haussler (2017) show the Denali fault has a few splays that also coincide with a split in the conductive anomaly as seen in figure 39. The mapped fault trace connecting the Bock's Creek & Denali faults could also stem from the late intrusions as a means to relieve built up stress intruding rock. Evidence from the 3D model agrees with Israel et al. that the Denali fault motion is more complex than just strike-slip. This could indicate there is a deformation zone which, when combined with a regional scale fault, provides an ideal environment for geothermal fluids to circulate close to the surface. Witter (2020) proposed multiple drill locations for geothermal wells in part derived from the responses seen in the 2D resistivity model. These sites were reranked using the new 3D conductivity model (Figure 45).

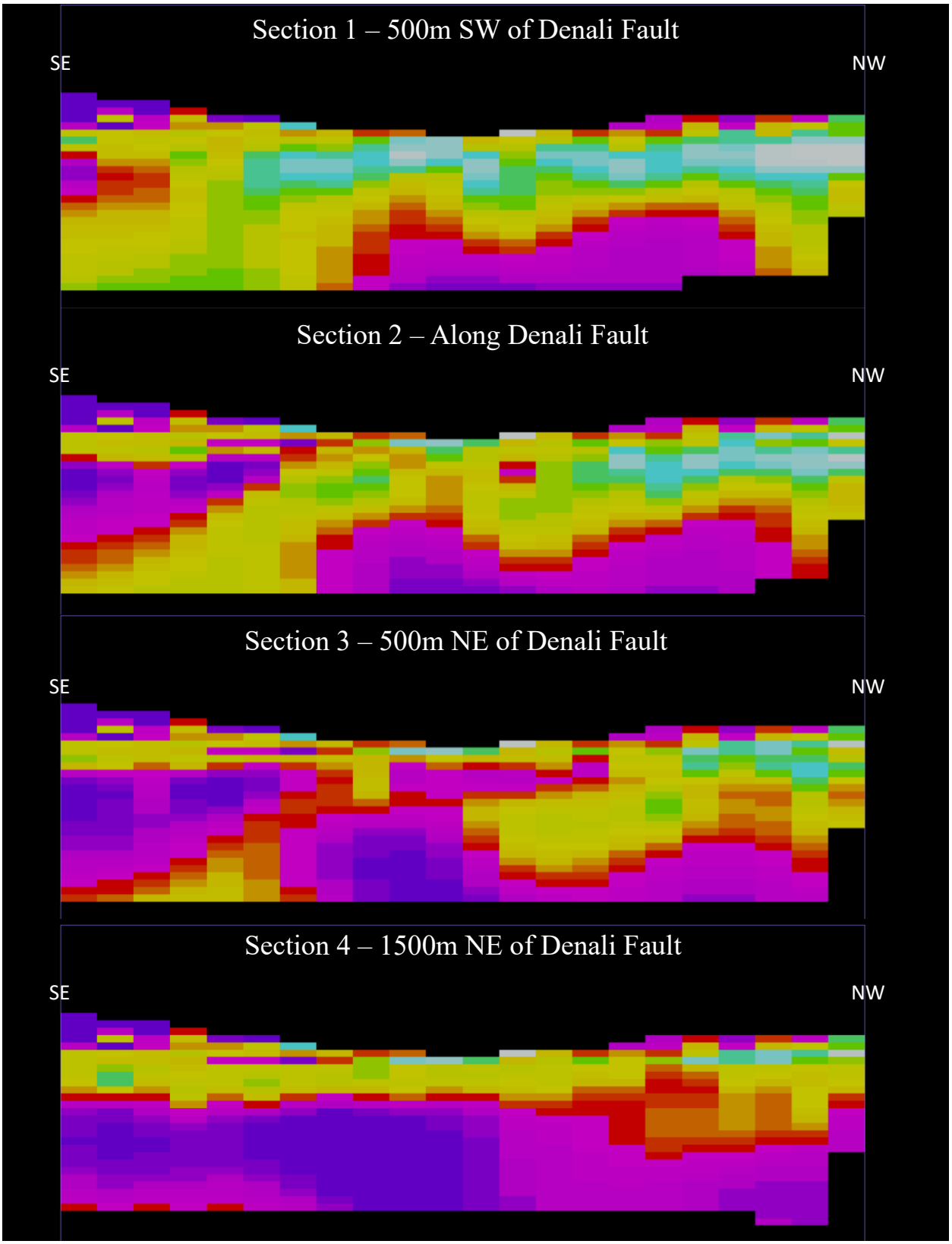

Figure 45 – Across line sections of the Burwash Landing 3D conductivity model. PURPLE: Conductive, TEAL/WHITE: Resistive. Conductive values were not of interest, just structure, so no colour bars were included.

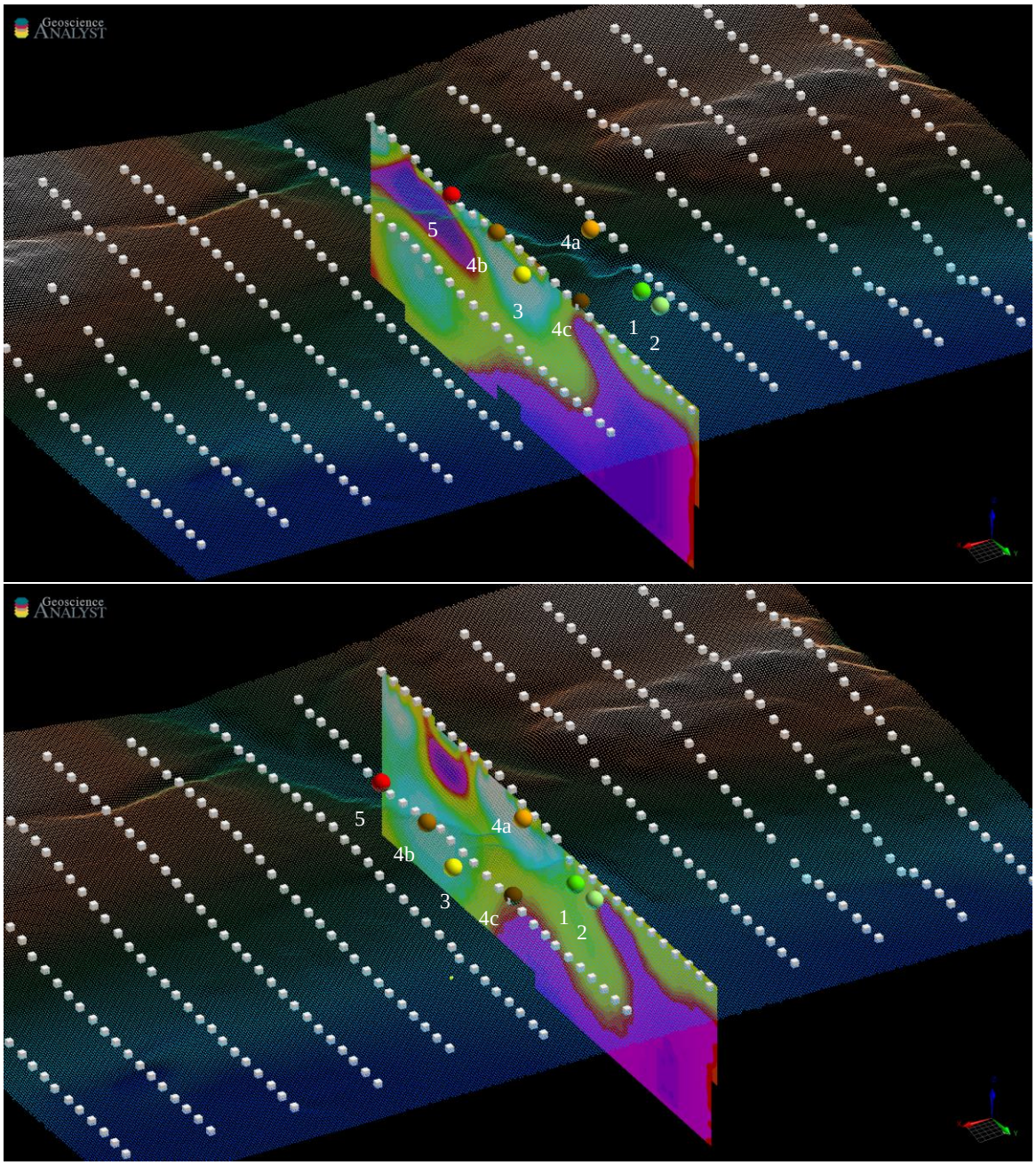

Figure 46 – Ranked geothermal drill locations recommended by Witter (2020) overlain on 3D conductivity model sections. (TOP) Conductivity section shown for Line 5000. (BOTTOM) Conductivity section shown for Line 4000. Figure is looking north.

Along with the criteria outlined by Witter (2020), the updated conductivity model shows a steeply dipping conductor underneath sites 1 & 2, keeping them the top priority targets. Site 4c was originally mapped as moderately resistive for the upper few hundred meters before becoming moderately conductive at depth. In the 3D model, 4c is located above the shallowest trace (~100m) of the conductive anomaly associated with the Denali Fault / Kluane Schist. This structure might require less drilling than some of the other proposed targets (i.e., target 3 which has no conductive

anomalies associated with it in the 3D model). Drill sites were identified around Bock's Creek Fault (4a, 4b, 5), but these conductivity contrasts do not extend very deep into the subsurface. The fact these targets are not road accessible either means they should be disregarded as drill sites unless constraining Bock's Creek fault by drilling would improve the geological model.

4.8 – Conclusions

The new conductivity model at Burwash Landing proved successful in identifying 3D structures not previously seen in the 2D sections. The 3D model provides a more geologically reasonable result that shows potential to relate conductivity ranges to different rock units. The Kluane Schist is clearly seen as a conductivity high with the Denali Fault trace having a similar signature. Laying over top the schist, Quaternary sediments have a low conductivity response and are seen throughout the survey on the eastern side of the Denali fault. Isolating conductive highs in the 3D model show a complex fault motion (Figure 42) consistent with the work of Israel et al. (2005). Between the two major fault structures, four regions of conductivity can be related to the Tatamagouche, Nikolai Basalt, Hasen Creek, and Station Creek Formations. Bock's Creek Fault does not show a similar signature to that seen at the Denali. The Bock's Creek fault trace is not as regional and only conductive in the top ~400 m of the subsurface. In terms of geothermal exploration, it would not be ideal to drill along this fault as access is poor and the fault does not show a deep conductive signature. The shallow conductive values at Bock's Creek fault could indicate hydrothermal fluids aren't upwelling into this area but fracturing of the Nikolai Basalt is allowing surface water to saturate near surface. There is a potential trace of the Bock's Creek fault at depth, but it is not consistent enough through the entire 3D model to say with certainty. Where Bock's Creek Fault and the Duke River intersect, a strong conductive anomaly is seen at depth. This anomaly might extend to a deeper conductive body that could also be associated with the Denali Fault. As for potential geothermal drill targets, the new ELF interpretation agrees with the two highest ranked sites (1 & 2). In addition, target 4c seems to be in a more favourable environment vs those ranked before it. Site 3, 4a, and 4b are in resistive units that extend down ~600-800 m. Site 5 has the worst access but is located on the strongest conductive anomaly seen at Bock's Creek fault. While the values obtained from inverting tipper data do not represent the real-world conductivity, the contrasts seen elucidate contacts between units, faults, and structures at depth. This knowledge can be used to help improve geological models, identify area of interest for more in-depth geophysical surveys, or identify potential drill locations for deep drilling.

5.0 - Conclusions & Future Work

Geophysical exploration is moving in two directions: re-evaluating previously discovered deposits (brownfield exploration) and discovering new ones at greater depth (greenfield exploration). This is due to the lack of near surface or easy-to-target mineral deposits (Ranjith et Al., 2017; McCutcheon & Walker, 2019; Xie, Konientzky, & Zhou, 2019). This thesis took the recent trends in exploration and used them to create a cost-effective workflow any geophysicist could follow to achieve meaningful conductivity models in the modern era. First, brownfield exploration at the Nash Creek deposit showed how re-evaluation of known deposits are valuable and can guide future exploration with a modern approach. By combining open-source spatial data sources with data from Callinex Mines Inc., a compilation of geophysical and geological information was used to create a 3D lithological model. This model was constructed using borehole data and field mapping as the primary influence with geophysics providing support when geological data was not available. The resulting model shows that a lack of structural constraint hindered understanding the deposit as well as how it interacted with the BPAB fault (west of this fault are older rocks with no evidence for VMS deposits). It was concluded that the BPAB fault must be constrained with geophysical surveying or drilled to understand the true scope of the Nash Creek deposit. The issue of overburden had no doubt hampered exploration at Nash Creek, but as deep-imaging geophysical methods mature, understanding structures at depth becomes a less daunting task. As proof of concept, the second chapter combined the deep imaging ELF-EM system with SimPEG, a recently updated open-source inversion package, to create a workflow for quickly and cost effectively identifying conductivity contrasts at depth. This new workflow was tested using data collected by the author at a known VMS deposit, Key Anacon, located within the BMC (to which Nash Creek is tangentially related). This deposit has been rigorously studied compared to Nash Creek and proved to be a better test location for the new 3D inversion workflow. Osisko Metals Inc. had previously constructed their own 3D model of the VMS deposit using borehole logging and MT / IP geophysical surveys. This wireframe model was compared to the resulting conductivity model produced by the ELF. The results were excellent, producing a ‘conductive envelope’ which encompassed most of the known sulphide lenses. The ELF system does not have the resolution to differentiate the lenses, but their attitude, dip, and spatial extent matched the general trend of the wireframe model. The ELF survey was acquired in one, two-week field deployment by two operators. The lack of cut lines, small crew size, and addition of open-source inversions, allow for

a 3D conductivity model to be produced without licencing fees making this highly inexpensive to produce. The resulting model, while lacking in resolution, elucidates structures buried deep beneath cover and proves to be an ideal reconnaissance tool for greenfield exploration programs or brownfield exploration where more constraint at depth is required (i.e., Nash Creek). Currently, the inversion results are strongly tied to the background conductivity of the starting model. As SimPEG continues to develop, improving the starting model is the clear next step. The ability to use an existing model is built into the open-source package but no voxel model existed at Key Anacon. This would be highly beneficial in brownfield exploration where prior information could be used to construct a starting model with known structures and varying conductivities instead of a unform half space with a single background conductivity value. Chapter four focused on reprocessing past ELF-EM surveys using the new SW workflow to compare results and how interpretation changed. The test site selected was Burwash Landing, Yukon along the Denali fault. Like the original interpretation, the reprocessed data showed a clear response related to the fault. Both models indicated hydrothermal fluids are most likely upwelling, using the fault as a conduit. The original 2D sections were discordant and had numerous near-vertical to vertical linear anomalies extending hundreds of meters into the subsurface. The interpretation in Witter (2020) describes these as artifacts of the inversion process and were not interpreted. In comparison, the SimPEG model lacked these anomalies (confirming them to be artefacts) and showed a clear fault trace with a variable dip of approximately 50-70 degrees northeast. Certain anomalies, such as the resistive Quaternary sediments near Kluane Lake, were present in both models. The recommended drill locations from Witter (2020) were reinterpreted and changed in a minor way (4c ranked higher than 3, 4a, and 4b). In general, however, the new 3D model shows there are several locations along the Denali fault that have greater potential to be drill targets in the future.

By combining modern computational methods and an underutilized survey technique, a cost-effective exploration tool has been presented in this thesis. This tool allows the user to assess several subsurface kilometers for conductivity contrasts and structure, at a moderate cost compared to other deep-imaging methods. Many facets of society rely on materials we take from the subsurface. These materials will continue to become harder to find and incur larger costs to extract. Regardless, exploration remains a necessity to push our understanding of where to find crucial materials and keep modern industries moving.

6.0 - References

Artimo, A., Mäkinen, J., Berg, R. C., Abert, C. C., & Salonen, V.-P. (2003). Three-dimensional geologic modeling and visualization of the Virttaankangas aquifer, southwestern Finland. *Hydrogeology Journal*, *11*(3), 378–386.

Bender, A. M., & Haeussler, P. J. (2017). *Eastern Denali Fault Surface Trace Map, Eastern Alaska and Yukon, Canada*. US Department of the Interior, US Geological Survey.

Bern, M. W., & Plassmann, P. E. (2000). Mesh Generation. *Handbook of computational geometry*, *38*.

Bongajum, E., White, I., Milkereit, B., Qian, W., Morris, W. A., Nasseri, M. H. B., & Collins, D. S. (2013). Multiparameter petrophysical characterization of an orebody: an exploration case history. In *Proceedings of the 3rd CANUS Rock Mechanics Symposium*.

Braden, B. (2012). Building a Better ELF. *Canadian Mining Journal*, *133*(6), 30–32.

Cagniard, L. (1953). Basic theory of the magneto-telluric method of geophysical prospecting. *Geophysics* , *18* (3), 605-635.

Chave, A. D., & Jones, A. G. (Eds.). (2012). *The magnetotelluric method: Theory and practice*. Cambridge University Press.

Chilès, J. P., Aug, C., Guillen, A., & Lees, T. (2004). Modelling the geometry of geological units and its uncertainty in 3D from structural data: the potential-field method. In *Proceedings of international symposium on orebody modelling and strategic mine planning*, 22, 313-320.

Cockett, R., Kang, S., Heagy, L. J., Pidlisecky, A., & Oldenburg, D. W. (2015). SimPEG: An open-source framework for simulation and gradient based parameter estimation in geophysical applications. *Computers & Geosciences*, *85*, 142-154.

de Groot-Hedlin, C., & Constable, S. (1990). Occam's inversion to generate smooth, two-dimensional models from magnetotelluric data. *Geophysics*, *55*(12), 1613-1624.

Dentith, M., & Mudge, S. T. (2014). *Geophysics for the mineral exploration geoscientist*. Cambridge University Press.

Desautels, P. (2019). Maiden Resource Estimate for the Bathurst Mining Camp, New Brunswick, Canada. *NI-43-101 Technical Report.*

Dostal, J., Wilson, R. A., & Keppie, J. D. (1989). Geochemistry of Siluro-Devonian Tobique volcanic belt in northern and central New Brunswick (Canada): tectonic implications. *Canadian Journal of Earth Sciences*, 26(6), 1282-1296.

Faulds, J., & Hinz, N. (2015). Favorable tectonic and structural settings of geothermal systems in the Great Basin region, western USA: Proxies for discovering blind geothermal systems. In *Proceedings World Geothermal Congress, Melbourne, Australia*. Nevada Bureau of Mines and Geology, University of Nevada, Reno.

Fyffe, L., & Fricker, A. (1987). Tectonostratigraphic terrane analysis of New Brunswick. *Atlantic Geology*, *23*(3), 113-122.

Geotech Ltd. (2013). Part II: ZTEM – Z-axis Tipper electromagnetics. In *Roundup: Geotech VTEM-ZTEM Workshop.*

Heagy, L. J., Cockett, R., Kang, S., Rosenkjaer, G. K., & Oldenburg, D. W. (2017). A framework for simulation and inversion in electromagnetics. *Computers & Geosciences*, *107*, 1-19.

Hebert, C. (2018). Multi-Parameter Analysis of Petrophysical and Geochemical Data for Base Metal Exploration (Unpublished master's thesis). University of Toronto, Toronto, Canada.

Heinson, G., Didana, Y., Soeffky, P., Thiel, S., & Wise, T. (2018). The crustal geophysical signature of a world-class magmatic mineral system. *Scientific reports*, *8*(1), 1-6.

Hildes, D. (2014). Halliday Lake, Saskatchewan, Extra Low Frequency (ELF-EM) Survey. Technical Note 2014-01.

Holtham, E., & Oldenburg, D. W. (2010). Three-dimensional inversion of ZTEM data. *Geophysical Journal International*, *182*(1), 168-182.

Holyland, P. W., & Ojala, V. J. (1997). Computer-aided structural targeting in mineral exploration: Two- and three-dimensional stress mapping. *Australian Journal of Earth Sciences*, *44*(4), 421–432.

Hulbert, L. J. (1997). *Geology and metallogeny of the Kluane mafic-ultramafic belt, Yukon Territory, Canada: Eastern Wrangellia, a new Ni-Cu-PGE metallogenic terrane* (Vol. 506). Geological Survey of Canada.

Israel, S., Tizzard, A., Major, J., Emond, D. S., Bradshaw, G. D., Lewis, L. L., & Weston, L. H. (2005). Bedrock geology of the Duke River area, parts of NTS 115G/2, 3, 4, 6 and 7, southwestern Yukon. *Yukon exploration and geology*, 139-154.

Jansen, J. C., & Cristall, J. A. (2017). Mineral exploration using natural EM fields. In *Proceedings of Exploration 17: Sixth Decennial International Conference on Mineral Exploration*. DMEC.

Kelbert, A., Meqbel, N., Egbert, G. D., & Tandon, K. (2014). ModEM: A modular system for inversion of electromagnetic geophysical data. *Computers & Geosciences*, *66*, 40-53.

Krieger, L., & Peacock, J. R. (2014). MTpy: A Python toolbox for magnetotellurics. *Computers & geosciences*, *72*, 167-175.

Kuzmin, P., Lo, B., & Morrison, E. (2005). Final report on modeling, interpretation methods and field trials of an existing prototype AFMAG system. *Ontario Geological Survey Misc Data Release*, *167*, 1-75.

Kowalczyk, P. L., & van Kooten, P. B. (2012). ZTEM data inversion and interpretation using the UBC-GIF MTinv3D code: A case history at the Silver Queen project, British Columbia. *ASEG Extended Abstracts*, *2012*(1), 1-4.

Labson, V. F., Becker, A., Morrison, H. F., & Conti, U. (1985). Geophysical exploration with audio frequency natural magnetic fields. *Geophysics*, *50*(4), 656-664.

Legault, J. (2010). ZTEM Tipper AFMAG Results over the Morrison Copper/Gold Porphyry deposit. *Geotech. Ltd. Case Study*.

Legault, J. (2012). Ten years of passive airborne AFMAG EM development for mineral exploration. In *2012 SEG Annual Meeting*.

Legault, J., Wilson, G. A., Gribenko, A. V., Zhdanov, M. S., Zhao, S., & Fisk, K. (2012). An overview of the ZTEM and AirMt airborne electromagnetic systems: A case study from the

Nebo-Babel Ni-Cu-PGE deposit, West Musgrave, Western Australia. *Preview*, *2012*(158), 26-32.

Lelievre, P., Oldenburg, D., & Williams, N. (2008). Constraining geophysical inversions with geologic information. In *SEG Technical Program Expanded Abstracts 2008*, 1223-1227. Society of Exploration Geophysicists.

L'Heureux, E., Ugalde, H., Qian W., Milkereit, B., & Nasui, C. (2007). An integrated geophysical study of orebody delineation, *CSEG Recorder Vol. 32*:36-39.

Lo, B., & Zang, M. (2008). Numerical modeling of Z-TEM (airborne AFMAG) responses to guide exploration strategies. In *SEG Technical Program Expanded Abstracts 2008* (pp. 1098-1102). Society of Exploration Geophysicists.

Lowey, G. W. (1998). A new estimate of the amount of displacement on the Denali fault system based on the occurrence of carbonate megaboulders in the Dezadeash Formation (Jura-Cretaceous), Yukon, and the Nutzotin Mountains sequence (Jura-Cretaceous), Alaska. *Bulletin of Canadian Petroleum Geology*, *46*(3), 379-386.

McCutcheon, S. R., & Walker, J. A. (2019). Great Mining Camps of Canada 7. The Bathurst Mining Camp, New Brunswick, Part 1: Geology and Exploration History. *Geoscience Canada: Journal of the Geological Association of Canada*, *46*(3), 137-154.

Noble, JPA (1976). Silurian stratigraphy and paleogeography, Pointe Verte area, New Brunswick, Canada. *Canadian Journal of Earth Sciences*, *13* (4), 537-546.

Pedersen, L. B. (1998). Tensor VLF measurements: Our first experiences. *Exploration Geophysics*, *29*(2), 52-57.

Prikhodko, A., Kuzmin, P. V., & Bagrianski, A. (2020). 60 Years of airborne AFMAG method evolution.

Schmucker, U. (1970). An introduction to induction anomalies. *Journal of geomagnetism and geoelectricity*, *22*(1-2), 9-33.

Simpson, F., & Bahr, K. (2005). *Practical magnetotellurics*. Cambridge University Press.

Siripunvaraporn, W., & Egbert, G. (2000). An efficient data-subspace inversion method for 2-D magnetotelluric data. *Geophysics*, *65*(3), 791-803.

Siripunvaraporn, W., Egbert, G., Lenbury, Y., & Uyeshima, M. (2005). Three-dimensional magnetotelluric inversion: data-space method. *Physics of the Earth and planetary interiors*, *150*(1-3), 3-14.

Siripunvaraporn, W., & Egbert, G. (2009). WSINV3DMT: vertical magnetic field transfer function inversion and parallel implementation. *Physics of the Earth and Planetary Interiors*, *173*(3-4), 317-329.

Smith, J. T., & Booker, J. R. (1991). Rapid inversion of two-and three-dimensional magnetotelluric data. *Journal of Geophysical Research: Solid Earth*, *96*(B3), 3905-3922.

Stanley, B. (2012). *Structural geology and geochronology of the Kluane Schist, southwestern Yukon Territory* (Master's thesis, University of Waterloo).

Ranjith, P. G., Zhao, J., Ju, M., De Silva, R. V., Rathnaweera, T. D., & Bandara, A. K. (2017). Opportunities and challenges in deep mining: a brief review. *Engineering*, *3*(4), 546-551.

Raybaut, P. (2009). Spyder-documentation. Available Online at: Pythonhosted.org.

Rikitake, T. (1950). Electromagnetic induction within the earth and its relation to the electrical state of the earth's interior. *Bull. Earthq. Res. Inst*, *28*, 45.

Rodi, W., & Mackie, R. L. (2001). Nonlinear conjugate gradients algorithm for 2-D magnetotelluric inversion. *Geophysics*, *66*(1), 174-187.

Tellus Explora. (2009). *Magnetotellurics (MT) Surveys*. Retrieved April 27, 2021, from http://www.tellus-explora.eu/methods/mt/

Tikhonov, A. N. (1950). On determining electrical characteristics of the deep layers of the Earth's crust. In *Doklady* (Vol. 73, No. 2, pp. 295-297).

Townend, J., Sutherland, R., Toy, V. G., Doan, M. L., Célérier, B., Massiot, C., ... & Zimmer, M. (2017). Petrophysical, geochemical, and hydrological evidence for extensive fracture-mediated fluid and heat transport in the Alpine Fault's hanging-wall damage zone. *Geochemistry, Geophysics, Geosystems*, *18*(12), 4709-4732.

Ugalde, H., L'Heureux, E., & Milkereit, B. (2007). An integrated geophysical study for orebody delineation, Nash Creek, New Brunswick. In *Proceedings of exploration 07: Fifth decennial international conference on mineral exploration* (pp. 1055–1058).

Ugalde, H., Morris, W. A., & van Staal, C. (2019). The Bathurst Mining Camp, New Brunswick: data integration, geophysical modelling, and implications for exploration. *Canadian Journal of Earth Sciences*, *56*(5), 433-451.

Van Rossum, G., & Drake Jr, F. L. (2014). The python language reference. *Python software foundation*.

van Staal, C. R. (1994). Brunswick subduction complex in the Canadian Appalachians: record of the Late Ordovician to Late Silurian collision between Laurentia and the Gander margin of Avalon. *Tectonics*, *13*(4), 946-962.

van Staal, C. R., Wilson, R. A., Kamo, S. L., McClelland, W. C., & McNicoll, V. (2016). Evolution of the Early to Middle Ordovician Popelogan arc in New Brunswick, Canada, and adjacent Maine, USA: Record of arc-trench migration and multiple phases of rifting. *GSA Bulletin*, 128(1-2), 122-146.

Veglio, E. (2017). Focused investigation of bedrock and associated base metal mineralization beneath glacial cover using geophysical, petrophysical, and petrological data in northern New Brunswick, Canada (Unpublished master's thesis). University of Toronto, Toronto, Canada.

Vozoff, K. (1972). The magnetotelluric method in the exploration of sedimentary basins. *Geophysics*, *37*(1), 98-141.

Wannamaker, P. E., Hohmann, G. W., & Ward, S. H. (1984). Magnetotelluric responses of three-dimensional bodies in layered earths. *Geophysics*, *49*(9), 1517-1533.

Ward, S. H. (1959). AFMAG—Airborne and ground. *Geophysics*, *24*(4), 761-787.

Ward, S. H., O'Donnell, J., Rivera, R., Ware, G. H., & Fraser, D. C. (1966). AFMAG—Applications and limitations. *Geophysics*, *31*(3), 576-605.

Wilson, R. A., & Kamo, S. L. (2012). The Salinic Orogeny in northern New Brunswick: geochronological constraints and implications for Silurian stratigraphic nomenclature. *Canadian Journal of Earth Sciences*, *49*(1), 222-238.

Wilson, R. A. (2013). Geology of the Charlo area (NTS 21 O/16. Part of 22 B/O1). Restigouche County. New Brunswick. New Brunswick department of Energy and Mines. Geological Survey Branch. Plate 2013-16 (revised 2015).

Wilson, R. A., McCutcheon, S. R., and Walker, J.A. (2014). Geology of the Nepisiguit Falls area (NTS 21 P/5). Gloucester County, New Brunswick. New Brunswick Depart of Energy and Mines. Geological Surveys Branch. Plate 2014-3.

Wilson, R. A., van Staal, C. R., & Kamo, S. L. (2017). Rapid transition from the Salinic to Acadian orogenic cycles in the northern Appalachian Orogen: Evidence from northern New Brunswick, Canada. *American Journal of Science*, 317(4), 449-482.

Witter, J. B., Miller, C. A., Friend, M., & Colpron, M. (2018). Curie point depths and heat production in Yukon, Canada. In *Proceedings, 43rd Workshop on Geothermal Reservoir Engineering. California* (pp. 1-11).

Witter, J.B., (2020). Early-stage exploration for geothermal energy resources along the Denali fault near Duke River, Yukon. Yukon Geological Survey, Open File 2020-3, 62 p.

Xie, H., Konietzky, H., & Zhou, H. W. (2019). Special issue “deep mining”. *Rock Mechanics and Rock Engineering*, *52*(5), 1415-1416.

7.0 - Appendices

Appendix A – ELF data file

Line	Point	LAT	LON	Alt	X	Y	GPSt	Pt	Rl	Az	Dur	IndNs	rE_0011	rN_0011	iE_0011	iN_0011	SNI_0011
2	1	45	0	0	3093428	7731078	123342	3.6	2.6	349.4	255	11.7	-0.352	0.75	0.503	-0.091	6.6
2	2	45	0	0	3093428	7731078	124738	1.4	-6.2	127.8	243	12.5	-0.689	0.529	0.546	0.073	7.4
2	4	45	0	0	3093428	7731078	131150	4.2	5	175.4	310	14.6	0.154	0.766	0.132	-0.206	21.7
2	3	45	0	0	3093428	7731078	132936	0.9	2.2	240.8	245	14.2	-0.313	0.795	0.494	-0.107	5.7
2	5	45	0	0	3093428	7731078	134449	0.2	-2.4	109.6	260	15.2	-0.074	0.783	0.353	-0.139	10.8
2	6	45	0	0	3093428	7731078	140018	2.6	-3	124.1	270	16	-0.729	0.441	0.38	-0.009	21.7
2	7	45	0	0	3093428	7731078	141358	4.9	0.5	103	265	16.5	-0.197	0.753	0.238	-0.099	21.7
2	8	45	0	0	3093428	7731078	142508	-0.5	1	47.6	253	17.4	-0.122	0.79	0.279	-0.11	16.6
2	9	45	0	0	3093428	7731078	143557	-6.2	-1	273.4	245	20.7	-0.222	0.755	0.067	-0.085	36.3
2	10	45	0	0	3093428	7731078	145046	6.6	1	348.9	275	26.4	0.1	0.774	0.167	-0.125	32.1
2	11	45	0	0	3093428	7731078	150458	3.4	1.1	97.9	270	22.2	0.311	0.792	0.246	-0.103	26.8
2	12	45	0	0	3093428	7731078	152102	5.6	4	225.9	250	20.1	0.632	0.632	0.14	-0.11	51.1
2	13	45	0	0	3093428	7731078	153613	-1.8	5.9	28.9	296	19.3	0.503	0.767	0.236	-0.045	25.3
1	13	45	0	0	3093428	7731078	155322	6.1	3.9	56.8	265	19.8	0.379	0.819	0.216	-0.098	24.8
0	13	45	0	0	3093428	7731078	160646	1	0	169.7	315	18.6	0.586	0.714	0.183	-0.138	39.1
3	12	45	0	0	3093428	7731078	163308	-0.5	5.8	40.6	240	19.7	0.163	0.853	0.152	-0.046	36.6
3	13	45	0	0	3093428	7731078	164656	-3.5	4.7	160.3	280	19	0.539	0.684	0.137	-0.086	36.7
3	11	45	0	0	3093428	7731078	170727	1.3	-0.5	242.6	290	19.9	0.368	0.78	0.271	-0.125	30
3	105	45	0	0	3093428	7731078	172320	2.8	0.3	240.1	240	21	0.345	0.818	0.16	-0.109	39.6
3	105	45	0	0	3093428	7731078	172613	2.9	0.4	239.6	123	20.6	0.305	0.858	0.185	-0.165	25.9
3	10	45	0	0	3093428	7731078	175003	1.5	-4.4	268.6	210	20.5	0.18	0.785	0.166	-0.112	40.7
3	95	45	0	0	3093428	7731078	180223	1.9	-2.7	302.7	330	19.6	0.227	0.853	0.154	-0.122	40.4
3	9	45	0	0	3093428	7731078	181107	2.7	-0.9	283.6	220	17.5	0.377	0.896	0.247	-0.099	27.5
3	85	45	0	0	3093428	7731078	182009	2.4	1.7	181	265	16.9	0.27	0.846	0.22	-0.119	30.3
3	8	45	0	0	3093428	7731078	183051	1.5	-1	235.2	264	16.6	0.311	0.836	0.284	-0.1	21.7
3	7	45	0	0	3093428	7731078	184104	3.1	-2.9	174.4	260	16.6	0.187	0.867	0.303	-0.058	21.4
3	6	45	0	0	3093428	7731078	185901	4.9	5	259.1	255	14.8	0.483	0.754	0.31	-0.217	11.4

NOTE – Only showing tipper components and signal to noise ratio for the 11Hz frequency. The full data file would have the last 5 columns repeated for each frequency (22, 45, 90, 180, 360, 720, & 1440 Hz).

Appendix B – ELF Inversion Code

```
'''
@author: Alexander Furlan
@version: 1.0
--------------------------------------------------------------------------------
ELF tipper inversion using SimPEG. (OcTree Version)
--------------------------------------------------------------------------------

Requirements:
--------------------------------------------------------------------------------
  1)  SimPEG + SimPEG branch:
      https://github.com/MiraGeoscience/simpeg.git@feature/tiled-simulations

  2)  ELF file (Geosoft .xyz export) Note: Remove noisy stations & repeats
      before export. They will be assigned a dummy value in this script.

  3)  DEM file (Convert raster to .xyz points) Note: Testing completed using
      .xyz's created in GrassGIS, Oasis Montaj, ArcMap, & ArcGIS Pro.


Notes:
--------------------------------------------------------------------------------
  []  It's recommended you rotate your data if you don't have a big boi PC.

      Test PC;
      Processor: Intel(R) Core(TM) i7-8750H CPU @ 2.20GHz (12 CPUs)
      Memory (RAM): 16384 MB

      Test dataset was NW-SE trending and could not be inverted with decent
      parameters on the above PC (Many...many...memory errors). Rotating your
      data minimizes the mesh size.


  []  Since Aurora's workflow is through Geosoft, an .xyz export of a montaj
      database was used. CSV style could be added rather easily.

      IMPORTANT: Export gdb using the 'comment header' option. The code below
                 relies on it. Header should look like this:

     / ------------------------------------------------------------------
     / XYZ EXPORT [MM/DD/YYYY]
     / DATABASE   [../File_Location/ELF.gdb]
     / ------------------------------------------------------------------
     /
     /   Line    Point                  X                    Y
     /======== ======== ====================== ========================
     /

  []  Base cell sizes are defined by the user. OcTree Levels is an array of
      values which defines how quickly the cell widths grow away from a given
      point.

      EX  If base cell size was 50m:
            octree_levels = [1,3,5]
          would produce:
```

```
            50, 100, 100, 100, 200, 200, 200, 200, 200

    [] Background conductivity is assigned by the user. It's best to choose a
       conductivity that's representative of the area the survey was recorded.


Menu Parameters (Default):
---------------------------------------------------------------------------
    1) X cell size   |
    2) Y cell size   |--- Adjust for station/line spacing of survey
    3) Z cell size   |

                     |   Output .mod & .msh will have this name. Keep it
    4) Output filename   |--- simple. The code will append the background
                     |   conductivity value chosen.

    5) Max iterations    |--- Max # of iterations for inversion.

                     |   Padding must be at least 1 skin depth of the
    6) Padding distance  |--- lowest frequency.
                     |
                         |   Octree_levels is used to define the rate
                         |   of cell width increase. (Radial) is a
                         |   radius of cells around the given data
    7) Octree Levels (Radial)   |   point. (Surface) increases cell size
           &                    |--- directly downward only. Surface is used
    8) Octree Levels (Surface)  |   to speed up processing time on a 'slow'
                         |   computer. Ideally, only radial would be
                         |   used. It's up to the user to decide what
                         |   works best.

                          |   Starting point for inversion. Since we
                          |   aren't measuring absolute conductivity,
    9) Background conductivity  |--- it's recommended you rerun the inversion
                          |   with multiple starting values & use the
                          |   averaging script. (1e-02)

                  |   Check off the frequencies you wish to use. You
                  |   should have an idea of what's useful after going
   11) Frequencies  |--- through ELF QAroot & plotting total divergence or
                  |   total phase rotation. Add padding if using 11 Hz.
                  |   (22, 45, 90, 180, 360)
'''
# Imports (Don't be fooled, dask/utils are used)
# ---------------------------------------------------------------------------
import numpy as np
import matplotlib.pyplot as plt
from mpl_toolkits.axes_grid1 import make_axes_locatable
from os import getcwd, mkdir, remove, path
from tkinter import Tk, filedialog
from tkinter import Frame, Label, Entry, IntVar, Checkbutton, Button
from time import time
from sys import exit
from discretize import TreeMesh
from discretize.utils import mkvc, refine_tree_xyz, mesh_builder_xyz
from SimPEG import maps, data, optimization, objective_function, utils
```

```
from SimPEG.utils import plot2Ddata, surface2ind_topo
from SimPEG import regularization, inverse_problem, directives, inversion
from SimPEG import data_misfit, dask
from SimPEG.electromagnetics import natural_source as ns
from dask.distributed import Client, LocalCluster
from pymatsolver import Pardiso as Solver


# onClosing()
# ----------------------------------------------------------------------------
# Destroys the root window if you hit the 'x' button while operating the menu.
def onClosing():
    root.destroy()
    exit()


# Base tkinter window
# ----------------------------------------------------------------------------
root = Tk()
root.withdraw()
root.attributes("-topmost", True)
root.title('Santas Workshop.')
root.resizable(height=False, width=False)
root.protocol("WM_DELETE_WINDOW", onClosing)


# build()
# ----------------------------------------------------------------------------
# This function prepares the data for inversion. First, it imports the ELF and
# DEM data. Next, it asks the user for a series of parameters (explained above)
# and uses these to build the mesh / set certain variables. It defines some
# global variables for the other main functions in this code.
def build():
    global cd, receiver_locations, frequencies, Emax, Emin
    global mesh, meshTENSOR, topo_xyz, ELFimport, std, cell_array

# offClick()
# ----------------------------------------------------------------------------
# This function disables the unneeded parameters when using a previously
# buit mesh. It's also used to signal the code for said mesh file.
    def offClick():
        xe["state"] = "disabled"
        ye["state"] = "disabled"
        ze["state"] = "disabled"
        octe["state"] = "disabled"
        octe2["state"] = "disabled"

    # cells()
    # ----------------------------------------------------------------------------
    # This function grabs the given input parameters and stores them.
    def cells():
        root.fn = fe.get()
        root.it = int(ie.get())
        root.bgcv = float(bge.get())
        # root.pv = (float(pe.get())/100)
        # root.nv = float(nf.get())
```

```
    root.sv = float(sw.get())
    root.bv = float(be.get())
    root.cv = float(ce.get())
    root.f1 = var1.get()
    root.f2 = var2.get()
    root.f3 = var3.get()
    root.f4 = var4.get()
    root.f5 = var5.get()
    root.f6 = var6.get()
    root.f7 = var7.get()
    root.f8 = var8.get()
    root.xc = int(xe.get())
    root.yc = int(ye.get())
    root.zc = int(ze.get())
    root.octr = octe.get()
    root.octr2 = octe2.get()
    root.mv = 0
    '''
    root.mv = 1
    if xe['state'] != 'disabled':
        root.xc = int(xe.get())
        root.yc = int(ye.get())
        root.zc = int(ze.get())
        root.octr = octe.get()
        root.octr2 = octe2.get()
        root.mv = 0
    '''
    root.quit()

# Select ELF & DEM files
# ---------------------------------- ----------------------------------
# Here, the code asks for your formatted ELF and DEM files. It will load
# them as needed by SimPEG to run the inversion. Standard Oasis Montaj
# dummies (*) are given a very small data value with a very large error.
#
# receiver_locations & topo_xyz are 2D arrays. The first variable specifies
# the ELF reading. The second variable specifies the x, y, or z value.
#
# EX   receiver_locations[0]   = would call the first ELF station.
#      receiver_locations[0,0] = would call the 'X' location of the first
#                                ELF station.
title = 'Please select ELF file'
cd = getcwd()
fn = filedialog.askopenfilenames(initialdir=cd, title=title,
                                 filetypes=[('XYZ', '.xyz')])
fname = fn[0]

file = open(fname, 'r')
hdrf = file.readlines()
hdr = hdrf[5]
hdrlst = hdr.split()
hdrlst.pop(0)
file.close()

ELFxyz = np.genfromtxt(fname, skip_header=8, names=hdrlst,
                       filling_values=4.20e-10)
```

```
xrx, yrx, zrx = ELFxyz['X'], ELFxyz['Y'], ELFxyz['Alt']
receiver_locations = np.c_[mkvc(xrx), mkvc(yrx), mkvc(zrx)]

title = 'Please select DEM file'
dn = filedialog.askopenfilenames(initialdir=cd, title=title,
                                 filetypes=[('XYZ', '.xyz')])
dname = dn[0]

DEMlst = ['X', 'Y', 'Z']
DEMxyz = np.genfromtxt(dname, names=DEMlst)

xx, yy, zz = DEMxyz['X'], DEMxyz['Y'], DEMxyz['Z']
topo_xyz = np.c_[mkvc(xx), mkvc(yy), mkvc(zz)]
topo_xyz = topo_xyz[1:]

del DEMxyz, xx, yy, zz, xrx, yrx, zrx

root.deiconify()
root.update()

# ----------------------------------------------------------------------
# Menu stuff....skip to the next underlined comment (367) unless you care.
# ----------------------------------------------------------------------

# Mesh frame
xyz = Frame(root, bg='#ffbf00', bd=5, highlightthickness=5)
xyz.grid(row=1, column=1, pady=(10, 0))

Label(xyz, text='Mesh Parameters', bg='#ffbf00').grid(row=1, column=1,
                                                     columnspan=2)

Label(xyz, text='X:', bg='#ffbf00').grid(row=2, column=1, sticky='e')
xe = Entry(xyz)
xe.grid(row=2, column=2)

Label(xyz, text='Y:', bg='#ffbf00').grid(row=3, column=1, sticky='e')
ye = Entry(xyz)
ye.grid(row=3, column=2)

Label(xyz, text='Z:', bg='#ffbf00').grid(row=4, column=1, sticky='e')
ze = Entry(xyz)
ze.grid(row=4, column=2)

Label(xyz, text='Octree Levels (Radial):', bg='#ffbf00').grid(row=5,
                                                             column=1,
                                                             sticky='e')
octe = Entry(xyz)
octe.grid(row=5, column=2)

Label(xyz, text='Octree Levels (Surface):', bg='#ffbf00').grid(row=6,
                                                              column=1,
                                                              sticky='e')
octe2 = Entry(xyz)
octe2.grid(row=6, column=2)
'''
Button(xyz, text='Mesh Built', bg='#ffbf00',
```

```
      command=offClick).grid(row=7, column=1, columnspan=2, pady=(10, 0))
'''

# Parameter frame
op = Frame(root, bg='#ffbf00', bd=5, highlightthickness=5)
op.grid(row=1, rowspan=2, column=2, sticky='n', pady=(0, 1))
Label(op, text='Output Parameters', bg='#ffbf00').grid(row=1, column=1,
                                          columnspan=2)

Label(op, text='Max Iterations:', bg='#ffbf00').grid(row=2, column=1,
                                        sticky='e')
ie = Entry(op)
ie.grid(row=2, column=2)
ie.insert(-1, 10)

Label(op, text='Background Conductivity:', bg='#ffbf00').grid(row=3,
                                             column=1,
                                             sticky='e')
bge = Entry(op)
bge.grid(row=3, column=2)
bge.insert(-1, 1e-2)

'''
Label(op, text='Percent Error (%):', bg='#ffbf00').grid(row=4, column=1,
                                        sticky='e')
pe = Entry(op)
pe.grid(row=4, column=2)
pe.insert(-1, 15)

Label(op, text='Noise Floor:', bg='#ffbf00').grid(row=5, column=1,
                                      sticky='e')
nf = Entry(op)
nf.grid(row=5, column=2)
'''

Label(op, text='Sensitivity Weights:', bg='#ffbf00').grid(row=6, column=1,
                                        sticky='e')
sw = Entry(op)
sw.grid(row=6, column=2)
sw.insert(-1, 1e-6)

Label(op, text='Beta:', bg='#ffbf00').grid(row=7, column=1, sticky='e')
be = Entry(op)
be.grid(row=7, column=2)
be.insert(-1, 1)

Label(op, text='Chi:', bg='#ffbf00').grid(row=8, column=1, sticky='e')
ce = Entry(op)
ce.grid(row=8, column=2)
ce.insert(-1, 1)

Label(op, text='Output Filename:', bg='#ffbf00').grid(row=9, column=1,
                                        sticky='e')
fe = Entry(op)
fe.grid(row=9, column=2)
```

```
# Frequency frame
ff = Frame(root, bg='#ffbf00', bd=5, highlightthickness=5)
ff.grid(row=1, column=3, sticky='n', pady=(15, 0))
Label(ff, text="Select frequencies:",
     bg='#ffbf00').grid(row=1, column=1, columnspan=2)

var1 = IntVar(ff)
Checkbutton(ff, text="0011", variable=var1,
          bg='#ffbf00').grid(row=2, column=1)
var2 = IntVar(ff, value=1)
Checkbutton(ff, text="0022", variable=var2,
          bg='#ffbf00').grid(row=3, column=1)
var3 = IntVar(ff, value=1)
Checkbutton(ff, text="0045", variable=var3,
          bg='#ffbf00').grid(row=4, column=1)
var4 = IntVar(ff, value=1)
Checkbutton(ff, text="0090", variable=var4,
          bg='#ffbf00').grid(row=5, column=1)
var5 = IntVar(ff, value=1)
Checkbutton(ff, text="0180", variable=var5,
          bg='#ffbf00').grid(row=2, column=2)
var6 = IntVar(ff, value=1)
Checkbutton(ff, text="0360", variable=var6,
          bg='#ffbf00').grid(row=3, column=2)
var7 = IntVar(ff)
Checkbutton(ff, text="0720", variable=var7,
          bg='#ffbf00').grid(row=4, column=2)
var8 = IntVar(ff)
Checkbutton(ff, text="1440", variable=var8,
          bg='#ffbf00').grid(row=5, column=2)

Button(root, text="Start Inversion.", command=cells, cursor='target',
     bg='#ffbf00').grid(row=2, column=3, sticky='s', pady=(0, 10))
root.mainloop()

# Determing which frequencies & components to use for inversion.
# ----------------------------------------------------------------------
# The code will filter out frequencies not selected in the menu to create
# the final frequency list. A similar process is used for tipper components
# but with the addition of flattening the array after removing the unused
# components. The order of components in the input ELF data doesn't matter,
# it's reordered correctly here.
frequencies = [11, 22, 45, 90, 180, 360, 720, 1440]
gFQ = [root.f1, root.f2, root.f3, root.f4,
      root.f5, root.f6, root.f7, root.f8]
products = []
for num1, num2 in zip(gFQ, frequencies):
   products.append(num1 * num2)
frequencies = list(filter((0).__ne__, products))

keys = [
   ['rE_0011', 'iE_0011', 'rN_0011', 'iN_0011'],
   ['rE_0022', 'iE_0022', 'rN_0022', 'iN_0022'],
   ['rE_0045', 'iE_0045', 'rN_0045', 'iN_0045'],
   ['rE_0090', 'iE_0090', 'rN_0090', 'iN_0090'],
   ['rE_0180', 'iE_0180', 'rN_0180', 'iN_0180'],
```

```
    ['rE_0360', 'iE_0360', 'rN_0360', 'iN_0360'],
    ['rE_0720', 'iE_0720', 'rN_0720', 'iN_0720'],
    ['rE_1440', 'iE_1440', 'rN_1440', 'iN_1440']
    ]

'''
keys = [
    ['rN_0011', 'iN_0011', 'rE_0011', 'iE_0011'],
    ['rN_0022', 'iN_0022', 'rE_0022', 'iE_0022'],
    ['rN_0045', 'iN_0045', 'rE_0045', 'iE_0045'],
    ['rN_0090', 'iN_0090', 'rE_0090', 'iE_0090'],
    ['rN_0180', 'iN_0180', 'rE_0180', 'iE_0180'],
    ['rN_0360', 'iN_0360', 'rE_0360', 'iE_0360'],
    ['rN_0720', 'iN_0720', 'rE_0720', 'iE_0720'],
    ['rN_1440', 'iN_1440', 'rE_1440', 'iE_1440']
    ]
'''
products = []
for num1, num2 in zip(gFQ, keys):
    products.append(num1 * num2)
keys = list(filter(([]).__ne__, products))
keys = [item for sublist in keys for item in sublist]

# Mesh building
# ------------------------------------------------------------------------
# If mesh parameters are given by the user, the code will use the cell
# sizes and OcTree values given to create a new mesh file. Padding is
# calculated dynamically using the lowest frequency & background
# conductivity selected by the user along with the skin depth eqn. If the
# "Mesh Built" button is pressed, the code will ask the user for a mesh
# file & load it in as a TreeMesh object instead.
'''
if root.mv == 1:
    title = 'Please select mesh file'
    mn = filedialog.askopenfilenames(initialdir=cd, title=title,
                                     filetypes=[('Mesh', '.msh')])
    mname = mn[0]
    mesh = TreeMesh.readUBC(mname)
    cfile = open(mname, 'r')
    cl = cfile.readlines()
    cv = cl[2].split()
    cell_array = [float(val) for val in cv]
    cfile.close()

else:
    print("\nCreating mesh...")
    skn_d = round((503.8 * np.sqrt(1/(frequencies[0]*root.bgcv))), -2)
    # shallow = round((503.8 * np.sqrt(1/(frequencies[-1]*root.bgcv))), -1)
    # print(f'\nShallow Skin Depth: {shallow}m.')
    print(f'\nSkin Depth: {skn_d}m.')
    cell_array = [root.xc, root.yc, root.zc]

    pad_array = [[skn_d*2, skn_d*2],
                 [skn_d*2, skn_d*2],
                 [skn_d*2, 0]]
    octree = []
```

```
    octree2 = []
    root.octr = root.octr.split(',')
    for val in root.octr:
        octree.append(int(val))
    root.octr2 = root.octr2.split(',')
    for val in root.octr2:
        octree2.append(int(val))
'''
print("\nCreating mesh...")
skn_d = round((503.8 * np.sqrt(1/(frequencies[0]*root.bgcv))), -2)
# shallow = round((503.8 * np.sqrt(1/(frequencies[-1]*root.bgcv))), -1)
# print(f'\nShallow Skin Depth: {shallow}m.')
print(f'\nSkin Depth: {skn_d}m.')

cell_array = [root.xc, root.yc, root.zc]

pad_array = [[skn_d*2, skn_d*2],
             [skn_d*2, skn_d*2],
             [skn_d*2, 0]]

octree = []
octree2 = []
root.octr = root.octr.split(',')
for val in root.octr:
    octree.append(int(val))
root.octr2 = root.octr2.split(',')
for val in root.octr2:
    octree2.append(int(val))

# OcTree MESH
mesh = mesh_builder_xyz(receiver_locations, cell_array,
                        padding_distance=pad_array,
                        mesh_type='tree'
                        )
# Mesh refinement based on topography
mesh = refine_tree_xyz(mesh, topo_xyz, octree_levels=[0, 0, 0, 1],
                       method="surface", finalize=False)
# Mesh refinement near receivers
mesh = refine_tree_xyz(mesh, receiver_locations, octree_levels=octree,
                       method="radial", finalize=False)
mesh = refine_tree_xyz(mesh, topo_xyz, octree_levels=octree2,
                       method="surface", finalize=False)
mesh.finalize()

print("\nMesh Complete.")

# Creating the ELF data array for SimPEG & extracting info for figures.
# ----------------------------------------------------------------------
# Here, the final ELF import and standard deviation array are created. Each
# tipper component value is assigned the standard deviation calculated from
# all values in that component. Since dummies in the original import were
# assigned a specific value, they are easily identified and given a large
# standard deviation.
var = []
std = []
Emax = []
```

```
    Emin = []
    ELFimport = np.array([])
    for key in keys:
        ELFxyz[key] = (ELFxyz[key] * -1)  # SimPEG & ELF seem to disagree.
        val = np.std(ELFxyz[key])
        emax = np.max(ELFxyz[key])
        emin = np.min(ELFxyz[key])
        var = np.append(var, val)
        Emax = np.append(Emax, emax)
        Emin = np.append(Emin, emin)
        ELFimport = np.append(ELFimport, ELFxyz[key])
    c = 0
    c1 = 0
    for num in ELFimport:
        if num == 4.2e-10:
            std = np.append(std, 1e10)
        else:
            std = np.append(std, var[c1])
        if c == len(receiver_locations):
            c = 0
            c1 += 1
        else:
            c += 1

    # np.savetxt('ELF_DATA.csv', ELFimport, delimiter=',')
    del gFQ, products, var, ELFxyz
    root.withdraw()
    '''
    root.destroy()
    exit()
    '''


# run()
# ----------------------------------------------------------------------------
# This is where the magic happens. The user set parameters, and newly formatted
# ELF / DEM data is used to run an inversion. This uses a lot of RAM and CPU
# power. It's recommended you don't use other apps while running it. That said,
# a server might fair better than the laptop used to test it.
def run():
    global dpred, f_n

# Prep work
# ----------------------------------------------------------------------------
# At this stage, the data is properly formatted and readable by SimPEG. We
# start by defining the file name and some stuff for dask.
    cluster = LocalCluster(processes=False)
    client = Client(cluster)
    f_n = '{}_{}'.format(root.fn, root.bgcv)

    # Conductivity in S/m
    air_conductivity = np.log(1e-10)
    background_conductivity = np.log(root.bgcv)

    # Find cells that are active for forward modeling (cells below surface)
    active_cells = surface2ind_topo(mesh, topo_xyz)
```

```
# active_cells =

# Define mapping from model to active cells
expmap = maps.ExpMap(mesh)
model_map = expmap * maps.InjectActiveCells(mesh, active_cells,
                                    air_conductivity)

# Define starting model. Models in SimPEG are vector arrays
# model = background_conductivity * np.ones(active_cells.sum())
m_bg = background_conductivity * np.ones(active_cells.sum())
model = np.ones(mesh.n_cells) * background_conductivity
indices = mesh._get_containing_cell_indexes
indices = indices(receiver_locations)
model[indices] = root.bgcv
model = model[active_cells]

# Create receivers
# ------------------------------------------------------------------------
# receiver_locations (from run()) are used to create a 3D tipper Rx
# masterlist. It includes real and imaginary components for two
# orientations. This is referencing the rE_XXXX, rN_XXXX, iE_XXXX, iN_XXXX
# components from the ELF dataset.
rxList = []
for rx_orientation in ['zx', 'zy']:
    rxList.append(ns.Rx.Point3DTipper(receiver_locations, rx_orientation,
                                'real'))
    rxList.append(ns.Rx.Point3DTipper(receiver_locations, rx_orientation,
                                'imag'))
# Source list
# ------------------------------------------------------------------------
# This creates a series of EM sources based on the frequencies selected by
# the user. Since we're looking at extremely low frequency sources, we can
# assume they act as planewaves, simplifying the math.
srcList = [
    ns.Src.Planewave_xy_1Dprimary(rxList, freq,
                              sigma_primary=model_map * m_bg)
    for freq in frequencies
]

# Setting up the tipper survey object
# ------------------------------------------------------------------------
# rel_err = (root.pv * abs(ELFimport))
# nse_flr = root.nv
survey = ns.Survey(srcList)
survey.dobs = ELFimport
survey.std = std
# survey.std = np.add(rel_err, (nse_flr*np.ones_like(rel_err)))
survey.locations = receiver_locations

data_obj = data.Data(survey, dobs=survey.dobs,
                     standard_deviation=survey.std)

# data_obj = data.Data(survey, dobs=survey.dobs,
#                      relative_error=rel_err,
#                      noise_floor=nse_flr)
```

```
# Setting up the problem object / Define the forward simulation
# ------------------------------------------------------------------------
sP = model_map*m_bg
simulation = ns.Simulation3DPrimarySecondary(mesh=mesh,
                                    survey=survey,
                                    sigmaMap=model_map,
                                    sigmaPrimary=sP,
                                    solver=Solver)

simulation.model = model

simulation.survey.dtrue = simulation.dpred(model)

# Create observations
# ------------------------------------------------------------------------
simulation.survey.dobs = survey.dtrue

# dpred = simulation.survey.dtrue.compute()

local_misfits = [data_misfit.L2DataMisfit(data=data_obj,
                                  simulation=simulation)]

local_misfits[0].W = 1. / survey.std

global_misfit = objective_function.ComboObjectiveFunction(
            local_misfits)

# Map for a regularization
regmap = maps.IdentityMap(nP=int(active_cells.sum()))
reg = regularization.Sparse(mesh, indActive=active_cells, mapping=regmap)

print('\n[INFO] Getting things started on inversion...')

# set alpha length scales.
alphaS = round(np.average(cell_array))
reg.alpha_s = 1/(alphaS*2)
reg.alpha_x = 1
reg.alpha_y = 1
reg.alpha_z = 1
reg.mref = background_conductivity * np.ones(active_cells.sum())

# Here we can set the upper and lower conductivity bounds. It is also where
# the number of iterations given by the user is input.
opt = optimization.ProjectedGNCG(maxIter=root.it,
                            upper=np.log10(1e5),
                            lower=np.log10(1e-11),
                            tolCG=1e-2, maxIterLS=50, maxIterCG=5)

coolingFactor = 2
coolingRate = 1
beta0_ratio = root.bv

directives.BetaSchedule(coolingFactor=coolingFactor,
                    coolingRate=coolingRate)

invProb = inverse_problem.BaseInvProblem(global_misfit, reg, opt)
```

```
updateSensW = directives.UpdateSensitivityWeights(threshold=root.sv)

betaest = directives.BetaEstimate_ByEig(beta0_ratio=beta0_ratio,
                                method="old")

update_IRLS = directives.Update_IRLS(f_min_change=1e-4,
                                max_irls_iterations=2,
                                coolEpsFact=1.5, beta_tol=4.,
                                coolingRate=coolingRate,
                                coolingFactor=coolingFactor)

save_model = directives.SaveUBCModelEveryIteration(mesh=mesh,
                                        mapping=model_map,
                                        file_name=f_n,
                                        replace=False)

target_misfit = directives.TargetMisfit(chifact=root.cv)

update_Jacobi = directives.UpdatePreconditioner()

directiveList = [updateSensW,
                 betaest,
                 update_IRLS,
                 save_model,
                 target_misfit,
                 update_Jacobi]

inv = inversion.BaseInversion(invProb,
                          directiveList=directiveList)

opt.LSshorten = 0.5

opt.remember('xc')

# Run Inversion
# ----------------------------------------------------------------------------

tc = time()
minv = inv.run(m_bg)
finaltime = (round(((time() - tc)/60)))
print("Total inversion runtime (minutes): ", finaltime)

# Cleaning up & creating dpred for plotting observed vs predicted
# ----------------------------------------------------------------------------
if root.mv == 1:
   remove(f_n + ".msh")

dpred = invProb.dpred
dpred = np.array(dpred)
dpred = dpred[0]
# np.savetxt("{}_predicted.mod".format(f_n), dpred, delimiter=",")

'''
# Make a mod file log
# ----------------------------------------------------------------------------
```

```
    # In Geoscience Analyst, it's easier to deal with the data in log format.
    # This can be commented out if you don't want to use the functionality.
    title = 'Please select mod file to convert to log'
    fn = filedialog.askopenfilenames(initialdir=cd, title=title,
                                     filetypes=[('Mod', '.mod')])
    fname = fn[0]

    file = open(fname, 'r')
    filedata = file.readlines()
    darray = []
    for val in filedata:
        strip = val.strip('\n')
        darray.append(strip)
    file = open('{}_log.mod'.format(f_n), 'w+')
    for val in darray:
        val = float(val)
        file.write(str(np.log10(val)))
        file.write('\n')
        '''
    root.destroy()


# plot()
# ----------------------------------------------------------------------------
# Here, it creates a plot of observed, predicted, and misfit. This gives you an
# idea of how well the inversion went and where the observed data is over- or
# under-represented in the final model.
def plot():
    global data
    print('\nMaking Figures...\n')
    plt.ioff()
    num_stn = (receiver_locations.shape[0])
    num_sets = int(ELFimport.shape[0] / len(frequencies))
    mft = np.subtract(np.abs(ELFimport), np.abs(dpred))
    # n_mft = np.divide(mft, std)

    c = 0
    data = []
    while c <= (len(ELFimport)-num_stn):
        data.append(ELFimport[c:c+num_stn])
        data.append(dpred[c:c+num_stn])
        data.append(mft[c:c+num_stn])
        # data.append(n_mft[c:c+num_stn])
        c += num_stn
    data = np.reshape(data, (len(frequencies), num_sets*3))

    if path.exists(cd + f'\\{f_n}_Obs_Pred\\'):
        pass
    else:
        mkdir(cd + f'\\{f_n}_Obs_Pred\\')

    lim_c = 0
    cnt = 0
    mft_lst = [2, 5, 8, 11]  # [2, 3, 6, 7, 10, 11, 14, 15]
    for freq in frequencies:
        c1 = 0
```

```
        cnt_comp = 0
        comps = ['rE_obs', 'rE_pred', 'rE_misfit',  # 'rE_norm_misfit',
                 'iE_obs', 'iE_pred', 'iE_misfit',  # 'iE_norm_misfit',
                 'rN_obs', 'rN_pred', 'rN_misfit',  # 'rN_norm_misfit',
                 'iN_obs', 'iN_pred', 'iN_misfit',  # 'iN_norm_misfit'
                 ]
        fig1 = plt.figure(figsize=(15, 10), dpi=115)
        for plt_comp in range(len(comps)):
            if cnt_comp in mft_lst:
                plt.set_cmap('bwr')
                ax = plt.subplot(4, 3, cnt_comp + 1)
                im = plot2Ddata(receiver_locations,
                                data[cnt,
                                    num_stn*plt_comp:num_stn*(plt_comp + 1)],
                                dataloc=True,
                                ax=ax)
            else:
                plt.set_cmap('turbo')
                ax = plt.subplot(4, 3, cnt_comp + 1)
                im = plot2Ddata(receiver_locations,
                                data[cnt,
                                    num_stn*plt_comp:num_stn*(plt_comp + 1)],
                                dataloc=True,
                                ax=ax, clim=[Emin[lim_c], Emax[lim_c]])
                if c1 == 1:
                    lim_c += 1
                    c1 = 0
                else:
                    c1 += 1
            ax.get_xaxis().set_visible(False)
            ax.get_yaxis().set_visible(False)
            divider = make_axes_locatable(ax)
            cax = divider.append_axes("right", size="5%", pad=0.05)
            plt.colorbar(im[0], cax=cax)
            cnt_comp += 1
            ax.set_title(comps[plt_comp])
        cnt += 1
        plt.subplots_adjust(wspace=0.3)
        fig1.suptitle(f'{freq}Hz Observed vs Predicted Data', fontsize='20')
        plt.savefig(cd + f'\\{f_n}_Obs_Pred\\{freq}Hz_Data.png',
                    bbox_inches='tight')
        plt.close()
    print('Done!')


# Runs the three main functions and delete global variables once complete.
if __name__ == '__main__':
    build()
    run()
    plot()
    for var in dir():
        if var[0:2] != "__":
            del globals()[var]
    del var
```